

Rudorffites and Beyond: Perovskite-Inspired Silver/Copper Pnictohalides for Next-Generation Environmentally Friendly Photovoltaics and Optoelectronics

Abhisek Chakraborty, Narendra Pai, Jing Zhao, Blair R. Tuttle, Alexandr N. Simonov,* and Vincenzo Pecunia*

In the wake of lead-halide perovskite research, bismuth- and antimony-based perovskite-inspired semiconducting materials are attracting increasing attention as safer and potentially more robust alternatives to lead-based archetypes. Of particular interest are the group IB–group VA halide compositions with a generic formula $A_xB_yX_{x+3y}$ ($A^+ = \text{Cu}^+/\text{Ag}^+$; $B^{3+} = \text{Bi}^{3+}/\text{Sb}^{3+}$; $X^- = \text{I}^-/\text{Br}^-$), i.e., silver/copper pnictohalides and derivatives thereof. This family of materials forms 3D structures with much higher solar cell efficiencies and greater potential for indoor photovoltaics than the lower-dimensional bismuth/antimony-based perovskite-inspired semiconductors. Furthermore, silver/copper pnictohalides are being investigated for applications beyond photovoltaics, e.g., for photodetection, ionization radiation detection, memristors, and chemical sensors. Such versatility parallels the wide range of possible compositions and synthetic routes, which enable various structural, morphological, and optoelectronic properties. This manuscript surveys the growing research on silver/copper pnictohalides, highlighting their composition–structure–property relationships and the status and prospects of the photovoltaic and optoelectronic devices based thereon. The authors hope that the insights provided herein might accelerate the development of eco-friendly and stable perovskite-inspired materials for next-generation photovoltaics and optoelectronics.

rising energy demand sustainably and supporting our economic and societal development. While conventional semiconductors such as silicon and III–V compounds (e.g., GaAs, InP, InAs) currently dominate the market, the processing of these materials into photovoltaics and optoelectronics is complex and energy-intensive, with limited prospects for further improvements, and requires significant capital investments despite many decades of research and development.^[1] Additionally, photovoltaic modules and optoelectronic devices based on traditional semiconductor materials typically require rigid substrates. These challenges have prompted the scientific community to search for new families of semiconductors that could allow more straightforward and economical processing with lower energy consumption, as well as flexible form factors.^[2–4]

One of the most promising families of compounds competing with conventional semiconductor technologies is that of lead halide perovskites, whose advantageous optoelectronic properties and relatively simple processing methods have been summarized in numerous publications (e.g., see recent reviews^[5–7] and references therein). As also ubiquitously reported, despite the undeniable advantages

1. Introduction

Semiconductors are the core materials of photovoltaic and optoelectronic technologies, which are central to tackling the global

A. Chakraborty, J. Zhao
Jiangsu Key Laboratory for Carbon-Based Functional Materials & Devices
Institute of Functional Nano & Soft Materials (FUNSOM)
Joint International Research Laboratory of Carbon-Based Functional
Materials and Devices
Soochow University
Suzhou 215123, China

 The ORCID identification number(s) for the author(s) of this article can be found under <https://doi.org/10.1002/adfm.202203300>.

© 2022 The Authors. Advanced Functional Materials published by Wiley-VCH GmbH. This is an open access article under the terms of the Creative Commons Attribution-NonCommercial-NoDerivs License, which permits use and distribution in any medium, provided the original work is properly cited, the use is non-commercial and no modifications or adaptations are made.

DOI: 10.1002/adfm.202203300

N. Pai
Department of Chemical Engineering
and The Australian Centre for Advanced Photovoltaics (ACAP)
Monash University
Victoria 3800, Australia

B. R. Tuttle
Department of Physics
Penn State Behrend
Erie, Pennsylvania 16563, USA

A. N. Simonov
School of Chemistry
Monash University
Victoria 3800, Australia
E-mail: alexandr.simonov@monash.edu

V. Pecunia
School of Sustainable Energy Engineering
Simon Fraser University
Surrey, BC V3T 0N1, Canada
E-mail: pecunia@sfu.ca

of lead-halide perovskites, the prospects for commercialization of technologies based on such materials are limited by their operational instability (e.g., against moisture, molecular oxygen, UV light, and elevated temperatures) and the prohibitive toxicity of lead.^[8–12] While respectable improvements in robustness are currently being achieved (yet still not at the level required for broad implementation),^[13–16] the use of toxic lead is most likely impossible to avoid in high-performance organo-metal halide perovskites, at least for photovoltaic applications.^[17,18] The toxicity aspect can hardly be ignored in light of the increasingly strict regulations worldwide.^[19,20] Hence, the development of lead-free perovskites or chemically analogous compounds has emerged as essentially a separate research sub-field primarily over the past five years.^[21–23]

Arguably, the most intense investigations in this direction are on the homovalent substitution of lead with tin, which, however, has a range of limitations discussed in numerous reviews.^[24,25] More broadly, the search for lead-free perovskite-inspired alternatives has focused on elements with electronic configurations similar to that of lead, since the defect tolerance of lead-halide perovskites has been linked to the high symmetry of the corner-sharing [PbX₆] octahedra and the ionic-covalent bonding arising from the stable ns² configuration of the Pb²⁺ cations that hybridize with halide anions.^[26–29] Group VA elements bismuth and antimony in their 3+ oxidation states formally fit this criterion and are also known to be highly stable.^[30] However, due to their different oxidation state than Pb²⁺, bismuth and antimony halide compounds do not adopt the conventional perovskite crystal structure. They are therefore referred to as perovskite-inspired semiconducting materials.

Two families of Sb- and Bi-based absorbers that have received considerable research attention include defect-ordered perovskites with the formula A₃B₂X₉ (e.g., Cs₃Sb₂I₉) and cation-ordered double perovskites with the formula A₂B'BX₆ (e.g., Cs₂AgBiBr₆). Herein, “B” refers to Bi or Sb consistent with the nomenclature accepted in the field of halide perovskites and derivatives; hence, it should not be confused with boron. Such materials, however, have wide bandgaps (typically of ≈2 eV or greater), large exciton binding energies (>100 meV) and low dimensionality (of 2 or lower, either structurally or electronically), all of which are detrimental to effective charge transport and optoelectronic device performance.^[30–33] Some of these limitations, however, can be partially resolved by replacing the conventional A-site cations derived from the lead-halide perovskites field, viz. Cs⁺, Rb⁺, MA⁺ (methylammonium), and FA⁺ (formamidinium) because their chemical nature and ionic radii define the dimensionality of bismuth/antimony-based perovskite-inspired semiconducting materials.^[34–36] Indeed, the introduction of coinage transition metal cations Ag⁺ or Cu⁺ produces three-dimensional networks of Bi/Sb-based halides, where the A-site cations also contribute to bonding through the formation of [AX₆] octahedra.^[30,34,37] Such compounds have a basic chemical formula A_xB_yX_{x+3y} (where A⁺ is Ag⁺ or Cu⁺, B³⁺ is Bi³⁺ or Sb³⁺ or a combination thereof, and X⁻ is I⁻ or Br⁻) and feature lattices with higher dimensionality compared to other antimony- and bismuth-based perovskite-inspired materials, suggesting their superior optoelectronic and photovoltaic properties.^[30] The structure of some silver/copper pnictohalides has been termed “rudorffite” in the literature, but other structures

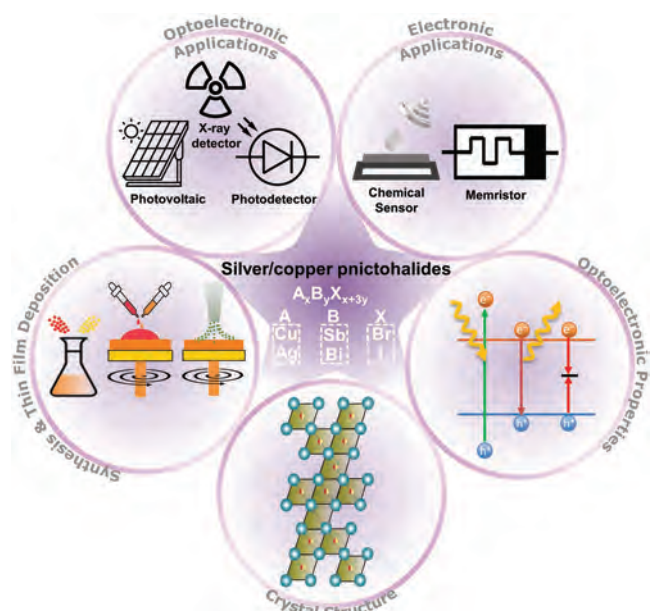


Figure 1. Schematic representation of various topics on halopnictogenates covered in this review. Photovoltaic icon was created by Pixel perfect from www.flaticon.com.

are also possible. Additional benefits of many such compounds are their comparatively high charge carrier mobility, narrower bandgaps, higher operational stability, and compatibility with low-temperature processing.

Silver(I)- and copper(I)-based pnictohalides exhibit absorption coefficients over 10⁵ cm⁻¹ with direct optical bandgaps in the range of 1.6–2.8 eV,^[38–40] making them potentially suitable for a range of optoelectronic applications. Furthermore, the reported single-junction solar photovoltaic efficiency of silver pnictohalides has more than quadrupled within just three years from the first solar cell study, increasing from 1.09 ± 0.12%^[41,42] to 5.44 ± 0.07%.^[36] Building upon the optoelectronic versatility of Bi and Sb-based perovskite-inspired materials and motivated by their promising photovoltaic performance, the scientific community has set out to investigate the capabilities of silver/copper nanocomposites for other applications, such as photodetectors, X-ray detectors, memristors, and chemical sensors.

The present manuscript aims to provide the first comprehensive overview of the properties and device applications of silver/copper pnictohalides, as schematically shown in **Figure 1**. We first survey the reported material compositions and current understanding of their structural characteristics. Further, we discuss the synthetic, processing, and cationic/anionic modification strategies adopted for the fabrication of various silver/copper nanocomposites and their impact on the morphology and optoelectronic properties of the resulting materials. We then analyze the performance of the compounds of interest in various optoelectronic applications, including photovoltaics, photodetectors, chemical sensors, and memristors. By providing a comprehensive and up-to-date assessment of the properties and device performance of silver/copper pnictohalides, this review aims to analyze the status of this promising class of materials and catalyze further progress in their development for easy-to-make and eco-friendly photovoltaics and optoelectronics.

2. Crystal Structures and Compositions

Much like lead-halide perovskites, which take their name from the parent, isostructural compound calcium titanate (CaTiO_3), in turn named perovskite in honor of mineralogist Lev von Perovski, Turkevych et al. suggested the term *rudorffite*^[43] in 2017 to refer to ternary metal-halide compounds with a structure closely related to NaVO_2 , a synthetic material first characterized by Walter Rüdorff.^[44] However, the structure of NaVO_2 was already officially named *caswellsilverite* by Okada and Keil in 1982^[45] as sanctioned by the Commission on New Minerals and Mineral Names of the International Mineralogical Association, in honor of geologist Dr. Caswell Silver, and in association with the naturally occurring mineral NaCrS_2 , which was found in meteorite fragments in Norton County (KS), USA.^[45]

Both model compounds NaVO_2 and NaCrS_2 belong to the $R\bar{3}m$ space group having a CdCl_2 -type rhombohedral structure (Figure 2a), featuring layers of edge-sharing $[\text{NaO}_6]$ octahedra alternating with layers of edge-sharing $[\text{VO}_6]/[\text{CrS}_6]$ octahedra (Figure 2b). A similar crystal structure (with space group $R\bar{3}m$) was found by Turkevych et al.^[43] in ternary metal-halide compounds with the formula $\text{Ag}_x\text{Bi}_y\text{I}_{x+3y}$ (Figure 2c). Indeed, akin to the model compounds NaVO_2 and NaCrS_2 , the “rudorffites” reported by Turkevych et al. are composed of edge-sharing octahedra, specifically $[\text{AX}_6]$ or $[\text{BX}_6]$.^[43] However, in contrast to NaVO_2 and NaCrS_2 , where the cation sublattice is filled, the layers found in silver-bismuth iodides also comprise vacancies. Such vacancies are inherently determined by the charge neutrality rule, given the different oxidation states of the metal cations (Ag^+ and Bi^{3+}) at the center of the metal-halide octahedra. In other words, the alternating layers of edge-sharing octahedra found in $\text{Ag}_x\text{Bi}_y\text{I}_{x+3y}$ materials feature different proportions of $[\text{AgI}_6]$, $[\text{BiI}_6]$, and $[\Delta\text{I}_6]$ octahedra, where Δ indicates a vacancy.

Moreover, a different structure has been reported for some embodiments of the same family of metal-halide compounds with the formula $\text{A}_x\text{B}_y\text{X}_{x+3y}$ ($\text{A}^+ = \text{Ag}^+/\text{Cu}^+$, $\text{B}^{3+} = \text{Bi}^{3+}/\text{Sb}^{3+}$, and $\text{X}^- = \text{I}^-/\text{Br}^-$) and derivatives. For example, such compounds can also adopt a cubic spinel structure with space group

$Fd\bar{3}m$ (Figure 2d), as opposed to the rhombohedral structure observed by Turkevych et al.^[43] similar to the mineral spinel MgAl_2O_4 .^[46,43,47] A typical MgAl_2O_4 structure consists of a face-centered cubic oxygen anion sublattice with tetrahedral sites occupied by divalent cations (Mg^{2+}) and octahedral sites occupied by trivalent cations (Al^{3+}).^[46] This structuring is also observed in silver bismuth iodides with space group $Fd\bar{3}m$, where the iodide anion sublattice is face-centered cubic close-packed.^[43] Since the tetrahedral sites in silver bismuth iodides with space group $Fd\bar{3}m$ are completely vacant and both metal cations occupy the octahedral sites, silver bismuth iodides with space group $Fd\bar{3}m$ are often referred to as having a defect spinel structure.^[43] While correlating them to pnictogen-based lower-dimensional perovskite-inspired materials (where the coordination numbers of 12 for the alkali metals and 8 for the pnictogens result in corner-sharing but low-dimensional octahedral networks), silver(I) and copper(I) pnictohalides contain orderly edge-sharing alternating octahedra of $[\text{AX}_6]$ and $[\text{BX}_6]$ with a coordination number of 6. While such a structure differs from that of NaVO_2 *caswellsilverite* (or “rudorffite”), the recent literature on $\text{A}_x\text{B}_y\text{X}_{x+3y}$ metal-halides has also applied the term “rudorffite” to embodiments presenting the aforementioned cubic defect spinel structure.^[43] Given the structural diversity of the $\text{A}_x\text{B}_y\text{X}_{x+3y}$ family of perovskite-inspired materials, we refer to such compounds as “silver/copper pnictohalides”. Indeed, this term is not exclusively applicable to one particular structural subset of this family of perovskite-inspired materials and, at the same time, is consistent with the variety of compositions possible.

Having outlined the general features of silver/copper pnictohalide structures, we further discuss the distinctive structural and compositional properties of the various silver(I) and copper(I) pnictohalides developed to date (see Table 1 for a comprehensive list of the compositions, structures, and processing methods reported thus far). First, we focus on $\text{Ag}_x\text{Bi}_y\text{X}_{x+3y}$ ($\text{B} = \text{Bi}^{3+}$ or Sb^{3+} ; $\text{X} = \text{I}^-$ or Br^-) compounds as the most intensively investigated materials in this class. Note that, to date, no reports have been published on silver(I) pnictohalides based purely on X-anions other than iodine and bromine.

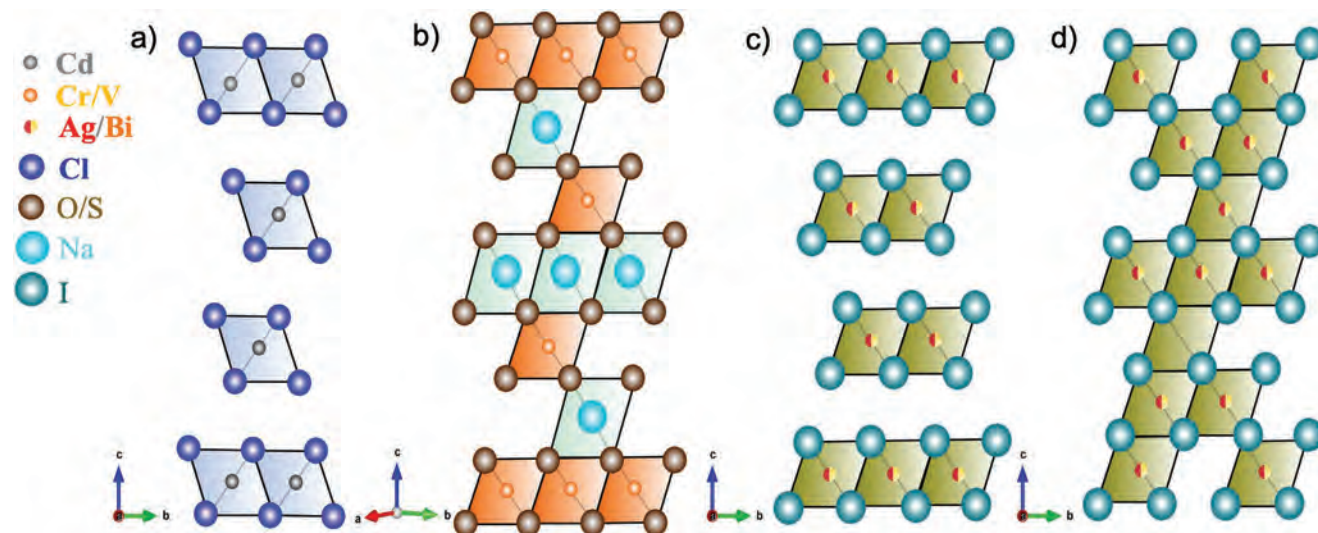


Figure 2. Crystal structure of a) CdCl_2 ; b) $\text{NaVO}_2/\text{NaCrS}_2$; c) CdCl_2 -type $\text{A}_x\text{B}_y\text{X}_{x+3y}$ materials, and d) defect spinel-type $\text{A}_x\text{B}_y\text{X}_{x+3y}$ materials.

Table 1. Silver/copper pnictohalides: compositions, structures, and processing methods reported to date.

First Author/Year	Material	Space group	Method	Solvents	Antisolvents
Fourcroy/1979 ^[55]	AgBi ₂ 7 (crystal)	$Fd\bar{3}m$	Melt-crystallization		
Fourcroy/1979 ^[55]	Ag ₂ Bi ₅ (crystal)	$R\bar{3}m$	Melt-crystallization		
Dzeranova/1985 ^[56]	AgBi ₄ (crystal)		Melt-crystallization		
Oldag/2005 ^[48]	Ag ₃ Bi ₆ (crystal)	$R\bar{3}m$	Solvothermal reaction		
Oldag/2005 ^[48]	AgBi ₄ (crystal)	$Fd\bar{3}m$	Solvothermal reaction		
Mashadieva/2013 ^[49]	AgBi ₂ 7	$Fd\bar{3}m$	Solvothermal reaction		
Mashadieva/2013 ^[49]	Ag ₂ Bi ₅	$R\bar{3}m$	Solvothermal reaction		
Kim/2016 ^[41]	AgBi ₂ 7	$Fd\bar{3}m$	One step spin-coating	n-butylamine	
Zhu/2017 ^[50]	Ag ₂ Bi ₅	$R\bar{3}m$	One step spin-coating	n-butylamine	
Zhu/2017 ^[50]	AgBi ₂ 7	$Fd\bar{3}m$	One step spin-coating	n-butylamine	
Jung/2017 ^[53]	Ag ₂ Bi ₅	$R\bar{3}m$	Antisolvent-assisted spin-coating	DMSO/DMF/HI	Diethyl ether
Sansom/2017 ^[54]	AgBi ₄ (crystal)	$Fd\bar{3}m$	Chemical vapor transport		
Sansom/2017 ^[54]	AgBi ₄ (powder)	$Fd\bar{3}m$ and $R\bar{3}m$	Melting crystallization		
Sansom/2017 ^[54]	AgBi ₄ (film)	$Fd\bar{3}m$ and $R\bar{3}m$	Drop-casting	DMSO	
Turkevych/2017 ^[43]	Ag ₃ Bi ₆	$R\bar{3}m$	Antisolvent-assisted spin-coating	DMSO	Toluene
Turkevych/2017 ^[43]	Ag ₂ Bi ₅	$R\bar{3}m$	Antisolvent-assisted spin-coating		
Turkevych/2017 ^[43]	AgBi ₄	$Fd\bar{3}m$	Antisolvent-assisted spin-coating		
Turkevych/2017 ^[43]	AgBi ₂ 7	$Fd\bar{3}m$	Antisolvent-assisted spin-coating		
Turkevych/2017 ^[43]	Ag ₃ Bi ₆	$R\bar{3}m$	Melting crystallization		
Turkevych/2017 ^[43]	Ag ₂ Bi ₅	$R\bar{3}m$	Melting crystallization		
Turkevych/2017 ^[43]	AgBi ₄	$Fd\bar{3}m$	Melting crystallization		
Turkevych/2017 ^[43]	AgBi ₂ 7	$Fd\bar{3}m$	Melting crystallization		
Ghosh/2018 ^[88]	Ag ₂ Bi ₅	$R\bar{3}m$	Antisolvent-assisted dynamic hot casting	DMSO/DMF	Chlorobenzene
Ghosh/2018 ^[88]	AgBi ₄	$Fd\bar{3}m$	Antisolvent-assisted dynamic hot casting	DMSO/DMF	Chlorobenzene
Ghosh/2018 ^[88]	AgBi ₂ 7	$Fd\bar{3}m$	Antisolvent-assisted dynamic hot casting	DMSO/DMF	Chlorobenzene
Lu/2018 ^[89]	AgBi ₄	$Fd\bar{3}m$	Antisolvent-assisted spin-coating	DMSO/DMF	methylbenzene
Shao/2018 ^[39,51]	AgBi ₂ 7	$Fd\bar{3}m$	Conventional one-step spin-coating	DMF/HCl	
Shao/2018 ^[39,51]	AgBi ₄	$R\bar{3}m$	Conventional one-step spin-coating	DMF/HCl	
Shao/2018 ^[39,51]	Ag ₄ Bi ₅ 19	$R\bar{3}m$	Conventional one-step spin-coating	DMF/HCl	
Shao/2018 ^[39,51]	Ag ₂ Bi ₃ 11	$Fd\bar{3}m$	Conventional one-step spin-coating	DMF/HCl	
Shao/2018 ^[39,51]	Ag ₄ Bi ₇ 25	$Fd\bar{3}m$	Conventional one-step spin-coating	DMF/HCl	
Shao/2018 ^[39,51]	AgBi ₂ 7	$Fd\bar{3}m$	Conventional one-step spin-coating	DMF/HCl	
Shao/2018 ^[39,51]	Ag ₄ Bi ₉ 31	$Fd\bar{3}m$	Conventional one-step spin-coating	DMF/HCl	
Pai/2019 ^[42]	Ag ₃ Bi ₆	$R\bar{3}m$	Gas-assisted spin-coating	DMSO/DMF/HI	
Pai/2019 ^[42]	Ag ₂ Bi ₅	$R\bar{3}m$	Gas-assisted spin-coating	DMSO/DMF/HI	
Pai/2019 ^[42]	AgBi ₄	$Fd\bar{3}m$	Gas-assisted spin-coating	DMSO/DMF/HI	
Pai/2019 ^[42]	AgBi ₂ 7	$Fd\bar{3}m$	Gas-assisted spin-coating	DMSO/DMF/HI	
Kulkarni/2019 ^[57]	AgBi ₂ 7	$Fd\bar{3}m$	Antisolvent-assisted spin-coating	DMSO	Chlorobenzene
Kulkarni/2019 ^[57]	AgBi ₂ 7	$Fd\bar{3}m$	Antisolvent-assisted spin-coating	n-butylamine	Chlorobenzene
Khazaei/2019 ^[90]	AgBi ₄	$Fd\bar{3}m$	Coevaporation		

Table 1. Continued.

First Author/Year	Material	Space group	Method	Solvents	Antisolvents
Khazaee/2019 ^[90]	AgBi ₂ I ₇	$Fd\bar{3}m$	Coevaporation		
Khazaee/2019 ^[90]	Ag ₂ BiI ₅	$R\bar{3}m$	Coevaporation		
Tu/2019 ^[59]	Ag ₃ BiBr ₆	$R\bar{3}m$	Conventional one-step spin-coating	n-butylamine	
Zhang/2019 ^[79]	AgBiI ₄	$Fd\bar{3}m$	Additive-assisted spin-coating	DMSO/DMF/HI	Chlorobenzene
Koedtrud/2019 ^[52]	Ag _{0.35} Bi _{0.55} I ₂	$Fd\bar{3}m$	Solid-state reaction		
Koedtrud/2019 ^[52]	Ag _{0.65} Bi _{0.45} I ₂	$R\bar{3}m$	Solid-state reaction		
Ye/2020 ^[91]	AgBiI ₄	$Fd\bar{3}m$	Anti-solvent assisted hot-casting	DMSO/DMF	Chlorobenzene
Pecunia/2020 ^[92]	Ag ₂ BiI ₅	$R\bar{3}m$	Antisolvent-assisted spin-coating	DMSO/DMF	Chloroform
Pecunia/2020 ^[92]	Ag ₂ BiI ₅	$R\bar{3}m$	Dynamic hot casting method	DMSO/DMF	Toluene
Pecunia/2020 ^[92]	Ag ₂ BiI ₅	$Fd\bar{3}m$	Additive	DMSO/DMF/HI	
Premkumar/2020 ^[12]	AgBiI ₄ (quantum dots)	$R\bar{3}m$	Ligand-assisted precipitation		
Premkumar/2020 ^[12]	Ag ₂ BiI ₅ (quantum dots)	$Fd\bar{3}m$	Ligand-assisted precipitation		
Premkumar/2020 ^[12]	AgBi ₂ I ₇ (quantum dots)	$R\bar{3}m$	Ligand-assisted precipitation		
Seo/2020 ^[93]	Ag ₃ BiI ₆	$Fd\bar{3}m$	Conventional one-step spin-coating	n-butylamine	
Tie/2020 ^[94]	AgBi ₂ I ₇ (single crystals)	$R\bar{3}m$	Traditional Bridgman method		
Yi/2020 ^[95]	AgBi ₃ I ₁₀	$R\bar{3}m$	Conventional one-step spin-coating	n-butylamine	
Hu/2020 ^[58]	Ag ₃ Bi ₂ I ₉	$R\bar{3}m$	Anti-solvent assisted spin-coating	DMSO	Toluene
Danilović/2020 ^[96]	Ag ₃ BiI ₆ (nanoparticles)	$R\bar{3}m$	Aerosol synthesis	DMSO	
Lee/2021 ^[97]	Ag ₂ Bi ₃ I ₁₁ (nanoparticles)	$R\bar{3}m$	Conventional one-step spin-coating	DMSO/DMF/HI	
He/2021 ^[98]	Ag ₂ BiI ₅	$R\bar{3}m$	Gas-assisted spin-coating	DMSO/DMF	
Shadabroo/2021 ^[99]	Ag ₂ BiI ₅	$R\bar{3}m$	Conventional one-step spin-coating	DMSO/DMF	
Prasad/2021 ^[38]	AgBiI ₄	$Fd\bar{3}m$	Sol-gel approach		
Prasad/2021 ^[38]	Ag ₂ BiI ₅	$R\bar{3}m$			
Bera/2021 ^[100]	AgBi ₃ I ₁₀	$Fd\bar{3}m$	Anti-solvent assisted dynamic hot-casting	DMSO/DMF	Dichlorobenzene
Bera/2021 ^[100]	AgBi ₂ I ₇	$Fd\bar{3}m$	Anti-solvent assisted dynamic hot-casting	DMSO/DMF	Dichlorobenzene
Bera/2021 ^[100]	AgBiI ₄	$Fd\bar{3}m$	Anti-solvent assisted dynamic hot-casting	DMSO/DMF	Dichlorobenzene
Bera/2021 ^[100]	Ag ₂ BiI ₅	$R\bar{3}m$	Anti-solvent assisted dynamic hot-casting	DMSO/DMF	Dichlorobenzene
Bera/2021 ^[100]	Ag ₃ BiI ₆	$R\bar{3}m$	Anti-solvent assisted dynamic hot-casting	DMSO/DMF	Dichlorobenzene
Gray/2021 ^[62]	AgSbI ₄	$R\bar{3}m$	Solid-state reaction		
Zhu/2020 ^[63]	AgSb ₂ I ₇	$Fd\bar{3}m$	Conventional one-step spin-coating	DMSO/DMF	
Iyoda/2020 ^[83]	Ag ₂ BiI ₅	$R\bar{3}m$	Antisolvent-assisted spin-coating	DMSO/HI	Various solvents
Iyoda/2020 ^[83]	Ag ₂ SbI ₅	$R\bar{3}m$	Antisolvent-assisted spin-coating	DMSO/HI	Various solvents
Hu/2018 ^[66]	CuBiI ₄	$Fd\bar{3}m$	Solvent Vapour Annealing – spin coating	N,N-dimethylacetamide (DMA)	
Zhang/2019 ^[101]	CuBiI ₄	$Fd\bar{3}m$	Direct metal surface elemental reaction (DMSER)		

Table 1. Continued.

First Author/Year	Material	Space group	Method	Solvents	Antisolvents
Qu/2020 ^[102]	CuBiI ₄	$Fd\bar{3}m$	Direct metal surface elemental reaction (DMSER)		
Yu/2020 ^[103]	CuBiI ₄	$Fd\bar{3}m$	Direct metal surface elemental reaction (DMSER) : 3-step chemical vapour deposition		
Fourcroy/1991 ^[67]	CuBiI ₄	$Fd\bar{3}m$	Solid-state reaction		
Bahari/2009 ^[104]	CuBiI ₄	$Fd\bar{3}m$	Melt-crystallization		
Bahari/2009 ^[104]	Cu ₂ BiI ₅	$R\bar{3}m$	Melt-crystallization		
Baranwal/2017 ^[72]	Ag ₃ BiI ₆	$R\bar{3}m$	Conventional one-step spin-coating	DMSO	
Baranwal/2017 ^[72]	Ag ₃ Bi(SCN) ₆	$R\bar{3}m$	Conventional one-step spin-coating	DMSO	
Baranwal/2017 ^[72]	Cu ₃ BiI ₆	$R\bar{3}m$	Conventional one-step spin-coating	DMSO	
Ramachandran/2021 ^[71]	Cu ₂ BiI ₅	$R\bar{3}m$	Two-step: spin-coating + thermal evaporation	DMF (for BiI ₃)	
Sansom/2021 ^[82]	CuBiI ₄	$R\bar{3}m$	Melt-crystallization		
Jia/2019 ^[40]	Cu ₃ SbI ₆	$R\bar{3}m$	Conventional one-step spin-coating		

Furthermore, we describe the Cu_xBi_yI_{x+3y} (B = Bi³⁺ or Sb³⁺) compositions, which are currently attracting growing attention. Finally, the possibilities for partial cation/anion substitution in silver(I) and copper(I) pnictohalides are discussed.

2.1. Silver(I) Pnictohalides

The Ag–Bi–I ternary compounds were initially investigated as potential ionic (Ag⁺) conductors^[48,49] and were first suggested as promising photoabsorbers only in 2016 by Kim et al.^[41] As mentioned in the previous section, the disorder at the cationic sublattices induced by the partial occupancy of monovalent or trivalent cations results in different stoichiometric variations in the same family of compounds.

Generally, silver iodobismuthates Ag_xBi_yI_{x+3y} have a cubic close-packed iodide sublattice, while the edge-sharing cation sublattice can form either a rhombohedral CdCl₂-type layered or a three-dimensional cubic defect spinel structure. The CdCl₂-type rhombohedral structure with $R\bar{3}m$ symmetry is typically found in silver-rich compositions with $x > 1$, which feature a lattice with disordered Ag⁺ and Bi³⁺ cations occupying every other <111> layer of the octahedral space.^[43,50,51] In this case, the metal cations occupy the 3a edge-sharing octahedral sites, while a small amount of Ag⁺ occupies the 3b sites (Figure 3a).^[52] Consequently, the reduction in the overall octahedral site occupancies due to each Bi³⁺ cation being charge-balanced with three Ag⁺-cations implies that these spinel structures can still possess vacancies. In contrast, bismuth-rich compositions with $\gamma > 1$ have been typically reported to contain more vacant sites in the edge-shared cation octahedral sublattice and to adopt a cubic defect spinel structure with $Fd\bar{3}m$ symmetry. Thus, the Ag⁺ and Bi³⁺ cations are statistically disordered, and the tetrahedral sites are vacant.^[50,52,53] Due to the presence of vacant sites, the structure of such silver iodobismuthates is referred to as the defect

spinel structure. In this case, both Ag⁺ and Bi³⁺ cations occupy the 16c edge-sharing octahedral site to form a 3D network (Figure 3b). The vacant tetrahedral sites in the cubic defect spinel structure have been attributed to the large ionic radii of Ag⁺ and Bi³⁺ ions, which prevent them from occupying such sites.^[52] However, the octahedral sites in the rhombohedral structure of the silver-rich compositions are large enough to accommodate the metal cations.^[52]

Given that the structure of Ag_xBi_yI_{x+3y} is determined by the relative amounts of bismuth and silver, the AgBiI₄ compound with equimolar amounts of the two metal cations presents a peculiar case. It has been found that this material can adopt either a rhombohedral or a cubic defect spinel structure but not a mixture of the two. This implies the potential of twinning the occupied half of the octahedral sites, which can share the edges and produce vacancy-separated two-dimensional layers. Additionally, it has been suggested that the rhombohedral phase of this particular composition shows equal occupancy of the 3a octahedral site by Ag⁺ and Bi³⁺ cations and no vacancies.^[43] In fact, Rietveld analysis of the synchrotron X-ray diffraction (XRD) data undertaken by Koedtruaad et al. for silver-rich Ag_xBi_yI_{x+3y} with a rhombohedral structure suggests complete occupancy of the 3a edge-sharing octahedral site by the cations with occupancies of Ag:Bi = 0.554:0.446.^[52] While the two suggested structures (rhombohedral and cubic) are very similar, the cell of the defect-spinel cubic structure in its trigonal setting has four times the volume of the CdCl₂-type rhombohedral unit cell. Furthermore, the two can be readily distinguished from the X-ray diffraction peaks at $2\theta \approx 42^\circ$: while the defect-spinel cubic structure gives rise to one peak corresponding to the (440) plane, the CdCl₂-type rhombohedral structure produces two peaks corresponding to the (110) and (108) planes (Figure 3e).^[54]

As discussed above, the disorder induced at the cationic sublattices by partial occupancy of the monovalent or trivalent

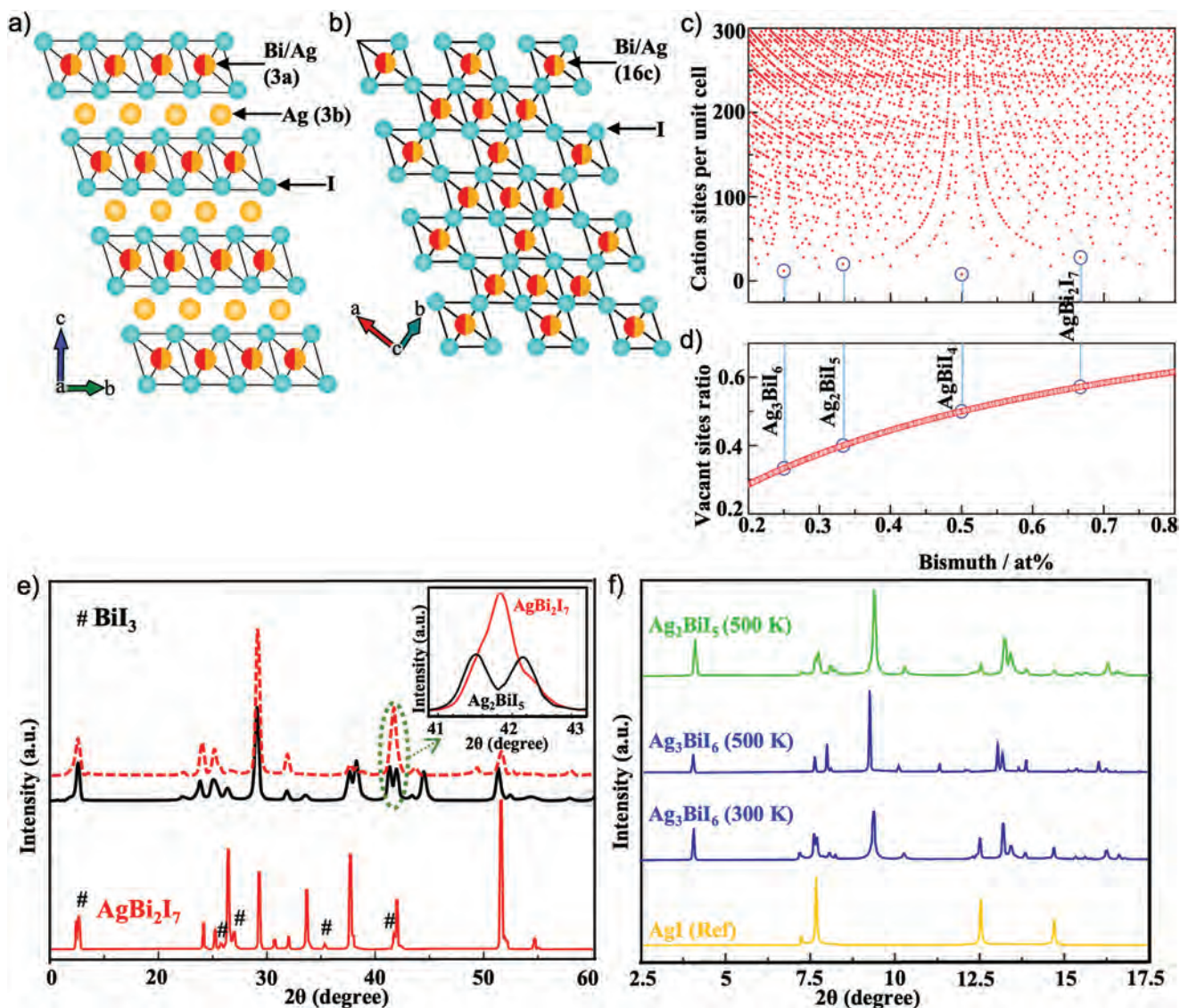


Figure 3. Crystal structures of $\text{Ag}_x\text{Bi}_{1-x/3}\text{I}_y$: a) CdCl_2 -type rhombohedral phase and b) cubic defect-spinel phase (yellow – Ag^+ , red – Bi^{3+} , teal – I^-). c) Silver iodobismuthates with cation sites per unit cell that satisfy the stoichiometry and charge neutrality rule. Reproduced with permission.^[43] Copyright 2017, John Wiley and Sons. d) Variation in vacancy site ratio for silver iodobismuthates with different stoichiometry. Reproduced with permission.^[43] Copyright 2017, John Wiley and Sons. e) XRD patterns of Ag_2BiI_5 . Reproduced under the terms of the Creative Commons Attribution CC-BY 4.0 International License.^[50] Copyright 2017, John Wiley and Sons, AgBi_2I_7 . Reproduced with permission.^[39] Copyright 2017, Elsevier. f) Ag_2BiI_5 and Ag_3BiI_6 . Reproduced with permission.^[43] Copyright 2017, John Wiley and Sons. The inset in panel (e) highlights the single peak of AgBi_2I_7 and a double peak of Ag_2BiI_5 at $2\theta = 42^\circ$. Reproduced under the terms of the Creative Commons Attribution CC-BY 4.0 International License.^[50] Copyright 2017, John Wiley and Sons. The presence of e) BiI_3 impurity in AgBi_2I_7 and f) AgI impurity in silver-rich Ag_3BiI_6 and Ag_2BiI_5 is identified. Reproduced with permission.^[43] Copyright 2017, John Wiley and Sons.

cations results in different stoichiometric variations in the Ag–Bi–I system. By varying the atomic ratio of Ag and Bi, several silver iodobismuthates have been synthesized, leading to a debate about the compositions and structures of these compounds. Fourcroy et al. identified two Ag–Bi–I phases of silver-rich Ag_2BiI_5 (hexagonal) and bismuth-rich AgBi_2I_7 (cubic), which exhibit congruent melting and peritectic reaction decomposition, respectively.^[55] Dzeranova et al. observed two different compositions, AgBiI_4 and Ag_3BiI_6 , which exist in the same system that melts congruently.^[56] Oldag et al.^[48] discovered that silver-rich Ag_3BiI_6 and substoichiometric silver-deficient AgBiI_4

crystallize in $R\bar{3}m$ and $Fd\bar{3}m$ symmetry, respectively, with significant cationic substructural disordering. A subsequent thermodynamic study by Mashadiev et al. of the AgI– BiI_3 phase diagram could not confirm the existence of Ag_3BiI_6 and AgBiI_4 as individual phases but instead identified two intermediate phases $\gamma\text{-Ag}_2\text{BiI}_5$ at 33.3 mol.% BiI_3 and $\delta\text{-AgBi}_2\text{I}_7$ at 60.0–66.7 mol.% BiI_3 , similar to those reported by Fourcroy et al.^[49]

Later, Kim et al. proposed that AgBi_2I_7 crystallizes in the $Fd\bar{3}m$ space group with the $[\text{AgI}_6]$ and $[\text{BiI}_8]$ polyhedra, producing a structure analogous to that of ThZr_2H_7 .^[41] However, this claim was challenged by Xiao et al. in their structural and

computational investigation demonstrating an impractically short Bi-I bond length and high mass density.^[47] This group suggested that the silver-deficient AgBiI_4 cubic structure with $[\text{AgI}_6]$ and $[\text{BiI}_6]$ octahedra is more likely for AgBi_2I_7 .^[47] However, Sansom et al. revealed twinning of the cubic defect spinel and rhombohedral structure in the octahedral faceted AgBiI_4 polycrystalline films and powder samples.^[54] At the same time, the single crystal growth of AgBiI_4 resulted in plate-like rhombohedral crystals.^[54] Finally, Turkevych et al. suggested that compositions Ag_3BiI_6 , Ag_2BiI_5 , AgBiI_4 , and AgBi_2I_7 fulfill the stoichiometry and charge neutrality requirements due to their smallest unit cells and thus are thermodynamically preferable to form (Figure 3c).^[43] They have also reported that the vacant site ratio increases with increasing bismuth content (Figure 3d).

Additionally, $\text{Ag}_x\text{Bi}_y\text{I}_{x+3y}$ materials have often been reported to contain impurities depending on the composition. An AgI impurity phase has been found in silver-rich Ag_2BiI_5 and Ag_3BiI_6 , while excess BiI_3 has been reported for bismuth-rich iodobismuthates such as AgBi_2I_7 (Figure 3e,f).^[43,53,57] However, AgI was found to be unstable at high temperatures (> 500 K), which thereby enables the formation of the pure $R\bar{3}m$ rhombohedral pnictohalide phase (Figure 3f). In bismuth-rich $\text{Ag}_x\text{Bi}_y\text{I}_{x+3y}$ with $\gamma > 1$, BiI_3 was also found in several independent studies, although no universal strategy for its elimination has been proposed (Figure 3e).^[39,53]

Finally, other Bi-rich compositions such as $\text{AgBi}_3\text{I}_{10}$, $\text{Ag}_2\text{Bi}_3\text{I}_{11}$, $\text{Ag}_4\text{Bi}_5\text{I}_{19}$, $\text{Ag}_4\text{Bi}_7\text{I}_{25}$, and $\text{Ag}_4\text{Bi}_9\text{I}_{31}$ and Ag-rich compositions such as $\text{Ag}_{0.65}\text{Bi}_{0.45}\text{I}_2$ and $\text{Ag}_3\text{Bi}_2\text{I}_9$ have been reported.^[51,52,58] Consistent with earlier studies, the Ag-rich compositions resulted in CdCl_2 -type rhombohedral phases with AgI impurities, and the Bi-rich compositions formed cubic phases with BiI_3 impurities.

The only report on silver bismuth bromide, Ag_3BiBr_6 , also re-established the formation of the hexagonal crystal structure with the $R\bar{3}m$ space group symmetry,^[59] similar to the iodide Ag-rich compositions.

Even though the electronic configuration and coordination properties of antimony are close to those of bismuth in many respects,^[60,61] silver-antimony halide compositions are not well explored at present, and there are only a few reports available in the literature. Recent studies by Gray et al.^[62] and Zhu et al.^[63] on AgSbI_4 and AgSb_2I_7 , respectively, revealed structural features for these materials similar to those of bismuth-based analogs. AgSb_2I_7 fits the Ag-deficient $Fd\bar{3}m$ cubic crystal structure, single crystals of AgSbI_4 are inclined to form the CdCl_2 -type rhombohedral structure, and both are coordinated in the $[\text{Ag/SbI}_6]$ octahedra with disordered tetrahedral vacant sites. It is also interesting that annealing AgSb_2I_7 films at 125°C induces significant changes in the XRD pattern, including the disappearance of peaks at 12° and 28° along with the emergence of AgI peaks, which implies significant distortion to the crystal structure.

Thus, an expansive library of $\text{Ag}_x\text{Bi}_y\text{X}_{x+3y}$ materials has been discovered over a comparatively short period. The structure of many of these materials is now reasonably well understood. The structural features summarized above again emphasize that referring even to silver(I) pnictohalides as rudorffites or caswellsilverites is not entirely appropriate. These materials adopt different crystal structures depending on the Ag:pnictogen

ratio, which expectedly influences their optoelectronic properties, as discussed in Section 4.

2.2. Copper(I) Pnictohalides

Apart from silver(I)-based materials, another class of group IB-group VA halides that have received reasonable investigative attention are copper(I) pnictohalides, of which $\text{Cu}_x\text{Bi}_y\text{I}_{x+3y}$ materials are currently the most frequently studied. These compounds are compositional analogs of the silver iodobismuthates presented in Section 2.1. Apart from the obvious fundamental interest, the lower price of copper compared to silver is one primary reason that motivates the investigation of copper pnictohalides.^[64,65]

Similar to the Ag-Bi-I systems, Fourcroy et al. were the first to study the structure of the CuBiI_4 compound, which adopts a cubic defect-spinel structure^[66] (space group $Fd\bar{3}m$) and is a structural analog of AgBiI_4 with the same structural symmetry (Figure 4a).^[67] In CuBiI_4 , each iodine atom is surrounded by three atoms of bismuth and eight atoms of copper (one Cu (1), six Cu (2), and one Cu (3)). Bismuth atoms are found in position 16c and have an occupancy rate of $1/2$ and other $1/2$ vacancies leading to an overall octahedral occupancy of 25%. Each bismuth atom is in the center of an almost perfect octahedron surrounded by six neighboring iodine atoms. Copper atoms occupy positions 8a and 48f with occupancy rates of 0.18 and 0.12, respectively, and to a lesser extent, position 8b with an occupancy rate of 0.09. Copper atoms are found in the center of four cubes of the eight vertices occupied by iodine atoms in such a way that they form a tetrahedral unit. The ratio of the number of unoccupied to occupied sites was reported to be 1.58.^[67]

Hu and co-workers^[66] also provided detailed structural information (Figure 4b) on Cu-Bi-I systems consistent with the findings of Fourcroy et al.^[67] They demonstrated a cubic crystal structure with the $Fd\bar{3}m$ space group for CuBiI_4 . However, Sansom et al. have recently raised concern over the stability of the CuBiI_4 phase under ambient conditions while exploring the phase diagram of the quaternary copper-silver-bismuth-iodine system (focusing on $\text{Cu}_2\text{AgBiI}_6$). According to this study, CuBiI_4 presents a metastable phase that decomposes to CuI and BiI_3 at room temperature.^[68] In a follow-up study, the same team also found the possibility of twinning in CuBiI_4 by fitting the powder diffraction pattern with a CdCl_2 -type rhombohedral structure ($R\bar{3}m$).^[69] At the same time, a recent theoretical study by Wang et al. predicted 15 possible low-energy crystal structures of CuBiI_4 .^[70] Initial screening based on the mechanical and dynamic stability proposed three new structures, $P\bar{1} - \text{II}$, $P\bar{1} - \text{III}$, and $P2_1/m$, as energetically and optoelectronically most favorable.^[70] Experimental evidence supporting these findings is yet to be obtained.

In 1991, Fourcroy et al. reported another composition of the copper(I) iodobismuthate family, viz. Cu_2BiI_5 .^[67] Ramachandran et al.^[71] recently synthesized and characterized thin films of this compound, which was found to have a hexagonal structure close to that of CdCl_2 .

An investigation of the phase diagram of the Cu-Bi-I ternary systems by Bahari et al. failed to find any ternary phases other than CuBiI_4 and Cu_2BiI_5 discussed above. At the same time, the first synthesis of Cu_3BiI_6 was reported by Baranwal et al.,^[72]

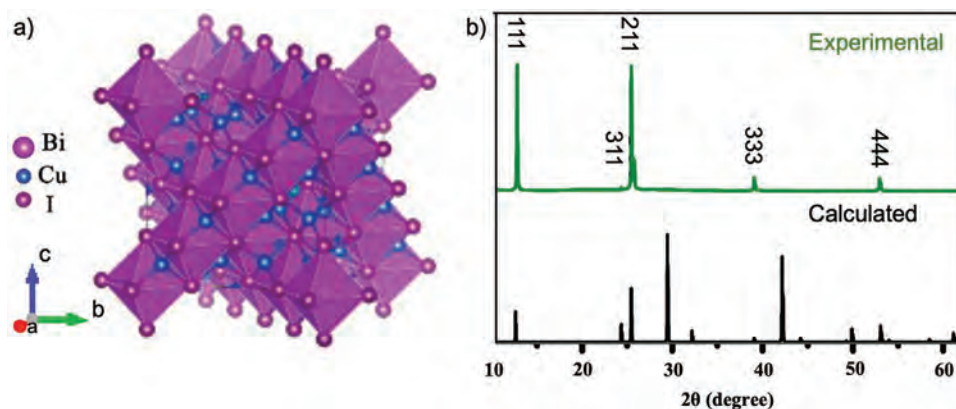


Figure 4. a) Crystal structure and b) XRD patterns of CuBi_4 . Reproduced with permission.^[66] Copyright 2018, John Wiley and Sons.

although no detailed structural information is available for this compound yet.

Minimal progress has been achieved in developing copper(I) antimony(III) iodide materials thus far. Jie and Ding reported on the previously undocumented XRD pattern of the material derived from the simple reaction between CuI and SbI_3 precursors in dimethylsulfoxide (DMSO). Although the authors proposed the formation of a new Cu_3SbI_6 phase, no detailed analysis of the crystal structure was undertaken.^[40] It is also important to note that no follow-up studies confirming the outcomes of this work have been reported since its publication in 2019.

Overall, the diversity of copper(I) pnictohalides discovered to date is lower than that of silver(I) iodobismuthates. Therefore, it is no surprise that a sufficiently deep understanding of the structure of the $\text{Cu}_x\text{Bi}_y\text{I}_{x+3y}$ materials is limited to CuBi_4 , which shares many similarities with the AgBi_4 analog. However, the reported data, even for this single composition, are still conflicting in the literature, including concerns about the phase stability of the material at room temperature. It is possible that the slower progress in discovering the Cu-based materials of this class is the consequence of the challenges of their synthesis and less impressive optoelectronic properties compared to silver iodobismuthates, as discussed in further detail in Sections 3 and 4.

2.3. Silver/Copper Pnictohalides with Mixed Cations and Anions

Compositional engineering by partial substitution of cations and/or anions in halide perovskites has been successfully used to fine-tune the microstructural and optoelectronic properties of these materials.^[73–75] Several groups have also implemented a similar approach to tailor the properties of silver/copper pnictohalides, with a major focus on silver iodobismuthates. These studies included mixing both A^+ and B^{3+} cations and the partial substitution of the iodide anion. Key structural features resulting from all three strategies are surveyed in this section.

2.3.1. Mixed Monovalent Cations

Several reports have explored the fractional substitution of Ag^+ with other monovalent cations. One approach that has attracted

some attention involves using Cs^+ as a substituent. The fractional substitution of Ag^+ with Cs^+ was first applied to AgBi_4 , where it was shown to lead to compounds with the general formula $[\text{Cs}_n\text{Ag}_{1-n}]\text{Bi}_4$. Yu et al. found that such compounds retain the cubic defect-spinel structure (with $Fd\bar{3}m$ symmetry) of the ternary parent silver iodobismuthate AgBi_4 , provided that the cesium(I) atomic fraction n remains below 0.1 (Figure 5a).^[76] Higher cesium amount resulted in the formation of $\text{Cs}_3\text{Bi}_2\text{I}_9$ as an impurity. The use of Cs^+ alone as the monovalent cation, i.e., aiming for the hypothetical cesium iodobismuthate $\text{Cs}_x\text{Bi}_y\text{I}_{x+3y}$, does not produce a defect-spinel or CdCl_2 -type structure. Instead, the resultant $\text{Cs}_3\text{Bi}_2\text{I}_9$ adopts a zero-dimensional structure consisting of isolated $[\text{Bi}_2\text{I}_9]^{3-}$ dimers, likely due to the larger ionic radius of Cs^+ (167 pm) compared to Ag^+ (115 pm).^[77] Finally, Yu et al. reported that no phase change occurs at low amounts of Cs^+ introduced ($n \leq 0.1$),^[76] but its presence improved the crystallinity of the resultant $[\text{Cs}_n\text{Ag}_{1-n}]\text{Bi}_4$ thin films, as concluded from the XRD analysis.

Fractional substitution of Ag^+ with Cs^+ was also applied to silver-rich Ag_2BiI_5 by Hosseini and Adelifard, who reported the formation of compounds with the formula $[\text{Cs}_n\text{Ag}_{2-n}]\text{BiI}_5$.^[78] Such compounds showed no phase change with respect to the parent material, as they retained the CdCl_2 -type rhombohedral structure of Ag_2BiI_5 with $R\bar{3}m$ symmetry. However, the incorporation of Cs^+ in to Ag_2BiI_5 was also found to change the relative intensity of the XRD peaks of the resultant $[\text{Cs}_n\text{Ag}_{2-n}]\text{BiI}_5$ in the thin-film form, revealing the impact of Cs^+ on the preferential growth of the material.

Zhang et al. attempted to incorporate Li^+ into the AgBi_4 lattice via the addition of LiI and LiTFSI (lithium bis(trifluoromethanesulfonyl)imide).^[79] Wang et al. systematically investigated the possibility of incorporating alkali metals into Ag-Bi-I ternary systems.^[80] The interstitial doping achieved by the team did not induce any structural changes; in fact, doping up to the level of 3 at.% improved the crystallinity of the Ag_2BiI_5 hexagonal phase in the order $\text{Cs}^+ > \text{K}^+ > \text{Rb}^+ > \text{Na}^+ > \text{Li}^+$.

Park et al. recently achieved partial substitution of Ag^+ by Cu^+ to enhance light-harvesting properties.^[81] The resulting $[\text{Cu}_n\text{Ag}_{2-n}]\text{BiI}_5$ films did not exhibit significant crystallographic changes or phase segregation other than the apparent structural contraction for doping concentrations up to 10 at.%.

Concurrently, Sansom et al. reported the first synthesis of the defect-spinel and CdCl_2 -type rhombohedral $[\text{CuAg}]\text{Bi}_5$

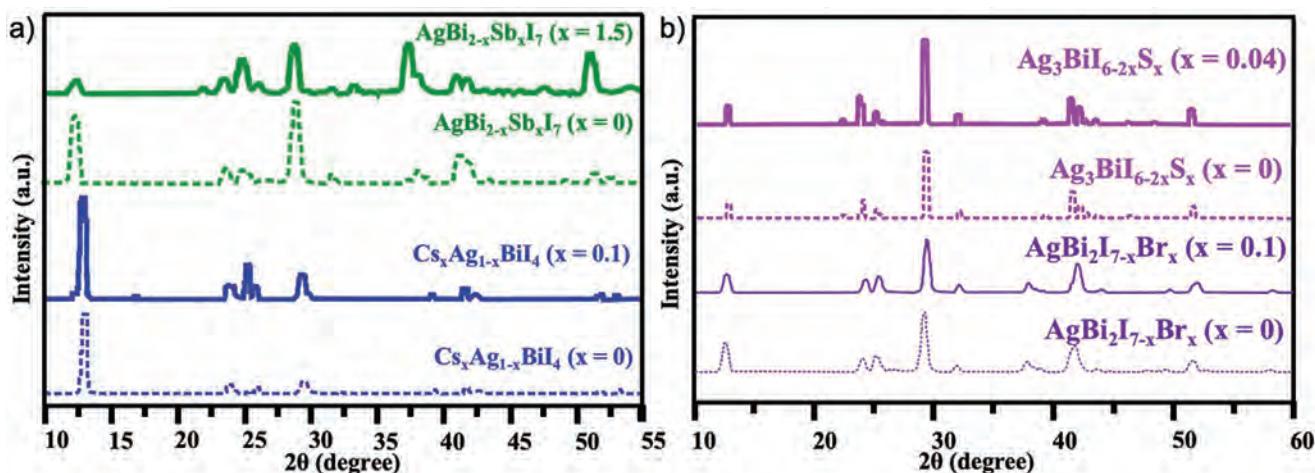


Figure 5. XRD patterns of group IB–group VA compositions with partially substituted a) cation sites: Cesium-doped $\text{Cs}_x\text{Ag}_{1-x}\text{BiI}_4$ with $x = 0$ and 0.1 (blue).^[76] Mixed antimony–bismuth $\text{AgBi}_{2-x}\text{Sb}_x\text{I}_7$, prepared using Sb-precursor concentration $x = 0$ and 1.5 (green).^[63] b) Anion site: sulfur-modified $\text{Ag}_3\text{BiI}_{6-2x}\text{S}_x$ with $x = 0$ and 0.04 (pink).^[42] Mixed halide $\text{AgBi}_2\text{I}_{7-x}\text{Br}_x$ with $x = 0$ and 0.1 (purple).^[84]

and $[\text{Cu}_2\text{Ag}]\text{BiI}_6$ materials.^[82] As mentioned above, the authors argued that CuBiI_4 is not stable and decomposes at room temperature. Hence, adding Ag^+ ions could stabilize CuBiI_4 , while Cu^+ addition could reduce the amount of silver in the compound. Based on single-crystal XRD (SCXRD), the authors suggested that the resultant material has four twinned cubic trigonal cells with the $R\bar{3}m$ space group. The twinning revealed two possible structural scenarios, viz. defect spinel or twinned CdCl_2 structure, which correlates with the previous explanation of the structure of AgBiI_4 by the same group.^[54] The incorporation of Cu^+ into AgBiI_4 or AgBiI_7 resulted in a decrease in the octahedral occupancy of Ag^+ and Bi^{3+} (≤ 40 at.%) and the formation of octahedral vacancies to form either three-dimensional cubic defect spinel $[\text{CuAg}]\text{BiI}_5$ or CdCl_2 -type $[\text{Cu}_2\text{Ag}]\text{BiI}_6$ two-dimensional octahedral networks.^[69] Interestingly, the structure of $[\text{Cu}_2\text{Ag}]\text{BiI}_6$ was found to have Ag^+ and Bi^{3+} cations occupying the edge-sharing octahedra in a disordered fashion separated by a layer of vacant octahedral sites, and the Cu^+ cations were found to occupy all possible tetrahedral sites with atomic occupancies of Cu^+ , Ag^+ and Bi^{3+} of 17.9%, 34.7%, and 30.6%, respectively.^[69] These relatively higher octahedral occupancies compared to CuBiI_4 (25%) could be one of the reasons for the improved phase stability of the Cu–Ag–Bi–I compositions.

2.3.2. Mixed Trivalent Cations

Substitution of Bi^{3+} with alternative trivalent cations in the $\text{Ag}_x\text{Bi}_y\text{I}_{x+3y}$ materials has primarily focused on antimony(III) as a partial substituent, but other possibilities have been considered as well. Compounds of this class investigated to date include $\text{Ag}[\text{Bi}_{2-m}\text{Sb}_m]\text{I}_7$, $\text{Ag}_2[\text{Bi}_{1-m}\text{Sb}_m]\text{I}_5$, and $\text{Ag}[\text{Bi}_{1-m}\text{Sb}_m]\text{I}_4$.^[62,63,83] In all three instances, the experimental results demonstrated successful incorporation of Sb^{3+} into the parent compound to form mixed B-cation materials while retaining the original cubic defect spinel structure (with $Fd\bar{3}m$ symmetry) for $\text{Ag}[\text{Bi}_{2-m}\text{Sb}_m]\text{I}_7$ (Figure 5a) and $\text{Ag}[\text{Bi}_{1-m}\text{Sb}_m]\text{I}_4$, and the rhombohedral structure (with $R\bar{3}m$ symmetry) for $\text{Ag}_2[\text{Bi}_{1-m}\text{Sb}_m]\text{I}_5$.

Iyoda et al. attempted to substitute bismuth in Ag_2BiI_5 with group III and group V elements for the B-site combinations of Bi + In, Ga + Sb, and Bi + Sb.^[83] However, the authors structurally characterized only materials based on the bismuth–antimony mix since these compounds exhibited the most promising optoelectronic properties. The specific composition analyzed was $\text{Ag}_2[\text{Bi}_{1-m}\text{Sb}_m]\text{I}_5$, which showed no change in the XRD pattern of Ag_2BiI_5 when m was not higher than 0.6. Increasing the Sb content above $m = 0.7$ resulted in XRD amorphous materials, preventing any conclusions on their structure.

2.3.3. Mixed X-site Anions

To date, attempts to partially substitute the X-site anions have been applied to silver bismuth iodides. Replacement of I^- with Br^- in $\text{AgBi}_2[\text{I}_{7-l}\text{Br}_l]$ materials up to $l = 0.6$ did not induce detectable changes to the crystal structure in the study by Wu et al.^[84] The iodide and mixed iodide–bromide materials exhibited the same cubic structure with $Fd\bar{3}m$ space group symmetry (Figure 5b). However, the smaller size of the bromide ions compared to iodide induced a slight contraction of the crystalline lattice, as concluded from the shift of the XRD reflections to higher angles. Additionally, it was observed that higher bromide concentrations induce the formation of AgI and BiBr_3 admixtures.

Apart from halogenides, the fractional substitution of I^- with sulfide dianions was investigated in an attempt to upshift the deep valence band edge (E_{VBM} below -5.6 eV) and decrease the bandgap of silver bismuth iodides, which limits the charge transfer and photovoltaic capabilities of these materials. An extreme point of comparison here is represented by the well-known and actively investigated silver–bismuth sulfides,^[85,86] which have a very narrow bandgap (<1.4 eV) along with a shallow valence band edge ($E_{\text{VBM}} > -5.2$ eV versus vacuum).^[85–87] Focusing on the major $\text{AgBi}[\text{I}_{4-2l}\text{S}_l]$, $\text{AgBi}_2[\text{I}_{7-2l}\text{S}_l]$, $\text{Ag}_2\text{Bi}[\text{I}_{5-2l}\text{S}_l]$, and $\text{Ag}_3\text{Bi}[\text{I}_{6-2l}\text{S}_l]$ compositions modified with low amounts of S^{2-} ($l \leq 0.06$), Pai et al.^[42] observed mixed defect

cubic spinel and trigonal structure with $R\bar{3}m$ space group symmetry that was not affected by partial anionic substitution (Figure 5b). However, substitution attempts over $l = 0.06$ led to phase segregation and amorphous materials. The authors further observed trace amounts of AgI in all samples, which were more pronounced in Ag-rich compounds (Ag_2BiI_5 , Ag_3BiI_6) as the sulfide contents increased.

In summary, incorporating monovalent cations with smaller ionic radii at the A-site, trivalent cations at the B-site, and monovalent or divalent anions at the anionic X-site does not generally induce significant structural distortion in silver bismuth iodides whenever the substitution level is sufficiently low. In fact, in some cases, the overall crystallinity of the materials is improved, disregarding structural contractions. However, attempts to introduce high concentrations of substituents result in phase segregation and reduction in crystallinity. The beneficial impacts of the anionic/cationic modifications on morphological and optoelectronic properties are discussed in Section 4.

3. Synthesis and Thin-film Deposition

The synthesis methods play a pivotal role in defining morphological and physicochemical properties, including the optoelectronic properties of materials. One can tailor the composition, morphology, and crystal structure of nanomaterials by adapting or modifying highly efficient, reproducible, and controllable synthesis and deposition strategies and thereby pave the way to understanding the intrinsic fundamental characteristics that lead to desired optoelectronic properties. Bottom-up synthesis methods (Figure 6), such as solvothermal,^[48,105] solid-state fusing (melt-crystallization),^[56,106,107] Bridgeman reaction,^[94] sol-gel,^[108,109] ligand-assisted hot-injection,^[12] chemical vapor transport (CVT),^[54,110] and aerosol methods,^[96] have been explored to synthesize single crystals, quantum dots and nanoparticles of silver/copper pnictohalides. In turn, polycrystalline thin films of these materials have been fabricated using various deposition strategies, such as spin-coating,^[66,68] direct metal surface elemental reaction (DMSER),^[101,102] and coevaporation.^[71,103] In regard to optoelectronic devices, the material and film qualities are critical, as they affect the series and shunt resistances,

carrier generation and extraction, recombination processes, and photon detection sensitivity. While phase-pure crystal growth commonly requires synthesis optimization or modification to attain a critical saturation point and nucleation, the film quality and coverage can be improved by accessing reliable and scalable solution- or vapor-based thin-film formation strategies.

Low-temperature solution-based methods are often preferable to produce silver/copper pnictohalide films due to their technical simplicity, cost-effectiveness, and potential for scale-up. However, a direct transition from the procedures established for lead/tin-halide perovskites to perovskite-inspired silver/copper pnictohalides is rarely possible, primarily due to the low solubility of their precursors and the possibility of forming compounds with close but different stoichiometry. Under these circumstances, the formation of pure single-phase compositions often presents a challenge. To address this, the effects of various synthetic parameters on the properties of the resulting films have been explored and modified by researchers to obtain phase-pure and conformal materials and fine-tune the optoelectronic properties to suit various applications. Apart from the solution-based fabrication strategies, coevaporation has proven to produce high purity films with reasonable control over stoichiometry and morphology.

In this section, we discuss the synthesis and deposition methods that have been developed for silver and copper pnictohalides while highlighting the strategies introduced to improve morphology and thereby the optoelectronic properties and device performance.

3.1. Silver(I) Pnictohalides

3.1.1. Single-crystal and Nanoparticle Synthesis

The synthesis of single crystals is typically pursued in studies aiming for an in-depth understanding of the structural parameters and physicochemical properties of novel compositions. Conventionally, solid-state fusing or melt-crystallization methods have been adopted to develop crystals and study their temperature-dependent phase diagrams. This approach is widely used to produce high-phase purity (>99.99%) crystals from melted metal precursors and is also considered

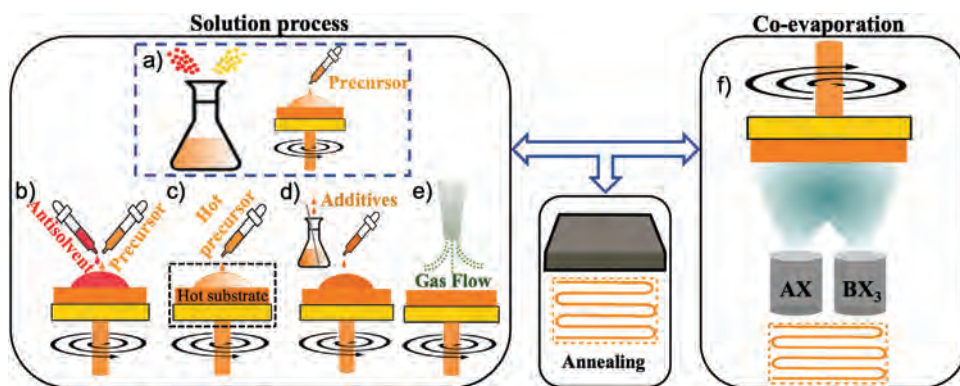


Figure 6. Schematic illustration of the deposition process for the silver/copper pnictohalide thin films via a) conventional spin coating; b) antisolvent-assisted spin-coating; c) dynamic hot casting; d) additive engineering; e) gas-assisted spin-coating; f) co-evaporation.

less complex than the solution processes since no solvents or additives are involved.^[106,107] Specifically, this method involves melting high-purity powders of the precursors of interest (at the desired molar ratios) in a vacuum-sealed quartz tube, followed by quenching to room temperature.

Fourcroy et al.^[55] and Dzeranova et al.^[56] developed AgBi₂I₇ and AgBiI₄ crystals, respectively, while Mashadieva and co-workers reported the synthesis of Ag₂BiI₅ and AgBi₂I₇ crystals using melt crystallization.^[49] Later, Sansom et al. obtained AgBiI₄ nanoparticles by reacting high purity (99.999%) AgI and BiI₃ at 610 °C for 24 h in vertically placed and vacuum-sealed long quartz tubes, cooling to 350 °C and keeping at this temperature for 120 h, and finally quenching in an aqueous bath at room temperature to avoid the formation of the BiI₃ and Ag₂BiI₅ impurities.^[54] Apart from the target AgBiI₄ phase, a minor admixture of fragile flat dendritic crystals of Ag-deficient AgBi₂I₇ was also formed at the top of the tube; the contribution of these compounds increased with the decrease in the AgI:BiI₃ ratio.

In their other work on silver iodobismuthate single crystals, Sansom et al. employed the chemical vapor transport (CVT) method.^[54,110] For the synthesis, vacuum-sealed quartz tubes were horizontally placed in a furnace with two temperature zones (363 and 350 °C; temperature gradient of 0.8 °C cm⁻¹), and the precursor powders were volatilized in the higher-temperature zone in the presence of a transport agent. The formed gaseous mixture was deposited at the lower-temperature part of the chamber, leading to the growth of the crystals. This strategy produced two different sets of black AgBiI₄ crystals: octahedral facets of ≈ 0.5 mm × 0.5 mm × 0.5 mm in size and elongated plate-like structures with lateral dimensions of ≈ 0.1 mm × 0.5 mm.^[54]

Turkevych et al. also adopted solid-state vacuum fusing to obtain black crystals of AgBiI₄, AgBi₂I₇, Ag₂BiI₅, and Ag₃BiI₆.^[43] Their study revealed that bismuth-rich compounds AgBiI₄ and AgBi₂I₇ could be obtained as single-phase materials. In contrast, the silver-rich compounds Ag₃BiI₆ and Ag₂BiI₅ always contained an AgI admixture, although present at a very low concentration in the latter case. At the same time, Ag₃BiI₆ was reported to exist as a pure phase at elevated temperatures above 127 °C.

Interestingly, Oldag and co-workers adopted a solvothermal technique to synthesize crystal structures of AgBiI₄ and Ag₃BiI₆ a decade before vacuum fusing and the chemical vapor transport methods discussed above were applied to this class of materials.^[48,105] Under solvothermal conditions, crystals grow in a solvent medium under high pressure and temperature, typically close to the boiling point of the reaction medium. This method enables control of the nucleation and growth of crystals by regulating various reaction parameters, such as the pH of the starting solution, temperature, pressure, reaction time, and concentrations of reactants and other chemicals present.^[111,112] Grayish black octahedral crystals of AgBiI₄ and hexagonal/trigonal platelets of Ag₃BiI₆ have been synthesized using this method, where the precursors were dissolved in a 20 wt.% HI aqueous solution at 160 °C.^[48] The study revealed a close structural relationship between AgBiI₄ and Ag₃BiI₆, with AgBiI₄ having a higher degree of structural order.

Daniilović and colleagues introduced a strategy for the synthesis of Ag₃BiI₆ nanoparticles (Figure 7d).^[96] This team

developed a ligand-free aerosol method by applying an atomizer to a clear solution of AgI and BiI₃ in DMSO and passing the generated aerosol drops through a hot (120 °C) metallic tube and discarding the solvent using a cold trap.

The traditional vertical Bridgman method was employed by Tie et al. to prepare single crystals of AgBi₂I₇ (Figure 7e).^[94] In this decades-old classical solid-state procedure,^[113,114] nucleation is initiated while melting precursor materials in sealed quartz ampoules. The rod/columnar growth occurs as the nucleation propagates through the entire molten material. By applying this method to the synthesis of silver bismuth iodides, the authors obtained single crystals of 14 mm in width and length, which were cut using a diamond wire saw and polished with dustless cloth and isopropanol.^[94] The size and shape of the crystals produced with this method are to a significant extent determined by the dimensions of the ampoule used for the synthesis.

Finally, the synthesis of silver antimony iodide by a solid-state reaction was reported by Gray et al.^[62] By heating grounded metal halide precursors in a vacuum-sealed silica ampule at 125 °C for 18 h, polycrystalline AgSbI₄ was obtained. The team demonstrated the same approach for producing AgBiI₄, with the only difference being the synthesis temperature of 175 °C.

3.1.2. Quantum Dot Synthesis

Premkumar et al. synthesized nanocrystals (quantum dots) of AgBiI₄, AgBi₂I₇, and Ag₂BiI₅ via a modified ligand-assisted reprecipitation method (Figure 7a–c).^[12] The reaction was initiated by rapid injection of oleylamine and oleic acid dissolved in hot ethyl acetate into a low concentration silver(I) (0.1 mM) and bismuth(III) (2 mM) iodide precursor solution in dimethylformamide (DMF). Oleylamine and oleic acid act as stabilizers and control the size of the nanoparticles by suppressing agglomeration. Recently, the same team presented a modified solvothermal method by changing the ligand to oleylaminesulfide for improved photoelectric properties and obtained nanocrystals with an average size of ≈ 5 nm.^[115]

Overall, solid-state synthesis methods enable the formation of phase-pure crystals. However, high energy intensity and cost associated with the use of high vacuum and high-temperature conditions limit their extension toward practical applications. Nevertheless, the solid-state methods are more reliable and reproducible for synthesizing silver pnictohalide crystals compared to the solvent-based methods discussed in the following section.

3.1.3. Thin Film Deposition: Solution-Based Routes

The ability to produce semiconducting materials in the form of very thin, compact films opens up opportunities for many optoelectronic applications. Such morphology can be achieved using solution-based methods, which can also be considered suitable for scale-up as facile and low-cost fabrication approaches. Several factors define the quality of the thin films and thereby their optoelectronic properties, including purity and solubility of the precursors, chemical coordination of the precursors with solvents, viscosity and stability of solutions, boiling point and

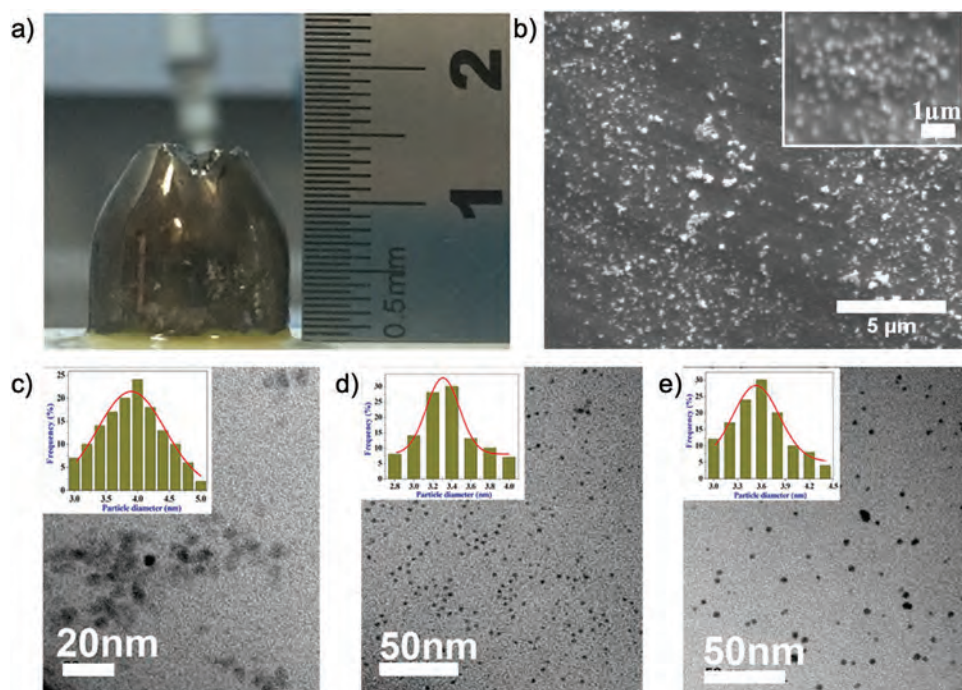


Figure 7. a) Photograph of the AgBi_2I_7 crystals. Reproduced with permission.^[94] Copyright 2020, American Chemical Society. b) SEM images of Ag_3BiI_6 . Reproduced with permission.^[96] Copyright 2020, American Chemical Society. HRTEM images of silver bismuth iodide samples at the Ag:Bi atomic ratios of c) 1:1 (AgBiI_4), d) 2:1 (Ag_2BiI_5), and e) 1:2 (AgBi_2I_7). Reproduced with permission.^[12] Copyright 2020, American Chemical Society.

polarity of solvents, deposition environment, post-treatment parameters such as annealing temperature and time.

Single- or two-step deposition strategies are usually adopted for producing semiconductor thin films, including silver/copper pnictohalides. Single-step deposition is often used for silver-based compounds, in which halide precursors are dissolved in suitable organic solvents, e.g., a mixture of DMF and DMSO, and deposited on substrates by spin-coating or drop-casting followed by annealing at moderate temperatures in the range of 100–200 °C (Figure 6a). A broad range of parameters can be optimized to decrease the energy barrier for nucleation and promote conformal crystal grain growth. These parameters include but are not limited to precursor concentrations, spinning settings, chemical nature of the solvent and additives, post-deposition treatment, the use of antisolvent or gas-assisted solvent evaporation, and the preannealing temperature of the substrate and the solution (for the so-called hot casting method). Since nucleation and grain growth are to a major extent defined by the chemical interaction between the precursors, solvent, and substrate, changes in the conditions listed above alter the kinetics of these processes by controlling the rate of the solvent evaporation rate to achieve supersaturation. Hence, optimization of the deposition parameters is always necessary to obtain thin films with desirable uniform morphology.

Precursors of silver(I) pnictohalides, AgI and AgBr, have low solubility in commonly used polar aprotic solvents such as DMSO and DMF, which naturally limits their use for the solution-based methods of synthesis. Hence, primary alkylamines such as *n*-butylamine were employed in the initial studies to prepare phase-pure silver bismuth halide films.^[41,57,59] However,

the coverage of the substrate with the material achieved with this solvent was unsatisfactory due to uncontrolled crystallization (Figure 8a).^[57] This morphology, which is highly unfavorable for the photovoltaic performance, was explained by the relatively low boiling point of the solvent (78 °C) and the formation of a strong BiI_3 -*n*-butylamine-AgI adduct, whose decomposition into the target silver iodobismuthate required a high temperature of 150 °C.

Another obvious strategy to improve the solubility of precursors is to increase the temperature, which was indeed found to be effective for the preparation of clear solutions of silver(I) and bismuth(III) halogenides in solvents convenient for spin-coating and similar methods (such as DMSO and DMF) by heating at 70–110 °C for less than 30 min. The enhancement in solubility was attributed to the formation of an adduct of BiI_3 and DMSO, a Lewis base, and $[\text{BiI}_{3+x}]^{x-}$ coordination complexes that accelerate the dissolution of AgI.^[43] Such solutions produced films with fewer pinholes, larger grains, and complete substrate coverage compared to those prepared with *n*-butylamine (Figure 8b).^[57] In contrast to *n*-butylamine, the decomposition of the DMSO-precursor adduct required a much lower film annealing temperature of 90 °C, resulting in highly crystalline silver iodobismuthate films. Recently, Kulkarni et al.^[57] studied the effects of solvents on the crystallization of $\text{Ag}_x\text{Bi}_y\text{I}_{x+3y}$ and found that the presence of DMSO in multicomponent solvent systems (e.g., in a 1:1 vol. mixture with DMF) reduces the phase segregation and formation of pinholes in the films. This positive effect was attributed to the higher boiling point of DMSO and the formation of the BiI_3 -DMSO-AgI intermediate adduct. At the same time, the use of DMSO solutions, in contrast to *n*-butylamine,

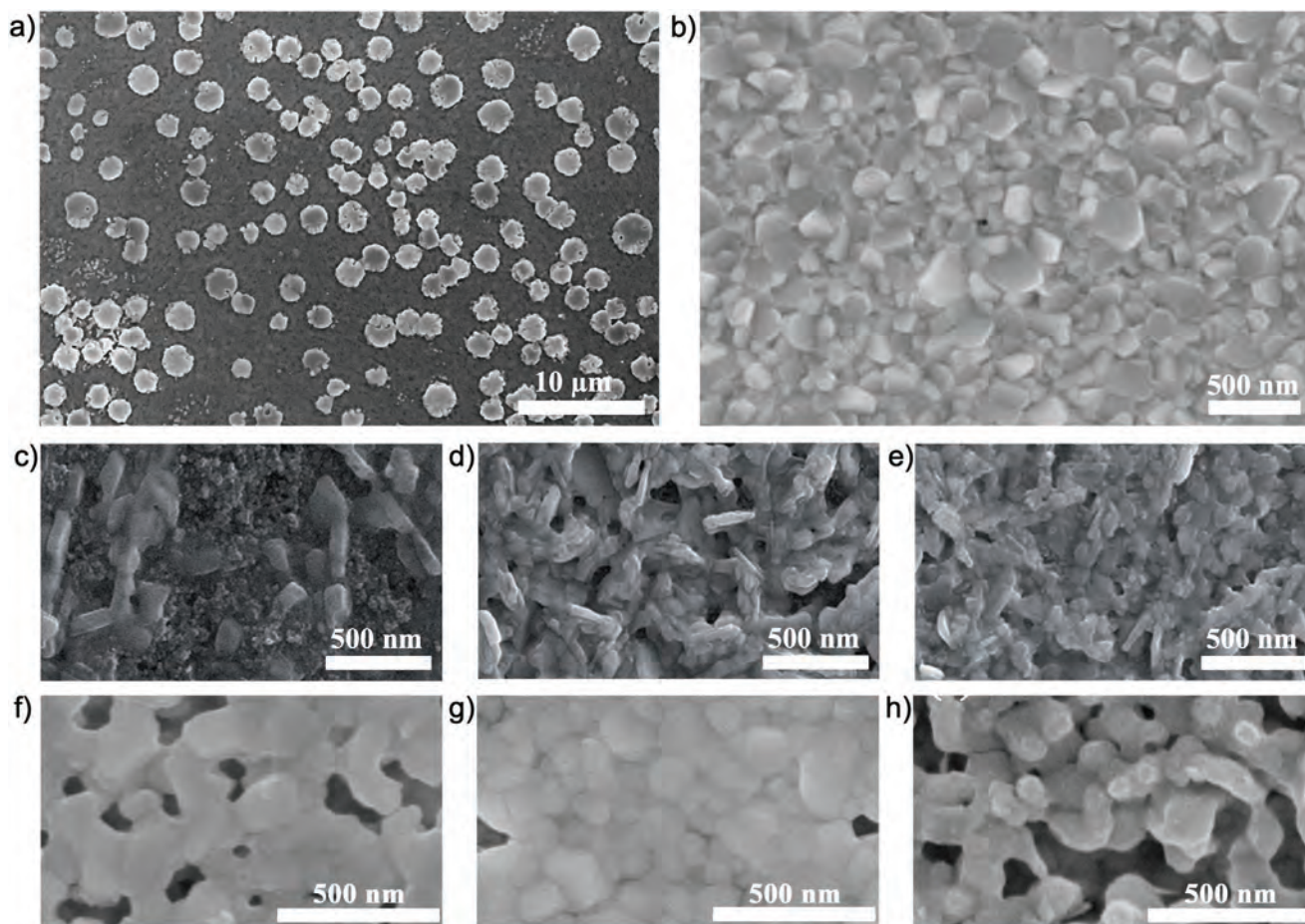


Figure 8. SEM images of AgBi_2I_7 thin films prepared using a) *n*-butylamine and b) DMSO as solvents. Reproduced with permission.^[57] Copyright 2019, The Royal Society of Chemistry. Ag_2BiI_4 thin films produced using different precursor concentrations of c) 0.2 M, d) 0.4 M, and e) 0.5 M. Reproduced with permission.^[53] Copyright 2019, The Royal Society of Chemistry. AgBiI_4 films prepared using a precursor concentration of 0.6 M and post-annealed at f) 130 and g) 150 and h) 180 °C. Reproduced with permission.^[89] Copyright 2018, American Chemical Society.

was found to produce films contaminated with BiI_3 , which was found to negatively affect charge transport properties.^[57]

The initial concentration of the precursor solutions is also a critical parameter. A higher starting concentration might result in the rapid formation of smaller crystals that tend to agglomerate, while a lower concentration might promote slower growth of larger crystals, leading to nonuniform coverage. For example, it was reported that a low precursor concentration of 0.2 M (Figure 8c) produced a Ag_2BiI_5 film that covered only half of the underlying mesoporous TiO_2 layer.^[53] As the concentration was increased to 0.4 M (Figure 8d), significantly improved coverage was reported, albeit small pinholes ($\approx 50\text{--}80$ nm) were still present. Complete coverage was achieved when the concentration was 0.5 M (Figure 8e), but a further increase in concentration was not possible due to the limited solubility of the precursors. As expected, the increase in the precursor solution concentration from 0.2 to 0.5 M also increased the thickness of the films from ≈ 30 to 150 nm.

The post-annealing temperature defines the evaporation rate of the residual solvent in the coated films, affecting the grain size and uniformity of the thin films. Lu et al. studied the effect of the post-annealing temperature in the 130–180 °C

range on the characteristics of AgBiI_4 deposited by spin-coating (Figure 8f–h).^[89] The use of the lowest temperature produced films of smaller grains (≈ 50 nm) with pinholes (Figure 8f), while the highest temperature resulted in island-type grain coverage due to excessively rapid crystallization (Figure 8g). Smooth pinhole-free films of larger grains (≈ 70 nm) with high crystallinity were produced at the optimal temperature of 150 °C (Figure 8h).

The use of additives to facilitate the dissolution of the precursor salts and/or improve the silver bismuth iodides was also explored (Figures 6d and 9). The addition of ≤ 12 vol.% hydroiodic acid to the mixed DMSO-DMF (at a 3:1 vol. ratio) precursor solutions was reported to improve the solubility of AgI and, consequently, the crystallinity and morphology of the films (Figure 9a,b).^[42,92] Hydrochloric acid was also found to have a similar positive effect on the properties of the $\text{AgBi}_{1-x}\text{I}_{3x+1}$ ($1 \leq x \leq 2.25$) films when using DMF as a solvent.^[39] The introduction of lithium bis(trifluoromethylsulfonyl)imide (LiTFSI) as an additive to AgBiI_4 precursor solutions was reported to eliminate pinholes and allow for the formation of dense thin films with complete coverage of a compact tin(IV) oxide substrate (Figure 9c,d).^[79] This significant improvement that led to

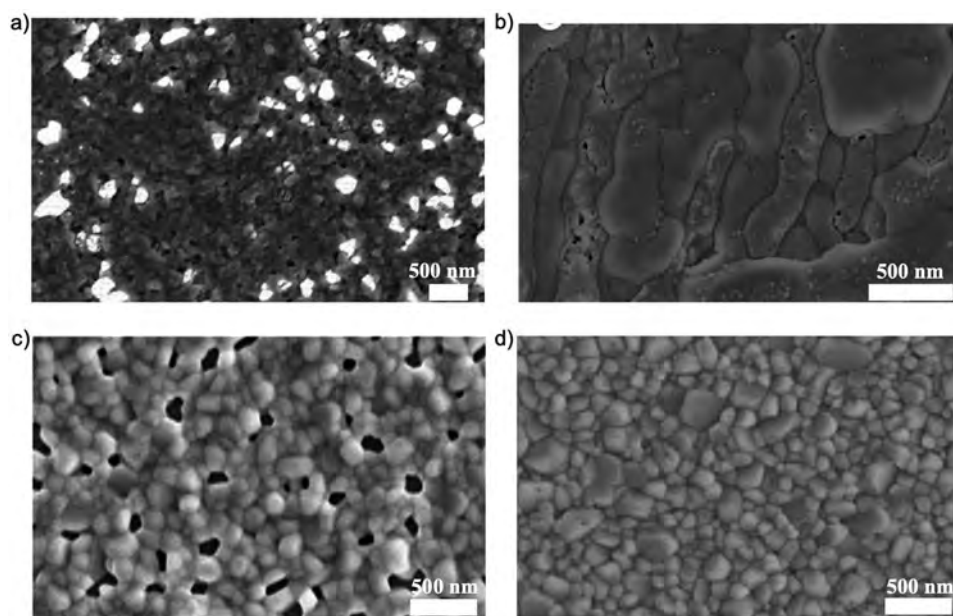


Figure 9. Sulfur-modified Ag_3BiI_6 thin films prepared by a) without and b) with HI. Reproduced with permission.^[42] Copyright 2018, John Wiley and Sons. SEM images of the AgBiI_4 films prepared c) without and d) with 2 wt.% lithium bis(trifluoromethylsulfonyl)-imide (LiTFSI) additive. Reproduced with permission.^[79] Copyright 2019, American Chemical Society.

enhanced device performance was attributed to the presence of the TFSI^- anion, which coordinates with the Ag-Bi-I solvent adduct and controls the crystallization. The use of excessively high (≥ 3 wt.%) LiTFSI concentrations deteriorated the film quality, which was explained by the hydrophilicity of this salt. Finally, Hosseini et al. reported incorporating multiwalled carbon nanotubes and reduced graphene oxide in precursor solutions for the synthesis of Ag_2BiI_5 films with significantly improved morphology.^[116]

By adopting strategies developed for halide perovskites and related materials, the quality of the silver/copper pnictohalide films was also improved by introducing antisolvents^[117] (Figure 6b) and flowing gas (Figure 6e),^[118] and through optimization of the duration of the solution dropping during spin-coating. Antisolvents such as chloroform, chlorobenzene, and toluene were used to prepare silver iodobismuthate films of various compositions with Ag:Bi = 1:2, 2:1, 1:1, and 3:1 by Pecunia and colleagues.^[68] More recent work by Iyoda et al. studied the effect of toluene, *n*-hexane, diethyl ether, dichlorobenzene, chloroform, chlorobenzene, and anisole as antisolvents on the optoelectronic performance (such as charge carrier generation efficiency and carrier lifetime) of Ag_2BiI_5 using time-resolved microwave conductivity (TRMC).^[83] From this analysis,^[42,88,92] the authors suggested that toluene produces films with the highest charge generation and mobility and the lowest concentration of traps and recombination rate among the examined antisolvents. The physicochemical origin of this promoting effect of toluene is yet to be established, and the overall understanding of the relationships between the properties of antisolvent and the characteristics of the resulting silver pnictohalide films is far from complete. Nevertheless, the general criteria for selecting a suitable antisolvent from an empirical perspective are well known: to promote the formation of high-quality dense films, the antisolvent should have a boiling point lower than that

of the solvent and should not dissolve the final product to accelerate nucleation.

Another strategy to achieve better coverage via spin-coating is dynamic hot casting (Figure 6c), where the preheated precursor solution is dropped onto a heated substrate while spinning. In conventional spin coating, nucleation begins as soon as the precursor solution is dropped on the substrate, leaving excess solvent trapped underneath the active layer formed. These trapped solvents are removed upon further film annealing, thus leaving behind extensive pinholes. The idea behind the dynamic hot casting method is to delay nucleation so that the excess solvent can be removed during spin-coating. However, as the spin-coating process proceeds and the excess solvent is removed, the solvent on top of the substrate becomes oversaturated, thus leading to nucleation. Following this approach, pinhole formation can be prevented, and films with larger grains can be obtained. Additionally, preheating of coated solutions improves the solubility of the silver pnictohalide precursors in aprotic organic solvents. Since the dynamic hot casting process takes place on the surface of mesoporous TiO_2 instead of the top of the photoactive film, nucleation begins in a short time with minimal solvent trapped. Hence, the preheating temperature, solution concentration, and drop speed are all crucial parameters that define the morphology of the resultant films. This method was reported to produce dense AgBiI_4 and Ag_2BiI_5 thin films with micrometer-sized grains under ambient atmosphere (Figure 10a,b).^[88,93]

The use of gas-assisted spin-coating (Figure 6e) also improves the morphology and coverage of the silver bismuth iodide films. In this procedure, an inert gas, such as argon, is blown onto the substrate while spin-coating to accelerate oversaturation by stimulating evaporation of solvents such as DMSO and DMF, which have relatively high boiling points. The gas flow parameters, viz. the rate, distance, and duration all significantly affect the crystallization rate and coverage (Figure 10c,d).^[118]

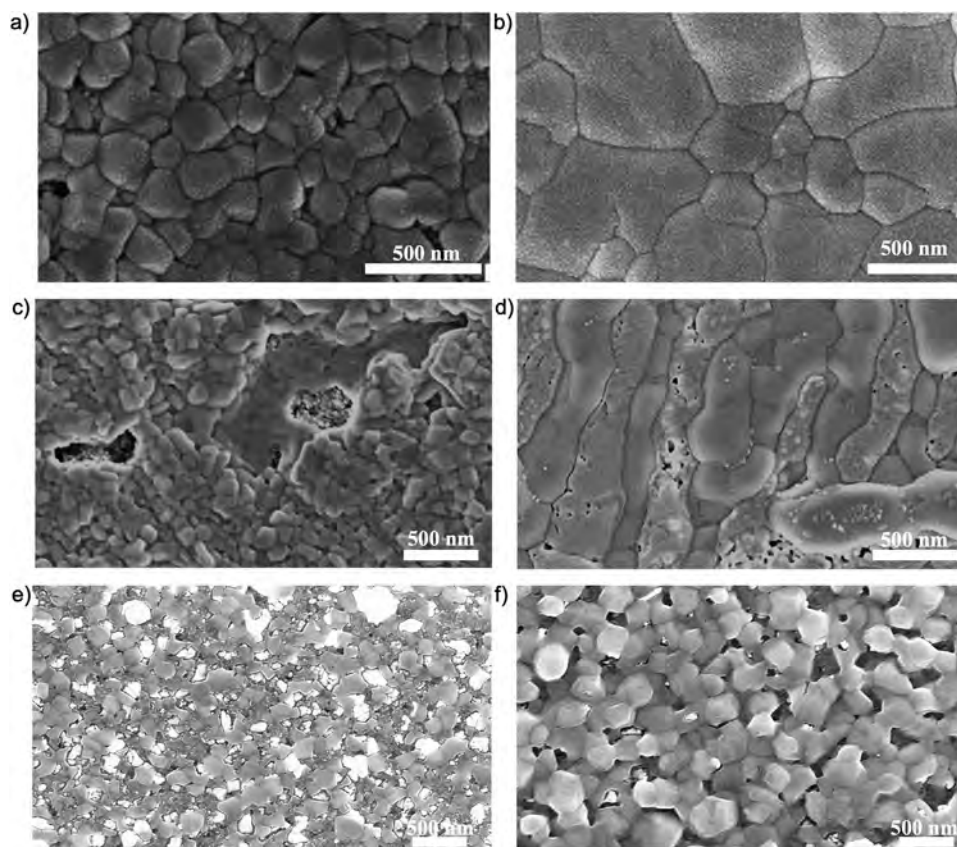


Figure 10. SEM images of a) conventional spin-coated and b) dynamic hot-cast Ag_2BiI_5 films. Reproduced with permission.^[88] Copyright 2018, John Wiley and Sons. c) Normal spin-coated and d) gas-assisted spin-coated sulfur-modified Ag_3BiI_6 films. Reproduced with permission.^[42] Copyright 2018, John Wiley and Sons. e) Antisolvent-assisted and f) hot-cast Ag_2BiI_5 films. Reproduced under the terms of the Creative Commons Attribution 4.0 International license.^[92] Copyright 2020, Pecunia et al.

Pecunia and co-workers^[92] compared the properties of Ag_2BiI_5 films on mesoporous TiO_2 (m- TiO_2) prepared using antisolvent and hot-casting methods (Figure 10e,f) as well as conventional spin-coating with the addition of hydroiodic acid to the precursor solution. The authors concluded that the first two techniques produced domains of the target compound that had feature sizes in the range of 10–300 nm and were contaminated with AgI. At the same time, the simple spin-coating of the HI-containing solutions led to a dramatic increase in the crystallization rate of silver bismuth iodides without any identifiable impurity phase.

The aforementioned thin-film deposition methods were also extended to produce Bi-rich compositions, such as $\text{AgBi}_3\text{I}_{10}$ and $\text{Ag}_2\text{Bi}_3\text{I}_{11}$, using *n*-butylamine, DMSO, DMF, and their mixtures as solvents.^[97,99] Yi et al. obtained nearly uniform $\text{AgBi}_3\text{I}_{10}$ films containing 300–800 nm-sized grains using conventional one-step spin-coating with *n*-butylamine as the solvent and by controlling the post-annealing temperature and duration.^[95] Shao and co-workers used an HCl additive in DMF solutions of silver and bismuth iodides to develop well-crystallized $\text{AgBi}_y\text{I}_{1+3y}$ ($1 \leq y \leq 2.25$) thin films by conventional spin-coating.^[51] Recently, Shadabroo et al. correlated the structural properties of AgBiI_4 , Ag_2BiI_5 , and AgBi_2I_7 films produced by one-step spin-coating with the temperature and duration of post-annealing as well as with the chemical nature of the solvent used. The

authors reported that the morphology and crystallinity of the films could be improved with increasing annealing temperature (from 100 to 150 °C) and duration (from 10 to 30 min). In addition, excess DMSO in the mixed solvent system was suggested to reduce the amount of phase impurities and pinholes in the films, probably due to the formation of BiI_3 -DMSO-AgI adducts. *n*-Butylamine was reported to be beneficial for synthesizing quality silver bromobismuthate films under the conditions used by the authors^[99] contrasting some of the previous reports.^[57]

Finally, a recent study by Prasad et al. highlighted the low-temperature preparation of high-quality silver bismuth iodide films using aqueous precursor solutions, which are of course highly advantageous from applied and environmental perspectives.^[38] The substrate was placed in a solution containing bismuth(III) and silver(I) nitrates along with nitric acid, to which potassium iodide was added to initiate the formation of a silver bismuth iodide film, which occurred over a few hours. The as-prepared films of AgBiI_4 and Ag_2BiI_5 contained ellipsoidal grains with a size of ≈ 60 –80 nm. Upon annealing at 125 °C for 15 min, the ellipsoidal grains acquired hexagonal shapes and a significant increase in the size and packing density of the grains was observed. The grain size of the annealed AgBiI_4 films was in the range of 70–200 nm, while the annealed Ag_2BiI_5 films contained grains with dimensions exceeding 300 nm. This pro-

cess offers improved control over the stoichiometry of the final film to achieve a single-phase, compositionally pure silver bismuth iodide using aqueous precursor solutions.

3.1.4. Quantum-Dot-Based Thin Film Deposition

Apart from the conventional solution-based processes discussed above, AgBiI_4 , AgBi_2I_7 , and Ag_2BiI_5 films were also produced by spin-coating dispersions of corresponding nanoparticulate precursors obtained via the modified ligand-assisted reprecipitation process described in Section 3.1.2 above. This strategy was applied to compact TiO_2 substrates used to produce optoelectronic devices.^[12] The quantum-dot-based film fabrication approach enables the formation of pure nanocrystal films, which are primarily defined by the composition of the nanoparticulate precursor rather than the solvent evaporation and postannealing conditions. Furthermore, these quantum dots allow tuning of the optoelectronic properties and reduce the nonradiative recombination with size and ligand modifications.

3.1.5. Vacuum-Based Methods

Unlike solution-process methods, vacuum-based thermal evaporation (Figure 6f) does not require toxic solvents and provides a higher level of control over the film thickness and morphology. Thermal evaporation also enables the multilayer deposition of films with the desired thickness without damaging the underlying layer(s).^[120]

Khazaee et al. introduced the evaporation method for silver pnictohalides by depositing films of AgBi_2I_7 , AgBiI_4 , and Ag_2BiI_5 with varied deposition rates of the AgI and BiI_3 precursors (ratio of the $\text{AgI}:\text{BiI}_3$ deposition rate, $r = 0.2, 0.6, 0.8$ and 1.2).^[90] The as-deposited films contained relatively small grains of ≈ 100 nm in size, regardless of the deposition rate ratio. Subsequent annealing at 180°C for 15 min under N_2 for bismuth rich films ($r = 0.2, 0.6$) and in excess BiI_3 vapors for silver-rich films ($r = 0.8, 1.2$) increased the grain size to $\approx 3\ \mu\text{m}$ ($r = 0.2, 0.6$) and 300 nm ($r = 0.8$) and eliminated pinholes. However, silver-rich films with $r = 1.2$ contained smaller grains (<100 nm) and pinholes. Turkevych et al. reported the synthesis of quality AgBiI_4 films by evaporation of silver and bismuth metals ($>99.99\%$), treating the bimetallic precursor with I_2 vapor at 40°C inside a glove box, and final annealing at 110°C .^[121]

Notwithstanding all the advantages provided by the vacuum-based thermal evaporation methods, the number of reports building upon this strategy for synthesizing silver pnictohalides beyond Bi-I-based compositions, and even for the $\text{Ag}_x\text{Bi}_y\text{I}_{x+3y}$ family, is limited.

3.1.6. Summary

Over the past several years, research on silver pnictohalides has substantially advanced the arsenal of methods available to synthesize these materials. The key challenges that were resolved are the low solubility of precursors, phase purity, and control over stoichiometry of the final product. In addition, several

fabrication methods have been developed to enable the deposition of thin and uniform films with sufficiently large grain sizes. Nevertheless, most of these procedures pertain to the domain of laboratory research, while their scalability presents a range of challenges discussed above. Therefore, if the commercialization of silver pnictohalogenides is pursued in the future, further efforts will be required to develop scalable and cost-effective synthetic approaches.

3.2. Copper(I) Pnictohalides

3.2.1. Single-Crystal and Nanoparticle Synthesis

Similar to silver pnictohalides, initial reports on copper bismuth iodides used melt-crystallization synthesis of single crystals and aimed to understand the phase diagram of the system and structural parameters of new phases. Fourcroy et al.^[67] and Bahari et al.^[104] studied copper bismuth iodide single crystals generated via solid-state melt crystallization of metallic precursors and reacting them in an iodine environment under vacuum at temperatures over 327°C . While the former team investigated the structural parameters of CuBiI_4 , the latter focused on the CuBiI_4 and Cu_2BiI_5 compositions and established a phase diagram of the Cu-Bi-I system via differential thermal analysis (DTA) and XRD measurements. Sansom et al. explored the structure and stability of CuBiI_4 while investigating the CuI-AgI-BiI_3 combinatorial systems.^[69,82] To this end, the authors synthesized CuBiI_4 crystal and powder samples by melting copper(I) and bismuth(III) iodides in sealed tubes at 610°C overnight and subsequently cooled down to 350°C . This temperature was further maintained for 5 days, and then the samples were quickly quenched to room temperature by immersing ampoules in water, leading to the formation of a black powder.

Unfortunately, no other single crystal growth or nanoparticle synthesis reports of copper pnictohalides are currently available in the literature to the best of our knowledge. This limits a deeper structural understanding of these systems.

3.2.2. Thin-Film Deposition: Solution-based

In 2017, Baranwal et al.^[72] reported on the first solution-based synthesis and deposition of Cu_3BiI_6 using the optimized ratio of the CuI and BiI_3 precursors in DMSO. However, the first structural confirmation of the formation of a solution-processed copper bismuth iodide (CuBiI_4) was provided by Hu et al. in 2018.^[66] Akin to AgI , the solubility of CuI in aprotic organic solvents is limited, and special measures need to be applied to facilitate the effective synthesis of copper pnictohalides. For example, Hu and coworkers reported the improved solubility of CuI and BiI_3 powders in *N,N*-dimethylacetamide (DMA) with the addition of HI ,^[66] which was attributed to the high solubility of hydrogen diiodocuprate (HCuI_2) and hydrogen tetraiodobismuthanuide (HBiI_4) in this solvent. While the conventional one-step spin-coating of such a precursor solution resulted in films with poor coverage and many pinholes (Figure 11a), employing tributyl phosphate as a solvent and vapor-assisted

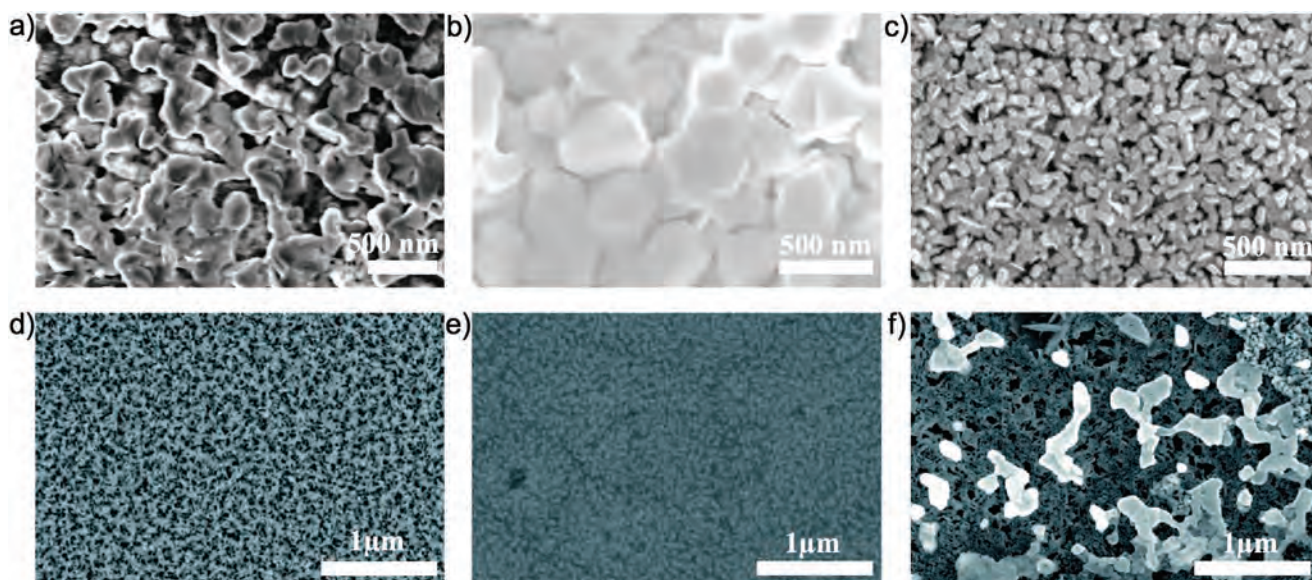


Figure 11. SEM images of the CuBi_4 thin films prepared by a) conventional thermal annealing and b) solvent vapor annealing (SVA). Reproduced with permission.^[66] Copyright 2018, John Wiley and Sons. c) SEM image of the CuBi_4 prepared by elemental powder reaction. Reproduced with permission.^[102] Copyright 2020, The Royal Society of Chemistry. SEM images of the spin-coated Cu_3SbI_6 films d) without heat treatment and annealed at e) 70 °C and f) 100 °C. Reproduced with permission.^[40] Copyright 2018, Springer Nature.

post-annealing significantly improved the grain growth and coverage (Figure 11b). The high vapor pressure of tributyl phosphate facilitated the preparation of films at low temperature (≤ 70 °C), as the solvent vapors restricted rapid crystallization and provided improved substrate coverage. The precursor concentration was also found to significantly affect the film quality: an increase in the precursor concentration from 0.4 to 0.7 M improved the size of the grains (from 150 to 300 nm) and produced more compact films with a lower concentration of pinholes and a higher degree of crystallization.

Later, Qu et al. used elemental Bi^0 , Cu^0 , and I_2 as precursors to form CuBi_4 films (Figure 11c). The precursor powders were first mixed by stirring the solid powders for 10–24 h and then dissolved in DMF and glacial acetic acid to form a transparent solution.^[102] The role of glacial acetic acid was to suppress the formation of the by-product BiOI . Films were deposited from this varied Cu:Bi ratio mixture by spin-coating using chlorobenzene as an antisolvent and subsequently annealed at 70 °C for 5 min. Film color changed from red to gray with the introduction of antisolvent, and dense films with improved coverage were obtained with the increase in the molar ratio of Cu:Bi (0.4:1 to 1:1).

Recently, Ramachandran et al. demonstrated a solution-process + thermal evaporation strategy to obtain phase-pure Cu_2BiI_5 films.^[71] In this approach, BiI_3 film was produced by spin-coating a high concentration (1 M) precursor solution in DMF and then used as a substrate for evaporation of copper under a high vacuum. After postannealing at 100 °C for 30 min, the films promote Cu diffusion and thereby Cu_2BiI_5 formation; additionally, an increase in the thickness of the Cu layer (from 50 nm to 100 nm) improves the compactness of the films.

Antimony-based copper pnictohalide Cu_3SbI_6 has also been synthesized via spin-coating of DMSO-based precursor solutions and subsequent thermal treatment.^[40] Before annealing,

the films exhibited nonuniform coverage (Figure 11d). Upon heat treatment at a low temperature of 70 °C, uniformly distributed small grains of 50 nm were formed (Figure 11e). Further annealing at a higher temperature of 100 °C resulted in the decomposition of the compound, leading to the formation of agglomerates and voids (Figure 11f), which was additionally verified by measurements of the surface roughness of the films.

Although research on copper pnictohalides is significantly less intense than on their silver-based counterparts, several interesting solutions to overcome the solubility and stoichiometric problems during solution-processable synthesis have been introduced. These developments building upon the use of unconventional solvents, postannealing strategies for controlling crystallization, and a combination of evaporation and solution processes might promote further innovation in the synthesis of stoichiometrically different copper pnictohalide compositions and understanding of their fundamental properties.

3.2.3. Thin-Film Deposition: Vapor-Based

Distinct from silver pnictohalides, metallic copper and bismuth rather than their iodide salts were primarily employed to synthesize copper pnictohalides by thermal evaporation due to the challenges of the use of copper(I) iodide precursors with this method.^[101] In this modified route, a direct metal surface elemental reaction (DMSER) via evaporation is typically conducted to achieve thin films of metallic alloys to fabricate various chalcogenide and iodide thin films.^[122–124]

Following this strategy, Zhang et al. produced Cu-Bi alloy thin films by magnetron sputtering under argon, which was then treated with iodine vapors inside the glove box at room temperature for 10 hours.^[101] Interestingly, the CuBi_4 films deposited on ITO displayed a rough surface with pinholes,

while a uniform, dense, and pinhole-free film was observed after the deposition of spiro-OMeTAD. The authors attributed this to the dissolution and recrystallization of CuBiI_4 in the presence of 4-*tert*-butyl pyridine (*t*BP), acetonitrile, and spiro-OMeTAD. Later, Yu and co-workers modified this method by varying the Cu:Bi ratio to obtain films with a bismuth concentration gradient. The metal ratio was varied by depositing a copper layer of different thicknesses (10–30 nm) on top of a 60 nm bismuth layer and exposing the resulting material to the I_2 vapors for various periods (18–30 h).^[103] Implementation of this strategy improved the morphology and several optoelectronic properties of the films, as discussed in Section 4 below.

Thus, the new thermal evaporation strategies were adequate for the efficient control over stoichiometry, thickness, and phase purity of the Cu-Bi-I materials. Furthermore, these methods enable tuning of the optoelectronic properties of the materials and allow for the design of new device architectures to support further insights into these novel materials.

3.3. Silver/Copper Pnictohalides with Mixed Cations and Anions

3.3.1. Mixed Monovalent Cations

Fractional substitution of Ag^+ by Cs^+ in silver iodobismuthate AgBiI_4 can be accessed by adding different molar concentrations of CsI to AgI/BiI_3 precursor solutions in DMSO used for spin-coating, as reported by Yu et al.^[76] Upon resting for 5 min at 35 °C and annealing at 130 °C for 15 min, Cs-doped AgBiI_4 thin films were obtained, and their morphology was reported to gradually improve with the addition of Cs^+ by suppressing the number of pinholes. The best result was achieved at a Cs content of 5 at.% with respect to Ag (Figure 12a,b), which was also found to contain BiI_3 and Ag_2BiI_5 impurities on the film

surface. The introduction of an excessive amount of cesium of 10 at.% resulted in the formation of films with pinholes again and the emergence of a $\text{Cs}_3\text{Bi}_2\text{I}_9$ admixture. Incorporation of other alkali metal iodides (LiI, KI, and RbI) into AgI/BiI_3 solutions was investigated by Wang et al.^[80] and was found to improve the crystallinity and morphology of Ag_2BiI_5 films. Finally, another coinage metal Cu^+ was also reported to favorably affect the crystallinity, morphology, and optoelectronic properties of Ag_2BiI_5 by improving the intrinsic light absorption and overall stability of the films.^[81]

3.3.2. Mixed Trivalent Cations

As discussed above, the mixed B-site compositions of silver pnictohalides examined thus far are mostly based on bismuth-antimony combinations. Iyoda et al. prepared mixed silver bismuth/antimony iodide compositions as films with a rough surface containing grains of various shapes and sizes.^[83] The synthesis included spin-coating a AgI , BiI_3 , and SbI_3 precursor solution with a target stoichiometry corresponding to $\text{Ag}_2[\text{Bi}+\text{Sb}]\text{I}_5$, treating the resulting films with toluene and annealing at 100 °C for 5 min. The introduction of antimony improved the film morphology considerably with a smooth surface and suitable coverage; however, other small particles were also formed (Figure 12c,d).

Complete replacement of Bi^{3+} with Sb^{3+} in AgBi_2I_7 synthesized by Zhu et al. to form AgSb_2I_7 improved the grain size in the films, although it resulted in the formation of pinholes.^[62,78,83] For the mixed bismuth-antimony compositions, the higher bismuth content films $\text{Ag}[\text{Bi}_{1.5}\text{Sb}_{0.5}]\text{I}_7$ had smaller crystals with many pinholes. In contrast, for the higher antimony content $\text{Ag}[\text{Bi}_{0.5}\text{Sb}_{1.5}]\text{I}_7$ films, small and large grains with very few pinholes were observed.^[63]

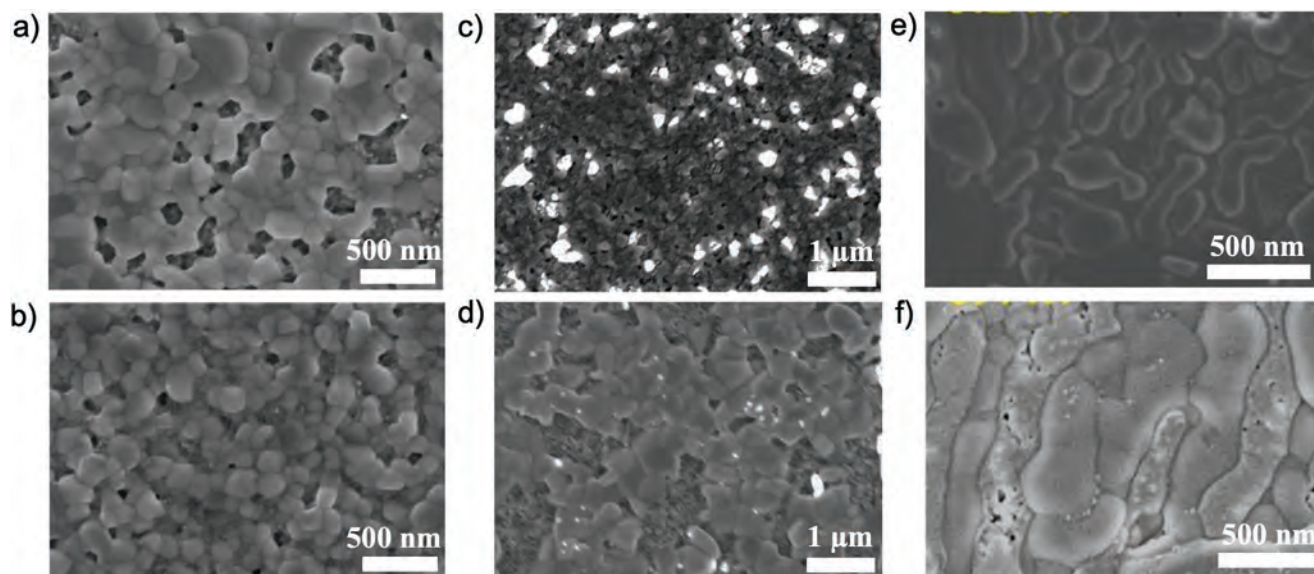


Figure 12. SEM images of Cs-incorporated AgBiI_4 at Cs concentrations of a) 0% and b) 10%. Reproduced with permission.^[76] Copyright 2020, American Chemical Society. SEM images of the spin-coated films of c) Ag_2BiI_5 , and d) $\text{Ag}_2[\text{Bi}+\text{Sb}]\text{I}_5$. Reproduced with permission.^[83] Copyright 2020, American Chemical Society. SEM images of the sulfur-modified Ag_3BiI_6 prepared at various precursor concentrations: e) 0.2 M, f) 0.4 M. Reproduced with permission.^[42] Copyright 2018, John Wiley and Sons.

3.3.3. Mixed X-Site Anions

Solution processes have primarily been employed to achieve partial anion substitution in silver bismuth iodide films.^[42,84] Similar to solution-processed pure silver bismuth iodides, all the precursor salts are dissolved in commonly used solvents, such as DMSO or DMF, spin-coated and then annealed to form the requisite film. In the case of partial replacement of iodine by sulfur to form $\text{Ag}_3\text{Bi}[\text{I}_{6-2x}\text{S}_x]$ silver bismuth sulfoiodide films, precursor salts silver(I) iodide, bismuth(III) iodide, and bismuth(III) tris(4-methylbenzodithioate) $[\text{Bi}(\text{S}_2\text{CAR})_3]$, which was the source of both Bi and S, were dissolved in stoichiometric ratios in a DMSO:DMF (3:1 vol) mixture with 12 vol.% HI added for improved solubility. The solution was then spin-coated and annealed at 130 °C for 15 min to form the required silver iodobismuthate.^[42] Argon gas was blown while spin-coated to accelerate solvent evaporation and promote oversaturation of the solution, thereby promoting crystallization. The solution-processed sulfur-modified $\text{Ag}_3\text{Bi}[\text{I}_{6-2x}\text{S}_x]$ films (Figure 12e,f) displayed complete coverage of the underlying mesoporous TiO_2 layer with oblong grains with an average size of 200 nm.^[42] Additionally, small particles (< 25 nm) were formed as impurities and were attributed to unreacted AgI based on the XRD data. While the sulfur-modified films were not smooth owing to the underlying uneven TiO_2 layer, no morphological change was induced by the partial replacement of I^- by S^{2-} of up to $x = 4$ at%. As the sulfide concentration was further increased, large grains (≈ 80 nm) were observed, associated with products from the decomposition of bismuth(III) tris(4-methylbenzodithioate).

Partial replacement of iodine with bromine to form $\text{AgBi}_2[\text{I}_{1-x}\text{Br}_x]_7$ films was achieved by dissolving BiBr_3 , AgI, and BiI_3 in hot DMSO, spin-coating and annealing at 90 °C for 5 min and at 150 °C for 15 min. An increase in the grain size of the films from 150 to 300 nm was observed as bromide ions were introduced, albeit larger grains were accompanied by more pinholes.^[84] It was proposed that the presence of bromide ions could suppress the reaction rate, leading to larger grains. However, at 40 at.% and higher bromide concentrations, the film morphology worsened, and the shape of the grains changed from cubic grains to nanoplates. This was attributed to phase segregation induced by structural decomposition.

Solution-based methods were mainly adopted for anionic or cationic substitution in silver pnictohalides, as they provide better control over the concentration. However, there are no significant reports on cationic or anionic substitution strategies for copper pnictohalides, probably due to the insuitability of cationic or anionic salts in the solvent systems employed. Considering the relevance of employing mixed anions or cations for tuning optoelectronic properties (discussed in Section 4), facile synthetic strategies that better control the degree of ionic replacement are necessary.

4. Electronic and Optoelectronic Properties

4.1. $\text{Ag}_x\text{B}_y\text{I}_{x+3y}$ ($\text{B} = \text{Bi}^{3+}$ or Sb^{3+})

To assess the optoelectronic potential of Ag-Bi-I compounds, much attention has been devoted to their absorption, bandgap,

energy levels, and charge transport properties. To investigate the bandgap of Ag-Bi-I thin films, researchers have relied on their optical absorption spectra and density functional theory (DFT) calculations. Compared to bismuth-based hybrid perovskite-inspired materials such as double perovskites and A_3BiX_9 compounds (where A is a monovalent cation such as $\text{Cs}^+/\text{Rb}^+/\text{CH}_3\text{NH}_3^+$ and X^- is a halide anion such as $\text{I}^-/\text{Br}^-/\text{Cl}^-$), which are limited by their wide indirect bandgaps ($E_g > 2.0$ eV),^[30,34,36,125–127] Ag-Bi-I materials have a considerably smaller bandgap in the range of 1.55–1.82 eV (indirect) and 1.6–1.93 eV (direct),^[38,39,42,79,90] as determined from the Tauc analysis of their UV–vis absorption spectra, which is more favorable for photovoltaic applications. The wide range in the bandgap of silver bismuth iodides arises from different compositions and synthesis conditions. Furthermore, Ag-Bi-I ternary systems, in general, irrespective of their composition, are reported to have an absorption coefficient in the range of 10^5 – 10^6 cm^{-1} , which is advantageous for realizing photovoltaic devices with submicrometer absorber thickness values.^[54]

The silver bismuth iodides have a valence band edge (E_{VB}) in the range of -5.51 to -6.4 eV (hereinafter, with respect to the vacuum level), while the conduction band edge (E_{CB}) is within the range -3.64 to -4.33 eV.^[41,52,53,92] The wide distribution of E_{VB} and E_{CB} values results from different synthesis conditions and techniques. Pai et al. reported the bandgap of several silver bismuth iodide-based compositions (AgBiI_4 , Ag_2BiI_5 , Ag_3BiI_6 , and AgBi_2I_7) synthesized using the same solution process and conditions, and a clear relationship between E_{VB} and E_{CB} on one side and silver bismuth iodide composition on the other side was observed.^[42] For instance, the E_{VB} of AgBiI_4 was -5.68 eV, which shifted upward to -5.64 eV for Ag_2BiI_5 and to -5.51 eV for Ag_3BiI_6 . On the other hand, for the bismuth-rich compound AgBi_2I_7 , there was a downward shift of E_{VB} to -5.80 eV compared to AgBiI_4 .^[42] A similar observation could be drawn for the conduction band edge, as the E_{CB} moved upward from -3.84 eV for AgBiI_4 to -3.75 eV for Ag_2BiI_5 and -3.64 eV for Ag_3BiI_6 and downward to -3.92 eV for AgBi_2I_7 .^[42] Thus, it can be concluded that increasing the silver content results in an upshift of the valence and conduction band edges, while the opposite occurs when the bismuth content is increased.

The electronic structure of Ag-Bi-I compounds has been investigated with first-principles methods based on DFT. Both Xiao et al. and later Sansom et al. performed band structure calculations for models of AgBiI_4 using the semilocal Perdew–Burke–Ernzerhof (PBE) method for treating the effects of exchange and correlation.^[47,54] As mentioned in Section 2.1, the AgBiI_4 structure involves layers of cations and vacancies. The disorder of site occupancy results in numerous possible structures within the minimum iodine sublattice unit cell.^[43]

The calculated band gaps and other quantitative features of Ag-Bi-I depend on the structure being calculated and on the specific method used in the calculations. A bandgap of 1.68 eV was calculated for AgBiI_4 by Xiao et al. using the PBE generalized gradient approximation (GGA).^[47] Wu et al. and Zhu et al. calculated band gaps of AgBi_2I_7 models using similar PBE methods and found slightly lower E_g of 1.4–1.6 eV.^[63,84] For group IB group VA composition materials, exact exchange and spin-orbit effects are significant, but the two effects almost cancel each other for the Ag-Bi-I systems.

Koedtrud et al. studied Ag-Bi-I ternary systems with rhombohedral (Ag_3BiI_6 , Ag_2BiI_5) and cubic (AgBiI_4 , AgBi_2I_7) phases. They reported direct bandgaps of ≈ 1.5 eV and ≈ 1.7 eV for the rhombohedral and cubic phases, respectively, and an indirect bandgap of ≈ 1.2 eV for the cubic phases.^[52] The valence band edges of the rhombohedral and cubic phases were -6.12 to -6.13 eV and -6.36 to -6.41 eV, respectively. They suggested that the difference in bandgap and valence band edge of silver iodobismuthates are not affected by composition but rather originate from the crystal structure of the rhombohedral or cubic phases. Since the valence bands of the Ag-Bi-I system are mainly dominated by Ag(4d) and I(5p) states, the shallow valence band edge in the rhombohedral structure was attributed to Ag(3b)-I bonds. At the same time, the small indirect bandgap observed in the cubic phase was assigned to the deficiency at the 16c edge-sharing octahedral site.

Sansom et al. calculated the hole and electron effective masses of AgBiI_4 for both defect-spinel and CdCl_2 -type models by fitting the band structure along with high symmetry directions Γ -L and Γ -Z (Figure 13).^[54] The authors reported that the valence band maximum is primarily a mixture of Ag(4d) and I(5p) states, whereas the conduction edge states are primarily a mixture of Bi(6p) and I(5p) states (Figure 13b,d). For the defect-spinel-type model, no significant difference between the hole effective masses of $1.0 m_e$ and $0.9 m_e$ and electron effective masses of $0.6 m_e$ and $0.8 m_e$ along the Γ -Z and Γ -L directions was found. In contrast, for the CdCl_2 -type model, the hole effective mass of $1.3 m_e$ and electron effective mass of $1.8 m_e$ were much higher in the Γ -Z direction than in the Γ -L direction, where the hole and electron effective mass was only $0.4 m_e$. Higher hole and electron effective masses along the Γ -Z direction for the CdCl_2 -type model are expected since the Γ -Z direction resembles transport normal to the Ag^+ and Bi^{3+} filled planes in the structure. They further reported the resistivity of AgBiI_4 at room temperature to be $1\text{M}\Omega\text{ cm}$, which was lower than that of MAPbI_3 ($38\text{ M}\Omega\text{ cm}$).^[128,129]

Furthermore, an experimental defect spectroscopy study revealed the presence of defect levels within the bandgap of AgBiI_4 , with average activation energies of 0.33 and 0.25 eV.^[130] However, the capture cross-sections of these defect levels were found to be in the 10^{-19} cm^2 range, which would therefore reduce their impact on the photovoltaic performance.^[130]

Microwave-based measurements (TRMC) have shown that silver iodobismuthates with rhombohedral structures have a higher conductivity than those with defect spinel structures, as reported by Iyoda et al.^[83] This was confirmed by Koedtrud et al., who found the electrical conductivity of the rhombohedral phase (Ag_2BiI_5) to be higher than that of the cubic phase (AgBi_2I_7), which was attributed to the lower activation energy for charge transport in the rhombohedral phase (10.89 kJ mol^{-1}) compared to that of the cubic phase (25.77 kJ mol^{-1}).^[52]

Processing conditions have a considerable effect on the charge transport characteristics of silver iodobismuthates. Pecunia et al. reported the Hall mobility of antisolvent-processed Ag_2BiI_5 thin films to be on average $1.6\text{ cm}^2\text{ V}^{-1}\text{ s}^{-1}$, i.e., three times higher than that of hot-coated films ($0.5\text{ cm}^2\text{ V}^{-1}\text{ s}^{-1}$).^[92] Ghosh et al. measured the Hall mobilities of AgBiI_4 and Ag_2BiI_5 thin films synthesized via dynamic hot casting and reported a higher mobility of $2.3 \pm 0.3\text{ cm}^2\text{ V}^{-1}\text{ s}^{-1}$ for Ag_2BiI_5 thin films compared to $1.7 \pm 0.3\text{ cm}^2\text{ V}^{-1}\text{ s}^{-1}$ for AgBiI_4 thin films. Both AgBiI_4 and Ag_2BiI_5 thin films had appreciable carrier densities of *ca* 4.2×10^{14} and $3.9 \times 10^{14}\text{ cm}^{-3}$, respectively.^[88]

Ghosh et al. also reported the presence of strong photo-bleaching in AgBiI_4 and Ag_2BiI_5 films from transient absorption spectra (Figure 14a), which was attributed to a change in the excitonic absorption due to the relaxed photoexcited carrier in the indirect band edge.^[88] Furthermore, they estimated the exciton binding energies of AgBiI_4 and Ag_2BiI_5 films to be 260 and 150 meV, respectively. However, the excitonic properties of silver iodobismuthates have not been studied in detail to date. The carrier lifetimes of AgBiI_4 and Ag_2BiI_5 were reported to be $\tau_1 \approx 7\text{ ns}$ and $\tau_1 \approx 12\text{ ns}$ (fast component) and $\tau_2 \approx 23\text{ ns}$ and $\tau_2 \approx 83\text{ ns}$ (slow

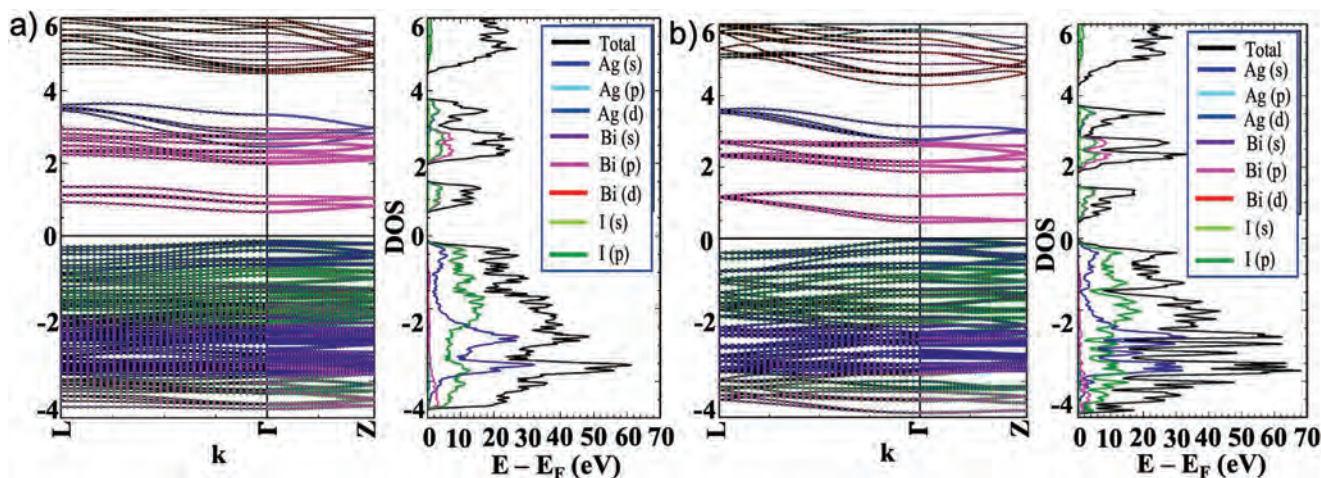


Figure 13. a) Calculated band structure of AgBiI_4 in its cubic structure and b) corresponding density of states with projections onto atomic orbitals at each atomic site. c) Calculated band structure of AgBiI_4 in its rhombohedral structure and d) corresponding density of states with projections onto atomic orbitals at each atomic site. Reproduced under the terms of the Creative Commons Attribution 4.0 International license.^[54] Copyright 2017, American Chemical Society.

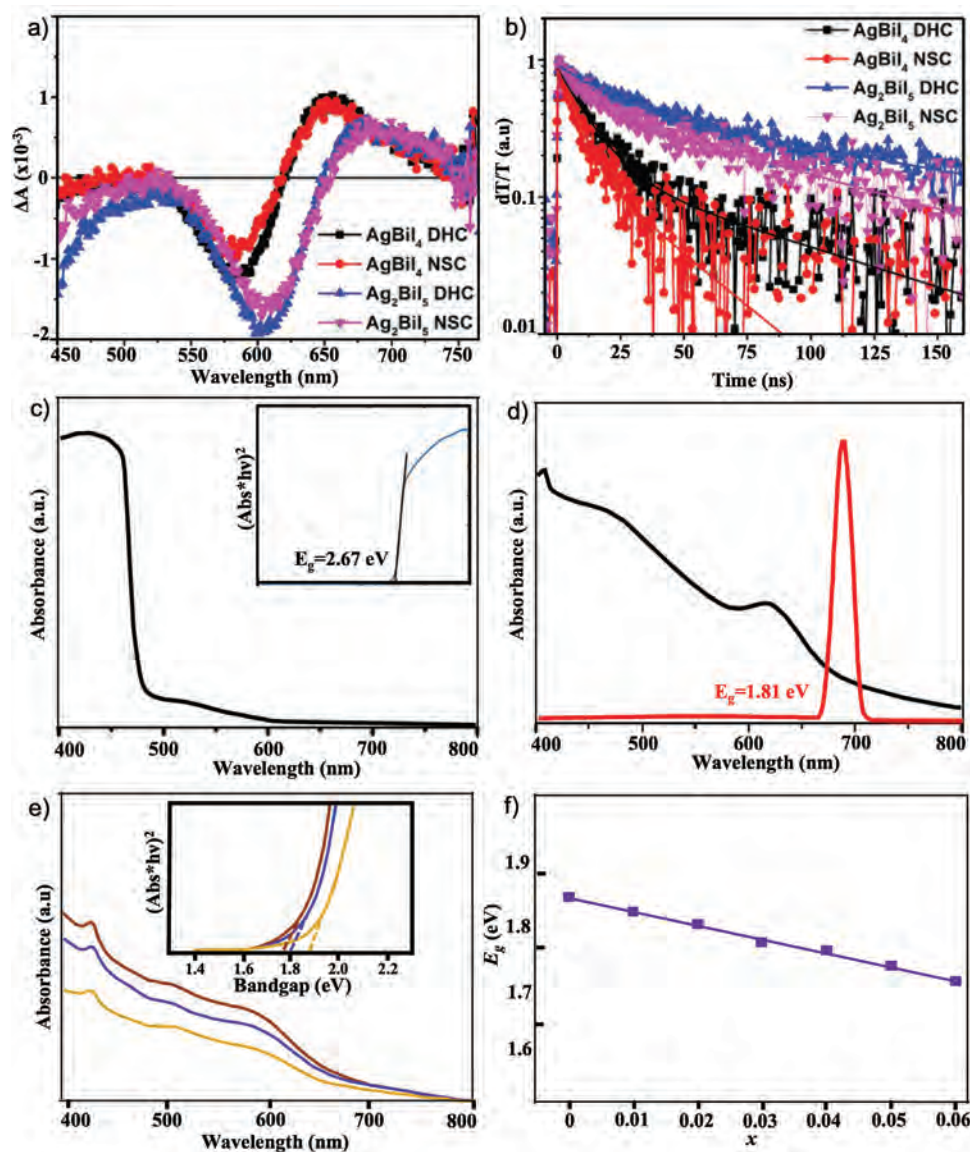


Figure 14. a) Transient absorption spectra (at 1 ns) and b) photobleaching decay dynamics (at ≈ 590 or 605 nm) of various silver bismuth iodides. Reproduced with permission.^[88] Copyright 2018, John Wiley and Sons. UV-vis spectra of CuBiI_4 synthesized by c) solution process (inset showing Tauc plot). Reproduced with permission.^[66] Copyright 2018, John Wiley and Sons. d) Direct metal surface reaction method (DMSER) (PL spectra shown in red). Reproduced with permission.^[101] Copyright 2018, Springer Nature. e) UV-vis spectra and Tauc plots (inset) of $\text{Ag}_3\text{Bi}[_{1-2x}\text{S}_x]$ coated onto $m\text{-TiO}_2/\text{TiO}_2/\text{FTO}$ for $x = 0$ (orange), 0.01 (purple), 0.02 (green), 0.03 (blue), 0.04 (brown), 0.05 (red), and 0.06 (magenta); f) dependence of the bandgap of $\text{Ag}_3\text{Bi}[_{1-2x}\text{S}_x]$ thin films on the level of anionic sulfide substitution. Reproduced with permission.^[42] Copyright 2018, John Wiley and Sons.

component).^[88] The carrier lifetimes associated with the slower component of the absorption transients were further increased to $\tau_2 \approx 75$ ns and $\tau_2 \approx 133$ ns by employing a dynamic hot-casting approach (Figure 14b).^[88] Lu et al. derived a maximum carrier lifetime of 5.8 ns from transient photoluminescence (TRPL) measurements on AgBiI_4 films. Additionally, they found that the TRPL lifetimes of such films deposited on poly[bis(4-phenyl) (2,4,6-trimethylphenyl)amine] (PTAA) and poly(3-hexylthiophene-2,5-diyl) (P3HT) were reduced to 3.8 and 4.7 ns, respectively, implying more efficient charge extraction by PTAA.^[89] $\text{AgBi}_3\text{I}_{10}$ was found to deliver photoluminescence transients with a fast component with a lifetime $\tau_1 \approx 3.6$ ns and a slow component with a lifetime $\tau_2 \approx 34$ ns.^[95]

4.2. $\text{Cu}_x\text{B}_y\text{I}_{x+3y}$ ($\text{B} = \text{Bi}^{3+}$ or Sb^{3+})

CuBiI_4 was reported to have a direct bandgap of 2.67 eV by Hu et al. (Figure 14c),^[66] while Zhang et al. found the optical bandgap of CuBiI_4 to be 1.81 eV (Figure 14d).^[101] This conspicuous difference in the optical bandgap was attributed to the different synthesis conditions. In the first case, a solution process was adopted, while in the latter case, a direct metal surface elemental reaction method (DMSER) was adopted. It appears that the conventional solution process is not sufficient to get the best out of this compound in terms of its usage as photoactive material. This is further supported by a report by Qu et al., who used mixed powders of the elemental constituents of the

compound before preparing the solutions and film deposition and reported an optical bandgap of 1.84 eV.^[102] Nonetheless, different synthesis conditions might not be the sole reason for such a difference in the bandgap, and thus, further studies are necessary to unambiguously determine the optical properties of CuBiI₄. The Fermi level of CuBiI₄ was reported to be closer to the conduction band, indicating *n*-type behavior, which is also evident from the transient photovoltage measurements.^[101]

The significant difference in the reported bandgaps of the CuBiI₄ films is also reflected in the published energy levels. Solution-processed CuBiI₄ films were found to have E_{VB} and E_{CB} at -5.68 and -3.01 eV, respectively,^[66] while CuBiI₄ films prepared through DMSER, which is a vapor-assisted process, were reported to exhibit downshifted E_{VB} and E_{CB} of -6.09 eV and -4.28 eV, respectively.^[101]

The effect of the synthesis method could also be observed in the carrier concentrations of the films: vapor-assisted (DMSER) CuBiI₄ films were found to have carrier concentrations two orders of magnitude higher than those of the solution-processed films. Additionally, the film resistance was three orders of magnitude higher for the solution-processed layers.^[101,102]

4.3. Partial Cation/Anion Substitution in Silver Bismuth Iodides

Pai et al. observed that partial replacement of iodide anion by sulfide led to significant improvements in the optoelectronic properties of thin films of silver iodobismuthates.^[42] The sulfur-modified films (AgBi[I_{4-2x}S_x], Ag₂Bi[I_{5-2x}S_x], and Ag₃Bi[I_{6-2x}S_x]) decreased their direct bandgaps from 1.89 to 1.73 eV as the sulfur content was increased from $x = 0$ to 0.06 (Figure 14e). The UV-vis spectra of all sulfur-containing films exhibited a weak peak at 415–425 nm, associated with AgI impurity, and a more intense peak at 495–505 nm for the bismuth-rich film AgBi₂[I_{7-2x}S_x], attributed to the BiI₃ octahedral component. The bandgap was revealed to have a linear relationship with the x value (Figure 14f), suggesting that for $x = 0.15$, this material system could achieve a bandgap of 1.6 eV, which would be ideal for photovoltaic applications. However, this could not be confirmed experimentally due to the solubility issue of the sulfur source bismuth(III) benzodithioate. Similarly, the valence band edge showed a linear upshift for all sulfur-modified films as the S content increased from 0 to 0.06, which is beneficial for charge separation and transfer.

In the case of anionic substitution of iodide ions with bromide ions in AgBi₂[I_{1-x}Br_x], an increase in bandgap from 1.78 to 2.1 eV (direct) and 1.59 to 1.95 eV (indirect) for $x = 0\%$ to 60% was observed.^[84] Investigation of the electronic structure of these materials revealed that partial bromide substitution affected both the valence and conduction band edges, leading to a change in the bandgap.

In regard to the partial substitution of bismuth with antimony, Ag[Bi_{2-x}Sb_x]I₇ displayed an increase in bandgap from 1.79 to 2.23 eV (direct) and 1.61 to 1.98 eV (indirect) as x increased from 0 to 2.^[63] Zhu et al. further calculated the near edge absorptivity ratio (NEAR) from Tauc plots to quantify the magnitude of the Urbach tail effect. The NEAR is calculated

using the formula $\left(\sqrt{\frac{\alpha(E_g)}{\alpha(1.02E_g)}} \right)$, where $\alpha(E_g)$ is the value at the

bandgap position and $\alpha(1.02E_g)$ is arbitrarily chosen to be 2% higher energy than the bandgap. Ideally, NEAR should be zero for a light absorber without any defects. They observed that the NEAR value was highest for solution-processed AgBiI₇, while the mixed bismuth–antimony halides had lower NEAR values, suggesting fewer sub-bandgap states.

Finally, the partial substitution of Ag⁺ with Cs⁺ in [Cs_xAg_{1-x}]BiI₄ resulted in essentially no change of the indirect bandgap (from 1.93 to 1.95 eV) as x was increased from 0 to 0.10.^[76] At the same time, a blueshift in the absorption edge for Cs content at $x = 0.10$ was observed, which was proposed to be due to the impurity phase of Cs₃Bi₂I₉.

5. Applications

5.1. Outdoor Solar Photovoltaics

Silver/copper pnictohalides have been intensively investigated as absorbers for photovoltaics, primarily due to the bandgap values of many of their embodiments approaching the optimum for single-junction or tandem photovoltaics (1.63–1.97 eV),^[36,38,39,76] in addition to their high absorption coefficients, solution processability, and high stability in ambient conditions. Investigating the photovoltaic properties of these ternary systems involved the fabrication of single-junction thin-film devices with active layer thicknesses in the range of 100–400 nm. To date, most of the research on these materials has focused on photovoltaic devices with a regular mesoporous device architecture (*n-i-p*), wherein the film is deposited on to a mesoporous TiO₂ layer. One of the primary reasons for using such device architecture is that a significant portion of the photoactive layer is embedded within the mesoporous electron transport layer, thereby shortening the distance that electrons must travel before being collected, i.e., enhancing the charge collection efficiency and suppressing recombination. Nonetheless, an additional mesoporous layer further complicates the device fabrication process and is not compatible with flexible substrates, as its fabrication requires high temperatures (≈ 500 °C).^[131] Hence, there have been few attempts to fabricate silver/copper pnictohalide-based solar cells using a regular (*n-i-p*) or inverted (*p-i-n*) structure with the active layer deposited on to a compact charge transport layer.^[76,79,90,92,93] Unfortunately, these devices displayed low efficiencies and suffered from severe hysteresis. At present, the mesoporous device architecture has delivered power conversion efficiencies under 1 sun AM1.5G simulated irradiation approaching 6% with sulfur-modified silver iodobismuthates,^[42] making this family of silver/copper pnictohalides the most promising for photovoltaic applications among all compositions explored to date.

To capture the general trends in composition versus photovoltaic performance of single-junction silver/copper pnictohalide solar cells, we plot in **Figure 15** their power conversion efficiencies (PCE) reported thus far, along with the corresponding open-circuit voltage (V_{oc}), short-circuit current density (J_{sc}), and fill factor (FF) values (Figure 15a,b). This figure reveals that compositions of 1:2, 2:1, 1:1, and 3:1 are the most studied group IB group VA compositions for photovoltaic applications to date. In the following, we discuss the progress

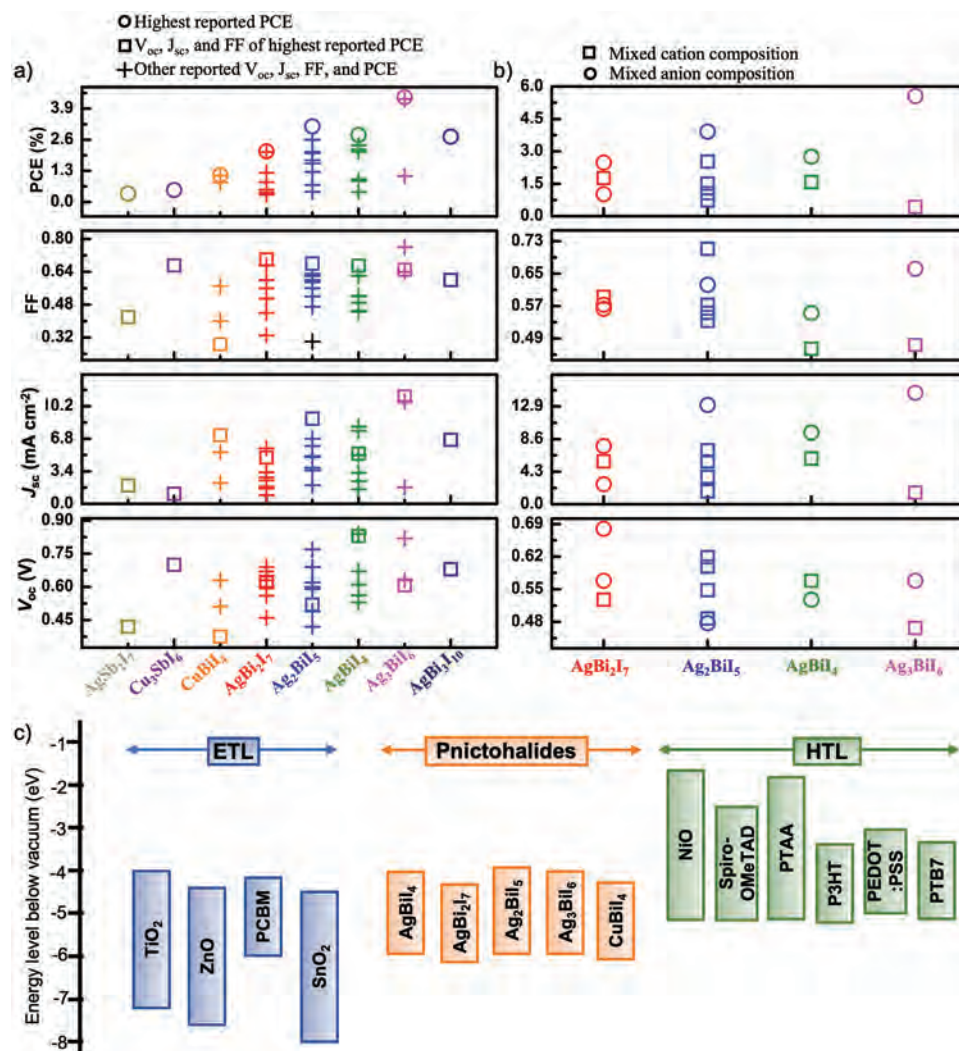


Figure 15. Photovoltaic parameters of a) pure and b) mixed cation/anion silver/copper pnictohalides. c) Energy level diagram of various ETLs, HTLs, and silver/copper pnictohalides.

in the solar cell performance of the various silver/copper pnictohalides and highlight the challenges faced.

5.1.1. $Ag_xB_yI_{x+3y}$ ($B = Bi^{3+}$ or Sb^{3+})

From Figure 15a,b, we can see that among all silver bismuth iodides, Ag_3BiI_6 -based solar cells have delivered the best performance thus far, achieving a PCE and J_{sc} of 5.6% and 15 mA cm⁻², respectively, for sulfur-modified Ag_3BiI_6 and a PCE and J_{sc} of 4.4% and 11 mA cm⁻², respectively, for pure Ag_3BiI_6 .^[42] In the case of pure- Ag_3BiI_6 -based solar cells with a device structure FTO|c-TiO₂|m-TiO₂| Ag_3BiI_6 |PTAA|Au (FTO – fluorine-doped SnO₂; c-TiO₂ and m-TiO₂ – compact and mesoporous titania, respectively), the notable increase in J_{sc} and PCE compared to previously published values^[43] was attributed to the improvement of the film quality provided by the gas-assisted spin-coating. Further significant improvements provided by the sulfide modification were explained by the enhanced absorption coefficient as well as the decrease in the bandgap

from 1.87 to 1.76 eV, primarily through the adjustment of the valence band edge to a value more favorably aligned with the hole transport material. While efficient light harvesting ensures improved charge carrier density, better band alignment enables more effective charge extraction. However, in both cases, relatively low V_{oc} values (≈ 0.57 and 0.61 V for sulfur-modified and pure Ag_3BiI_6 , respectively) were observed, which were primarily attributed to the presence of impurity particles on the film surface. Turkevych et al. also reported Ag_3BiI_6 -based solar cells with comparatively high performance, featuring a PCE of $\approx 4.3\%$, J_{sc} of ≈ 11 mA cm⁻², FF of $\approx 64\%$ and V_{oc} of ≈ 0.6 V. While the high PCE and J_{sc} were attributed to the intrinsic light-harvesting capability of the materials, the low V_{oc} and FF were rationalized in terms of the short carrier lifetime of 1 ns that could induce rapid recombination of the carriers in the Ag_3BiI_6 devices.

Pai et al. studied the effect of hole transport material (HTM) on the photovoltaic performance of Ag_3BiI_6 . They found that commonly used organic HTMs such as 2,2',7,7'-tetrakis-(*N,N*-di-4-methoxyphenylamino)-9,9'-spirobifluorene

(spiro-OMeTAD) and P3HT as well as inorganic HTMs such as cuprous thiocyanate (CuSCN) and cuprous iodide (CuI) provided low performance due to the use of solvents such as acetonitrile and chlorobenzene, as well as LiTFSI and *tert*-butylpyridine additives, all of which were reported to degrade the silver-bismuth iodide layer, leading to reduced J_{sc} and PCE. PTAA was found to be the most suitable HTM considering favorable energy matching and efficient charge transfer (Figure 15c).^[88] This is consistent with the findings from studies on related silver bismuth iodide solar cells, which revealed that the dopants commonly used in combination with spiro-OMeTAD damage the underlying active layers; in contrast, if spiro-OMeTAD is deposited without such dopants, the resultant solar cells deliver adequate photoconversion efficiency.^[92,132]

Apart from Ag_3BiI_6 , another silver-rich compound, Ag_2BiI_5 , has also been incorporated into photovoltaic devices. Zhu et al. fabricated the first Ag_2BiI_5 -based solar cell and compared its performance to those based on $AgBi_2I_7$. The reported Ag_2BiI_5 device delivered a PCE of $\approx 2.1\%$ and J_{sc} of $\approx 6.8 \text{ mA cm}^{-2}$, almost 5 times higher than that found for $AgBi_2I_7$.^[50] The fill factor for the Ag-rich material was also higher than that for the Bi-rich composition (*ca* 63% vs 56%). While the authors did not explain in detail the enhanced performance of the Ag_2BiI_5 -based solar cells, they suggested that the high efficiency could be attributed to effective electron transfer to the underlying TiO_2 layer. Although the PCE and J_{sc} were higher for the Ag_2BiI_5 -based solar cells, the V_{oc} values were relatively low (0.5 V) and similar to those recorded for the $AgBi_2I_7$ devices. The low V_{oc} could be associated with incomplete coverage of the underlying TiO_2 layer and the presence of foreign particles on the film surface.

Ghosh et al. improved the device performance with the Ag_2BiI_5 active layer using a dynamic hot-casting (DHC) method, which resulted in a PCE of $\approx 2.6\%$, V_{oc} of $\approx 0.7 \text{ V}$, J_{sc} of $\approx 6 \text{ mA cm}^{-2}$, and FF of $\approx 62\%$.^[88] Compared to the standard spin-coating method (SSC) with antisolvent treatment that delivered a PCE of $\approx 1.6\%$, V_{oc} of $\approx 0.63 \text{ V}$, J_{sc} of $\approx 4.4 \text{ mA cm}^{-2}$, and FF of $\approx 62\%$, the films prepared with the DHC method displayed larger grains with negligible pinholes and higher absorption. Additionally, the carrier lifetime of the Ag_2BiI_5 thin film was enhanced for DHC-prepared films ($\approx 130 \text{ ns}$) compared to SSC-prepared films ($\approx 83 \text{ ns}$). The low J_{sc} of $\approx 6 \text{ mA cm}^{-2}$ compared to the integrated current density of $\approx 7.9 \text{ mA cm}^{-2}$ calculated from the incident-photon-to-current conversion efficiency (IPCE) spectra of the Ag_2BiI_5 thin film was attributed to the non-optimal thickness of the transport layers, which resulted in space-charge-limited photocurrent or imbalanced electron-hole mobilities. The highest efficiency of $\approx 3.2\%$ was reported for Ag_2BiI_5 using the gas-assisted spin coating technique where the films were dried in the presence of argon gas flow to accelerate nucleation.^[42] The photovoltaic device architecture FTO|c-TiO₂|m-TiO₂| Ag_2BiI_5 |PTAA|Au demonstrated an enhanced J_{sc} of $\approx 8.9 \text{ mA cm}^{-2}$, while a low V_{oc} of $\approx 0.52 \text{ V}$ was recorded. Introduction of sulfide by partially replacing the iodide ions from Ag_2BiI_5 resulted in the enhancement of J_{sc} to $\approx 13 \text{ mA cm}^{-2}$, leading to a PCE of $\approx 3.9\%$.^[42] However, V_{oc} decreased further to $\approx 0.48 \text{ V}$. The improvement in J_{sc} was attributed to enhanced light absorption due to the decrease in the bandgap to $\approx 1.77 \text{ eV}$. The low V_{oc} could be the result of additional recombination pathways introduced via sulfide incorporation.

Another composition that has attracted significant interest in photovoltaic studies is $AgBiI_4$. The first report on $AgBiI_4$ solar cells demonstrated a PCE of $\approx 2.1\%$ with a J_{sc} of $\approx 7.6 \text{ mA cm}^{-2}$, FF of $\approx 52\%$ and V_{oc} of $\approx 0.5 \text{ V}$.^[89] An optimized precursor solution concentration of 0.6 M provided a higher absorption and carrier lifetime (5.8 ns) in contrast to films deposited from 0.4 M (3.8 ns) and 0.8 M (3.6 ns) solutions. Ghosh et al. employed a dynamic hot-casting technique to improve the film morphology of $AgBiI_4$ thin films, leading to a significant enhancement in all photovoltaic parameters, viz. V_{oc} from 0.63 to *ca* 0.67 V, J_{sc} from *ca* 3.7 to 5.2 mA cm^{-2} , FF from *ca* 51 to 62%, and PCE from *ca* 1.2 to 2.2%.^[88]

Zhang et al. achieved the highest PCE of $\approx 2.8\%$ for $AgBiI_4$ -based solar cells with the planar device structure ITO|SnO₂| $AgBiI_4$ |PTAA|Au through additive engineering.^[79] They found that adding LiTFSI to the precursor solution resulted in a fully covered pinhole-free film morphology, which significantly improved the photoconversion efficiency and resulted in a V_{oc} of $\approx 0.83 \text{ V}$. The high V_{oc} was attributed to the superior quality of the film owing to the LiTFSI additive, which was suggested to mitigate the recombination sites. The relatively low J_{sc} of $\approx 5.1 \text{ mA cm}^{-2}$ reported in the same study was attributed to the low thickness of the absorber layer and matched satisfactorily with an integrated current density of $\approx 4.7 \text{ mA cm}^{-2}$. An increase in the film thickness resulted in a higher V_{oc} of $\approx 0.88 \text{ V}$ —the highest among all silver/copper copolymer compositions reported—but also induced a drop in J_{sc} to even lower values, which was suggested to be an effect of the limited carrier diffusion length in thicker absorber layers. As observed previously, sulfur modification of $AgBiI_4$ lowered the bandgap to $\approx 1.73 \text{ eV}$, leading to an enhanced J_{sc} of $\approx 9.5 \text{ mA cm}^{-2}$, although at the cost of low FF and V_{oc} , which were found to be *ca* 55% and 0.53 V, respectively; the resulting PCE was $\approx 2.8\%$.^[42]

$AgBi_2I_7$ has also been extensively studied for photovoltaic applications. The first reported solar cell based on $AgBi_2I_7$ as the photoactive layer had a device structure of FTO|c-TiO₂|m-TiO₂| $AgBi_2I_7$ |P3HT|Au. Such devices delivered a PCE of $\approx 1.2\%$ with a V_{oc} of $\approx 0.56 \text{ V}$, J_{sc} of $\approx 3.3 \text{ mA cm}^{-2}$, and FF of $\approx 67\%$.^[41] The authors opted for *n*-butylamine as a solvent instead of the commonly used DMSO or DMF to improve the solubility of AgI. Later, Kulkarni et al. improved the crystallinity of $AgBi_2I_7$ films by using hot DMSO as the solvent and demonstrated a PCE of $\approx 2.1\%$ with $V_{oc} \approx 0.62 \text{ V}$, $J_{sc} \approx 4.8 \text{ mA cm}^{-2}$, and FF $\approx 70\%$ using the device structure FTO|c-TiO₂|m-TiO₂| $AgBi_2I_7$ |P3HT|Au, which is the highest reported performance of solar cells based on unmodified $AgBi_2I_7$.^[57] The significant improvement in the device performance was attributed to the superior film morphology without pinholes and complete coverage of the underlying transport layer, along with the presence of trapped BiI₃, which was suggested to facilitate charge transport.

Sulfur-modified $AgBi_2I_7$ was also assessed as an absorber in solar cells using the device structure FTO|c-TiO₂|m-TiO₂| $AgBi_2I_7$ |PTAA|Au. This resulted in the highest J_{sc} of $\approx 7.7 \text{ mA cm}^{-2}$ and an enhanced PCE of $\approx 2.5\%$,^[42] but again low FF ($\approx 57\%$) and V_{oc} of $\approx 0.57 \text{ V}$, probably due to the presence of additional recombination centers emerging upon modification with sulfide. Other cationic or anionic substitutions in $AgBi_2I_7$, such as partial replacement of bismuth with

antimony or iodine with bromine, did not result in performance that matched the solar cells based on the parent, unsubstituted compounds reported in the literature. For instance, Wu et al. reported a PCE of $\approx 1.8\%$ and J_{sc} of $\approx 5.7 \text{ mA cm}^{-2}$ provided by $\text{Ag}[\text{Bi}_{0.5}\text{Sb}_{1.5}]\text{I}_7$, which were higher than those measured for the control AgBi_2I_7 -based devices investigated within the same study,^[63] but notably lower than the performance for the best AgBi_2I_7 -based solar cells reported by other groups. Nonetheless, in this particular case, improvement in the performance was attributed to improved energy level matching between the active layer and the electron transport layer owing to the shift of the VBM and CBM upon introduction of antimony.

Complete substitution of bismuth with antimony to form AgSb_2I_7 led to suppressed performance owing to the increased bandgap (2.2 eV) and formation of sub-bandgap states, as confirmed by the near edge absorptivity ratio. Consequently, except for sulfide modification, other ionic substitutions in silver bismuth iodides failed to match the highest photovoltaic performance of their respective parent compounds reported by others.^[78,82–84]

The bismuth-rich compound $\text{AgBi}_3\text{I}_{10}$ was used as a photovoltaic absorber within devices with an $\text{FTO}|\text{c-TiO}_2|\text{m-TiO}_2|\text{AgBi}_3\text{I}_{10}|\text{Al}_2\text{O}_3|\text{NiO}|\text{carbon structure}$.^[95] The superior film quality with large grains and no pinholes along with inorganic transport materials resulted in a PCE of $\approx 2.7\%$, J_{sc} of $\approx 6.7 \text{ mA cm}^{-2}$, FF of $\approx 60\%$, and V_{oc} of $\approx 0.68 \text{ V}$. However, the J - V characteristics of these devices recorded at various light intensities revealed that further enhancement in the device performance is challenging due to the presence of traps.

Investigations of silver-bismuth-iodide solar cells under various conditions, e.g., under illumination and subjected to heating and moisture, have been pursued to assess the device stability of these materials. Kim et al., who reported the first silver bismuth iodide solar cells, showed the AgBi_2I_7 -based solar cell to be stable for 10 days under ambient conditions.^[41] Kulkarni et al. later demonstrated improved stability for 75 days in air at a relative humidity of 50–60% for AgBi_2I_7 -based solar cells.^[57] The considerable improvement in stability was attributed to the use of dimethyl sulfoxide as a solvent instead of *n*-butylamine, which was also used by Kim et al.^[41] Additionally, Kulkarni et al. demonstrated the high thermal stability of their devices at 100 °C for 5 h. In general, silver bismuth iodides without encapsulation under ambient conditions, i.e., at 20–30 °C and relative humidity of 50–75%, display stability for at least a month. Furthermore, cation-substituted and anion-substituted silver bismuth iodides display extended stability for more than a month.^[42,63,76,78,83,84] In an inert N_2 atmosphere, silver bismuth iodides were found to be stable for at least 6 months.^[90] Silver-rich $\text{Ag}_3\text{BiI}_{10}$ showed essentially no change in XRD profiles when kept under ambient conditions (20 °C and 40% relative humidity) after 2 months.^[95]

Sansom et al. studied the stability of AgBiI_4 under illumination and heating. They reported that while this material retained its structure when subjected to elevated temperatures from 60 to 290 °C, XRD analysis revealed a small peak of Ag_2BiI_5 as an impurity appearing at $\approx 90 \text{ °C}$.^[54] In comparison, MAPbI_3 degrades at 85 °C, even in an inert atmosphere, and undergoes phase transition at lower temperatures (45–55 °C).

The photostability of AgBiI_4 when exposed to AM 1.5G illumination in air was also found to be better than that of MAPbI_3 , with the former retaining its crystal structure after 3 h of illumination. This contrasts the commencement of the decomposition of methylammonium lead iodide after only 1 h of testing and complete structural degradation after 3 h.^[54] Nonetheless, partial decomposition of AgBiI_4 to AgI after $\approx 2 \text{ h}$ was reported. Furthermore, the low activation energy (0.4 eV) of Ag^+ migration within AgBiI_4 , which is comparable to that for the I^- migration in MAPbI_3 (0.44 eV), suggests facile cation migration. Crovetto et al. suggested that the presence of these mobile silver ions could increase carrier selectivity at the silver iodobismuthate/ETL interface and thus enhance charge transfer.^[133] Finally, additives such as LiTFSI that have improved the initial device performance were reported to have adverse effects on the stability.^[79]

5.1.2. $\text{Cu}_x\text{Bi}_y\text{I}_{x+3y}$ ($B = \text{Bi}^{3+}$ or Sb^{3+})

The first publication on solution-processed CuBiI_4 thin films reported a bandgap of $\approx 2.7 \text{ eV}$ and used these materials to fabricate solar cells with the architecture $\text{ITO}|\text{c-TiO}_2|\text{m-TiO}_2|\text{CuBiI}_4|\text{Spiro-OMeTAD}|\text{Au}$, delivering a PCE of $\approx 0.8\%$ with J_{sc} of $\approx 2.2 \text{ mA cm}^{-2}$, V_{oc} of $\approx 0.6 \text{ V}$, and FF of $\approx 59\%$.^[66] Later, Zhang et al. reacted iodine vapors with Bi–Cu alloy to form CuBiI_4 thin films, resulting in a material with a bandgap of $\approx 1.8 \text{ eV}$.^[101] Such CuBiI_4 thin films, when employed in solar cells with a planar ETL-free $\text{ITO}|\text{CuBiI}_4|\text{Spiro-OMeTAD}|\text{Au}$ structure, delivered a PCE of $\approx 1.1\%$ with J_{sc} of $\approx 7.2 \text{ mA cm}^{-2}$, V_{oc} of $\approx 0.38 \text{ V}$, and a very low FF of $\approx 29\%$, which is nevertheless the best-reported performance for CuBiI_4 films thus far.^[66,101] Such low photovoltaic performance was primarily attributed to the presence of severe recombination pathways. We assume that an ETL-free device structure was preferred due to the specifics of the film fabrication process. Presumably, the photovoltaic performance of CuBiI_4 could be further improved through the use of a mesoporous ETL. Moreover, CuBiI_4 is a promising candidate for tandem solar cells due to its suitable bandgap (1.8 eV) and photoelectric properties comparable to those of lead-based perovskites.^[66,101,103] However, further modification of the synthesis process is required to improve the film morphology and its optoelectronic properties.

Cu_3SbI_6 , which has an indirect bandgap of $\approx 2.4 \text{ eV}$, has also been investigated as a photoactive material in solar cells. Planar Cu_3SbI_6 -based devices were reported with PEDOT:PSS and PCBM as the ETL and HTL, respectively, and demonstrated a J_{sc} of $\approx 1.1 \text{ mA cm}^{-2}$, V_{oc} of $\approx 0.7 \text{ V}$, fill factor of $\approx 70\%$, and a resulting PCE of $\approx 0.5\%$.^[40] It was further observed that the photovoltaic parameters improved as the thickness of the photoactive layer was increased from ≈ 90 to 140 nm, but declined as the thickness was increased further, which suggests a relatively short carrier diffusion length.

In regard to the stability of copper pnictohalides, CuBiI_4 thin films have demonstrated superior photostability for more than 40 days under ambient conditions without encapsulation.^[66] Similar stability was reported for Cu_3SbI_6 , although under an inert N_2 atmosphere.^[40]

5.1.3. Efficiency Losses

Given that the average bandgap of $\text{Ag}_x\text{Bi}_y\text{I}_{x+3y}$ compounds is approximately 1.8 eV, this class of materials has the potential to provide an efficiency of 27% at the radiative limit, with a V_{oc} of 1.5 V, J_{sc} of 20 mA cm^{-2} , and FF of 91%. While short-circuit current densities of 15 mA cm^{-2} have already been achieved,^[37] significant progress is still needed to attain high open-circuit voltages and fill-factors (Figure 15a,b). Photovoltaic performance losses within these solar cells are most likely caused by the presence of crystallographic/surface defects and insufficiently high carrier lifetimes and mobilities. Increased defect-state densities and misalignment of the band edges with the charge-transport layers may additionally hamper effective charge transfer. When coupled to active and charge transport layers with nonoptimal thicknesses, imbalanced electron-hole transport could take place. Insufficiently long photogenerated carrier diffusion lengths and lifetimes would promote their rapid recombination via defects deep into the bandgap. Therefore, the significant open-circuit voltage losses in $\text{Ag}_x\text{Bi}_y\text{I}_{x+3y}$ solar cells to date can be attributed to nonradiative recombination. Most likely, these undesired losses occur at the grain boundaries and interfaces due to defects and impurities, which highlights the need to develop phase-pure high-quality active layers. Low fill-factors, typically below 70%, can be explained by high series resistance and unsatisfactorily low shunt resistance due to internal charge transport limitations and imperfections in the photoactive layers, as well as nonoptimized interfaces with the electron and hole-transporting layers producing excessive charge-transfer barriers.

Building upon research efforts on other photovoltaic technologies, the application of passivation strategies along with the optimization of the active layer morphology and device architecture might mitigate the pernicious effects of short carrier lifetimes, as was achieved, for example, in $\text{Cu}_2\text{ZnSnSe}_4$ and Sb_2Se_3 solar cells.^[134–136] The elimination of defects by introducing additives and/or dopants is also likely to be an effective approach, as has been already demonstrated when LiTFSI and alkaline-earth metals were applied to silver pnictohalide solar cells to achieve significantly improved V_{oc} values.^[79,80,116] Similarly, partial cationic/anionic and HI-assisted modification strategies have been demonstrated to improve the short-circuit current density.^[42,53,92]

The low photovoltaic performances reported for copper pnictohalides highlight the importance of the bandgap of the active material for efficient light absorption. Indeed, the highest J_{sc} reported for Cu-based materials ($<3 \text{ mA cm}^{-2}$),^[101,102] which exhibit bandgaps in excess of 2 eV and downshifted conduction and valence band edges, are much lower than those achieved with silver pnictohalides (15 mA cm^{-2}).^[42,43]

One current challenge with silver/copper pnictohalide-based solar cells is that improvements in one parameter (e.g., J_{sc}) commonly come at the expense of another (e.g., V_{oc}), suggesting that future advances might emerge from combinations of the active layer and device modification strategies introduced to date and to be developed.

Finally, the lack of an in-depth understanding of the correlations between the composition/structure, optoelectronic properties, and photovoltaic performance for silver/copper

pnictohalides is a critical factor that limits the development of devices with improved performance.

5.2. Indoor Photovoltaics

In recent years, indoor photovoltaics (IPV) have garnered much attention for powering wireless sensor networks to enable the realization of the full potential of the Internet of Things (IoT).^[137–140] These sensors conventionally rely on batteries as a power source, which is problematic in terms of cost and environmental impact.^[141] In contrast, using IPVs as the power source of the sensors provides a sustainable pathway for the growth of the IoT. IPVs rely on artificial light sources such as white light-emitting diodes and fluorescent lamps present inside buildings. The light emitted by such lamps can be converted to electrical energy to power electronic devices with low power consumption. Unlike standard outdoor AM 1.5G solar light, which has a broad-spectrum width (300–2500 nm) and intensity of 100 mW cm^{-2} , indoor lighting emits photons in the visible region (400–700 nm) and with lower intensity, in the range of $50\text{--}300 \mu\text{W cm}^{-2}$ ($\approx 200\text{--}2000 \text{ lux}$),^[142] as depicted in Figure 16a. Due to the narrower spectrum of indoor lighting compared to outdoor solar light, the ideal bandgap for IPV photoabsorbers is $\approx 1.9 \text{ eV}$ (Figure 16b), which makes wide bandgap materials such as amorphous silicon, lead-halide perovskites, organic semiconductors, and dye-sensitized solar cells preferable to the low bandgap crystalline silicon (1.1 eV) that dominates the outdoor photovoltaic market.^[143,144]

For the first time, Peng et al.^[145] demonstrated IPV based on perovskite-inspired materials, relying on layered $\text{Cs}_3\text{Sb}_2(\text{Cl}_x\text{I}_{9-x})$ and BiOI. They achieved efficiencies between 4% and 5%, falling within the range of 4–9% pertinent to the commercially dominant amorphous silicon IPV. This study also reported the calculated efficiency limit of various perovskite-inspired materials using spectroscopic limited maximum efficiency (SLME), which considers the absorptance, thickness of the absorber, and nature of the bandgap (direct/indirect), thus providing a more realistic maximum efficiency. Crucially, their analysis showed that AgBiI_4 and Ag_2BiI_5 could achieve theoretical efficiencies between 50% and 60%, which is also the highest among all lead halide perovskites and lead-free perovskite-inspired materials. Following these encouraging indications, Turkevych et al. reported the first “rudorffite” (AgBiI_4)-based IPV cell with the device architecture $\text{FTO|c-TiO}_2|\text{AgBiI}_4|\text{Spiro-OMeTAD}|Au$ (Figure 16c).^[121] They coevaporated silver and bismuth to form a $\text{Ag}_{0.5}\text{Bi}_{0.5}$ bimetallic film, which was then exposed to iodine vapor to form AgBiI_4 films, which displayed a bandgap of 1.8 eV close to the optimal bandgap of 1.9 eV required for IPVs. Their device achieved an efficiency of $\approx 5.2\%$ and $\approx 4.8\%$ and power output of ≈ 1.8 and $\approx 0.81 \mu\text{W cm}^{-2}$ under 1000 lux and 500 lux, respectively (Figure 16d). While the efficiency of the AgBiI_4 -based IPV by Turkevych et al. is much lower than the ultimate potential of this material (as calculated by Peng et al.^[145]) and the output power is relatively low, they suggested that the “rudorffite” IPV in combination with an energy storage device could drive a low-power wireless transmitter to achieve reliable data transfer.

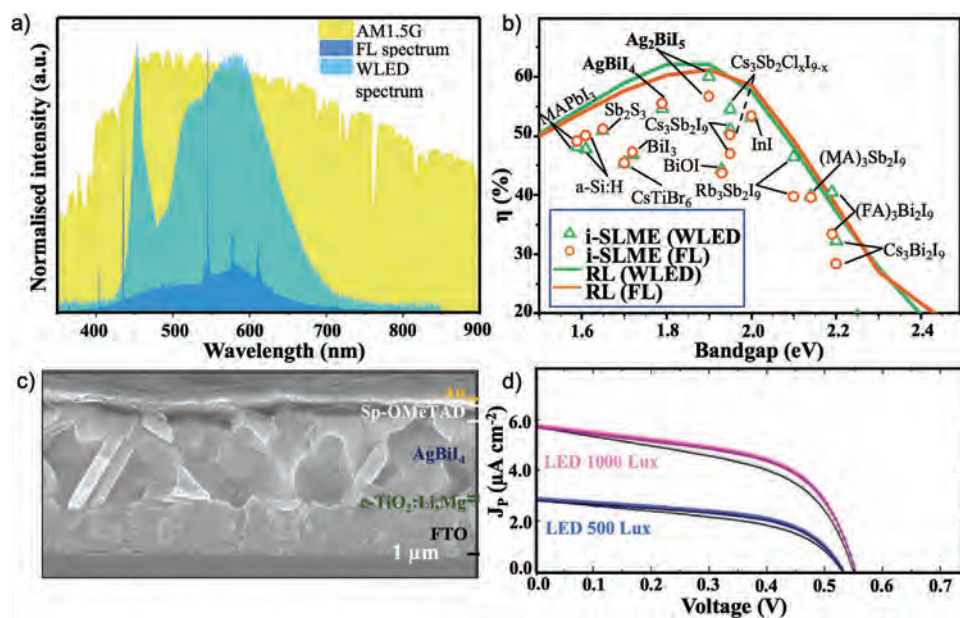


Figure 16. a) Comparison of spectral characteristics of the solar and indoor LED light with ranges of power consumption. b) Radiative limit and spectroscopically limited maximum efficiency (SLME) of the photovoltaic efficiencies of lead-free perovskite-inspired materials under AM 1.5G and indoor lighting conditions. Adapted under the terms of the Creative Commons Attribution 4.0 International license.^[145] Copyright 2020, Peng et al. c) Cross-section SEM image and d) J - V characteristics of the AgBiI_4 -based IPV cell showing forward (black) and reverse (red and blue) scans for 1000 and 500 lux illumination, respectively. Reproduced with permission.^[121] Copyright 2021, The Japan Society of Applied Physics.

Although silver pnictohalides have just entered the IPV arena and have ample scope to deliver higher efficiencies in light of their ultimate IPV potential, various challenges need to be addressed.^[144] First, various studies have shown the presence of defect-assisted traps in silver bismuth iodides that can lead to voltage loss, which is also evident from the AgBiI_4 -based IPV that manages a V_{oc} of ≈ 0.55 V. To prevent this voltage loss, the film morphology must be improved to achieve larger grains with no pinholes. Additionally, Turkevych et al. suggested that extremely thin absorber layers can enhance the charge collection probability and thus improve J_{sc} . Second, in addition to the absorber, the metal oxide electron transport layers, such as TiO_2 , SnO_2 , and ZnO , primarily used in outdoor photovoltaics contain traps filled by the UV component of the solar spectrum and high incident light intensity.^[146,147] However, in indoor lighting conditions with lower intensities and only operating in the visible region of the light spectrum, these trap sites might pose a severe challenge. Thus, further research is required to develop metal-oxide charge transport layers that will not require UV activation to fill up these traps, thereby not limiting the power conversion efficiency.

5.3. Photodetectors

Photodetectors are ubiquitous in modern electronic systems and play a significant role in emerging applications such as optical communication, medical imaging, wearable electronics, and the IoT.^[3,148–151] Low-cost organic and hybrid lead-halide perovskites have unique tunable optoelectronic properties that have stimulated further research in this domain.^[152–158] However, the toxicity and instability of lead-halide perovskites have

been a major bottleneck in their commercialization for various optoelectronic applications, prompting the search for lead-free perovskite-inspired materials for photodetection.^[125,159,160] Among the various perovskite-inspired materials, silver/copper pnictohalides are attractive for photodetector applications because they offer a 3D lattice configuration that can benefit charge transport. In addition, they have bandgaps between 1.6 and 2.8 eV, making them suitable for UV and visible light detection. Additionally, since silver bismuth iodides are blind to the NIR region of the light spectrum, the NIR filters can be avoided for visible-light detector applications, thus reducing the overall system cost and complexity while avoiding efficiency loss.^[92]

The efficacy of these materials for visible light detection was first demonstrated by Pecunia et al.^[92] using Ag_2BiI_5 . They studied the correlation between the film morphology and key photodetector parameters at an applied bias of 0 V (self-power mode). These compositions were prepared using three different methodologies, namely, hot-coating (HC), antisolvent processing (ASP), and hydroiodic acid additive (HIA), on mesoporous- TiO_2 -coated substrates. The cross-sectional image (Figure 17a-c) of the films revealed that a certain portion of them (≈ 250 nm) was embedded into a mesoporous layer of TiO_2 , irrespective of the processing method. The region above the transport layer was found to have a thickness of ≈ 5 nm in HIA samples, ≈ 30 nm for ASP samples, and ≈ 100 nm in the HC samples. The significance of the film distribution on the m- TiO_2 transport layer was evident from the photoconversion efficiency of the films; as such, the ASP and HC samples achieved an external quantum efficiency (EQE) of $\approx 10\%$ and below, while the HIA samples achieved a higher EQE of $\approx 27\%$ (Figure 17d). Apart from the EQE, the spectral responsivity (R_λ), another critical parameter in photodetectors, was found to cover

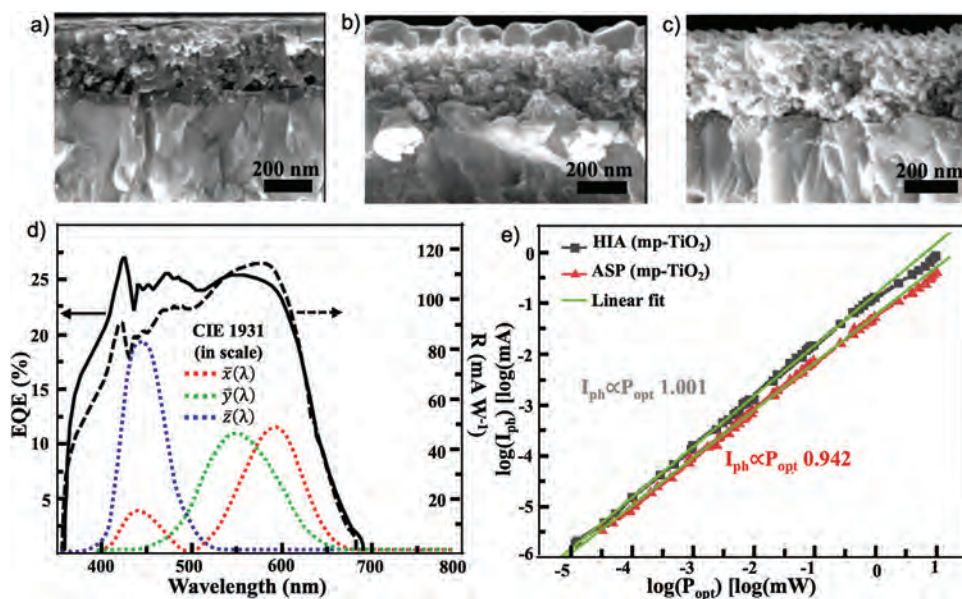


Figure 17. Cross-sectional SEM image of Ag_2BiI_5 films prepared by a) ASP, b) HC, and c) HIA methods; photodetector performance of Ag_2BiI_5 films depicting their d) EQE, e) spectral responsivity, and f) linear dynamic range. Reproduced under the terms of the Creative Commons Attribution 4.0 International license.^[92] Copyright 2020, Pecunia et al.

all color matching functions for the HIA samples with a peak responsivity of 120 mA W^{-1} (Figure 17d). Additionally, the spectral rejection ratio (SRR_{EQE}) to the near-infrared for all samples was found to be >250 for wavelengths $>750 \text{ nm}$, which is much higher than that of Si photodetectors ($\text{SRR}_{\text{EQE}} \approx 1$), denoting the superior ability of Ag_2BiI_5 photodetectors to deliver NIR-blind light sensing. They further calculated their photodetector specific detectivity $D^*(\lambda)$, which quantifies the capability to differentiate low light intensity from noise. The calculated $D^*(\lambda)$ amounted to 2×10^{11} Jones for the HIA samples, based on the contributions from shot noise and Johnson–Nyquist noise. The linear dynamic range (LDR) is used to quantify the ability of a photodetector to maintain a linear photocurrent (I_{ph}) response over a broad optical power (P_{opt}) range. The HIA samples showed a linear response spanning over five orders of magnitude ($\approx 10 \text{ nW cm}^{-2}$ – 1 mW cm^{-2}) and a large LDR of $\approx 182 \text{ dB}$ (Figure 17e). The photocurrent transient response revealed an average rise and fall time for the HIA samples in the range of ≈ 45 to 175 ms . Overall, such Ag_2BiI_5 photodetectors were found to be promising candidates for NIR-blind visible photodetection.

The effect of morphology on photodetector performance was examined by Ramachandran et al. They fabricated Ag_2BiI_5 photodetectors with the architecture $\text{Ag}|\text{Ag}_2\text{BiI}_5|\text{Ag}$, which displayed a low responsivity of $\approx 506 \text{ nA W}^{-1}$ at a bias of 5 V .^[161] The primary reasons for such performance were the poor film morphology and the lateral device architecture used (cf. the vertical device architecture adopted by Pecunia et al.^[92]). In their case, the silver bismuth iodide films showed incomplete coverage with many pinholes. Moreover, Premkumar et al. investigated a UV photodetector based on quantum dots of various silver bismuth iodides (AgBiI_4 , Ag_2BiI_5 , and AgBi_2I_7).^[12] They reported the average photoluminescence lifetimes of AgBiI_4 , Ag_2BiI_5 , and AgBi_2I_7 to be *ca.* 4.6, 79, and 15.9 ns , respectively.

The longer lifetime for AgBi_2I_7 quantum dots was attributed to the absence of AgI impurities acting as trap sites. Among the three compositions, AgBi_2I_7 quantum dots showed the best performance under low-intensity UV light, achieving a maximum photocurrent of $\approx 1.2 \mu\text{A}$, an ON–OFF ratio of ≈ 280 and a responsivity of $\approx 0.15 \text{ A W}^{-1}$.

There has been only one report on the use of CuBiI_4 for photodetectors.^[102] The fabricated device architecture $\text{Au}|\text{CuBiI}_4|\text{Au}$ demonstrated a responsivity of $\approx 500 \text{ mA W}^{-1}$ and specific detectivity of $\approx 3.8 \times 10^7$ Jones. This work additionally revealed that a change in the Cu:Bi atomic ratio from 0:1 to 1:1 delivers an improvement in the photodetector performance, including an increase in the photocurrent by six orders of magnitude.

5.4. Radiation Detectors

Other than photodetectors, AgBi_2I_7 has recently been employed as a broadband X-ray detector.^[94] In fact, silver-bismuth iodides have significant potential as active materials for detecting ionizing radiation, given their ability to stop radiation based on their heavy elemental components and high density.^[162] Additionally, their high stability in various environmental conditions is favorable for the operation of such detectors in the ambient atmosphere. AgBi_2I_7 single crystal-based X-ray detectors displayed a higher absorption and attenuation coefficient ($\approx 97\%$) (Figure 18a,b) than halide-based perovskites, commercialized amorphous selenium (a-Se), and $\text{Cd}_{0.9}\text{Zn}_{0.1}\text{Te}$ (CZT). A high attenuation coefficient is beneficial, as it can reduce the functional layer's required thickness and the challenges in charge collection. The single crystals further demonstrated a limit of detection (LoD) of $72 \text{ nGy}_{\text{air}} \text{ s}^{-1}$ (Figure 18c), much lower than that of commercialized a-Se detectors and the dose rate currently required for X-ray diagnostics ($5.5 \mu\text{Gy}_{\text{air}} \text{ s}^{-1}$).

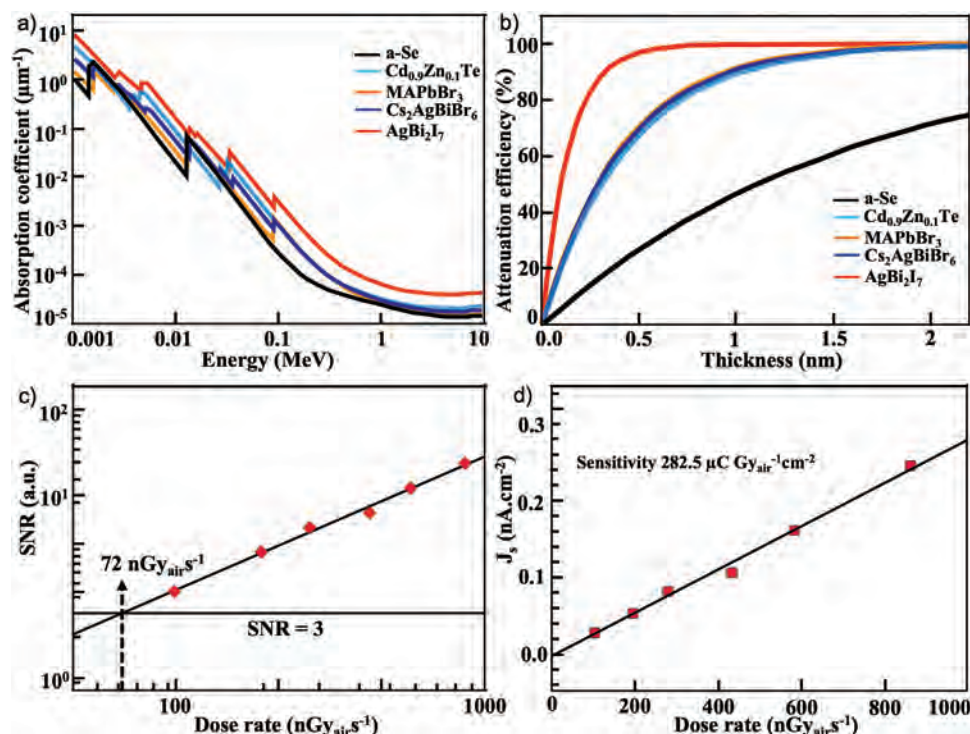


Figure 18. Performance of AgBi_2I_7 X-ray detectors. a) X-ray response characteristics of the AgBi_2I_7 X-ray detector under various dose rates. Inset: device structure of the X-ray detector; b) X-ray dose rate-dependent signal-to-noise ratio (SNR) of the device. The LOD of $72 \text{ nGy}_{\text{air}} \text{ s}^{-1}$ is derived from the slope of the fitting line with an SNR of 3; c) X-ray dose rate-dependent signal current density (J_s) of the device. The X-ray sensitivity of the device is derived from the slope of the fitting line. Reproduced with permission.^[94] Copyright 2020, American Chemical Society.

Furthermore, such silver-bismuth-iodide X-ray detectors had a sensitivity of $\approx 280 \mu\text{C Gy}_{\text{air}}^{-1}\text{cm}^{-2}$ to X-rays (Figure 18d), which is greater than that of MAPbBr_3 single crystals ($80 \mu\text{C Gy}_{\text{air}}^{-1}\text{cm}^{-2}$ at 22 keV) and $\text{Cs}_2\text{AgBiBr}_6$ single crystals ($105 \mu\text{C Gy}_{\text{air}}^{-1}\text{cm}^{-2}$ at 30 keV) and nearly 14 times greater than that of a-Se detectors ($20 \mu\text{C Gy}_{\text{air}}^{-1}\text{cm}^{-2}$ at 20 keV).

5.5. Memristors

Memristors are considered the fourth indispensable circuit element after resistors, capacitors, and inductors. The popularity and necessity of memristors have proliferated over the years with the ever-burgeoning development of IoT frameworks, artificial intelligence, and the need for high-volume confidential data storage. Fast and high photocurrent response, ON/OFF ratio, and low switching voltage properties of silver/copper pnicthoalides have prompted their investigation for memory devices. Specifically, due to its stability, very low operating voltages (e.g., device switching between SET and RESET only requires 0.16 V) and excellent ON/OFF ratio ($\approx 10^4$), AgBiI_4 has been utilized for nonvolatile memory devices such as resistive switching random-access memory (ReRAM) devices.^[91] In addition, the flexible ReRAM devices developed with this material exhibited excellent reproducibility, stability over 1000 bending tests, data withholding capacity over an extended period (maintaining high resistive and low resistive states for over 10^4 s), and reversible resistive switching under AC voltage pulses

(>700 cycles). Negligible degradation of the ON/OFF ratio was attributed to the increase in defects over time.^[91]

5.6. Chemical (or Ionic) Sensors

The detection of trace ions is crucial now more than ever with the increasing usage and wastage of electronic products, which contain elements hazardous to the environment and humans. According to the US and EU environmental protection regulations, even trace amounts of toxic ions could lead to physiological and neurological disorders in humans. As the cost and complexity of currently adapted chemical sensing analytical techniques have promoted highly selective, sensitive, and faster fluorescence-based sensors, silver/copper iodobismuthate-based compounds with good photoluminescence have recently attracted attention for detecting toxic ions. Premkumar et al. investigated silver iodobismuthate for this application for the first time by developing oleylamine-sulfide-passivated Ag_2BiI_5 quantum dots to detect copper(II) ions.^[12] The gradual incorporation of Cu^{2+} (up to $100 \times 10^{-9} \text{ M}$) in DMSO:water (3:2 vol) medium notably quenched (up to 90%) the overall photoluminescence emission of passivated Ag_2BiI_5 quantum dots without any significant peak shift or change in carrier lifetime (≈ 5.5 vs 4.8 ns). However, the quenching efficiency was limited to 21% in the unpassivated quantum dots, implying that passivation induced improved electron transfer for the reception of Cu^{2+} ions. Concurrent investigation with alkali, transition, and

posttransition metals (Na^+ , K^+ , Co^{2+} , Ni^{2+} , Zn^{2+} , Ag^+ , Pb^{2+} , Al^{3+} , Cr^{3+} , etc.) demonstrated no quenching even at five-fold higher concentrations, implying high selectivity toward Cu^{2+} ions, enabling the team to apply these silver pnictohalides to the detection of ions in tap water and drinking water samples.

6. Conclusions and Perspectives

Stability under various conditions, low toxicity, and high absorption coefficients render silver/copper pnictohalides attractive candidates for next-generation photovoltaics and optoelectronics. In this review article, we have discussed the various structures and compositions of these materials reported thus far. Substitution of the alkaline-earth A-site cations in lower-dimensional bismuth perovskites with coinage metal ions produces three-dimensionally connected networks with high crystalline symmetry but with a cubic or rhombohedral rather than perovskite structure. The silver-bismuth iodides generally have a rhombohedral structure for silver-rich compositions and a cubic structure for bismuth-rich compositions. It has been demonstrated that the rhombohedral phases have higher bandgaps than the cubic ones, while the electrical conductivity follows the opposite trend. Studies of the optoelectronic properties of silver iodobismuthates indicate that the bandgap and valence band edges of these unmodified materials are primarily defined by their crystal structure rather than composition. Thus, their optoelectronic properties can be tuned by structural modifications, in particular through the suppression of the crystallographic defects that might arise from cationic or anionic vacancies.

Various compositional engineering and morphological modification strategies have been successfully applied to tune the intrinsic light-harvesting capabilities of these materials. For example, incorporating a small amount of sulfur into silver bismuth iodides reduces the bandgap by elevating the valence band edge. Partial replacement of the A-site cations leads to an improvement in film morphology and reduced trap density. Furthermore, partial replacement of bismuth with antimony in silver bismuth iodide increases the bandgap, concurrently leading to a lower defect concentration. A similar observation of an increased bandgap was demonstrated when iodide was partially replaced by bromide in silver iodobismuthate. On the positive side, the film morphology improved, with more prominent grains and fewer defects upon bromide inclusion. Recently, there has been an increased interest in replacing silver with copper as the monovalent cation. Although the volume of research on copper pnictohalides is limited, the results are promising and deserve further in-depth studies.

The application of silver pnictohalides to photovoltaics has already delivered encouraging results. For example, despite the comparatively small scale and a short period of this research endeavor, silver bismuth iodides have impressively improved photovoltaic performance, with the first reported devices having a power conversion efficiency of $\approx 1.2\%$ and the latest devices achieving a PCE of $\approx 5.6\%$. Significant improvements in photovoltaic performance were primarily achieved through compositional modifications as well as the application of optimized synthesis and film fabrication strategies. These advances improved

the intrinsic light-harvesting capability, band structure and film morphology, thereby reducing traps and facilitating efficient charge transport and extraction. Furthermore, in light of the bandgaps of silver pnictohalides being close to 1.9 eV—optimal for indoor light harvesting—they are considered highly promising candidates for indoor photovoltaics. Indeed, silver pnictohalides have an ultimate maximum efficiency for indoor photovoltaics of $\approx 60\%$, which is appreciably higher than that of the commercially mainstream indoor photovoltaics based on hydrogenated amorphous silicon (a-Si:H) (which has a bandgap of ≈ 1.75 eV) and mainstream lead-halide perovskites developed for solar photovoltaics (which have bandgaps of ≈ 1.6 eV). Furthermore, while it has been demonstrated that mixing iodide with bromide in lead-based perovskites also leads to a bandgap of 1.9 eV, these materials are not photostable due to phase separation, which results in a reduction of the bandgap over time to ≈ 1.7 eV^[163] (i.e., a value that is far from the optimum for indoor light harvesting). Consequently, silver pnictohalides not only have considerable room for improvement in terms of their indoor photovoltaic performance but also their potential compares favorably to that of commercial and lead-halide perovskite indoor photovoltaics.

Furthermore, silver bismuth iodides have been investigated for visible light detection, delivering auspicious performance. These materials have also been applied to X-ray detection, already demonstrating better performance than halide-based perovskites, commercialized a-Se, and the currently promising $\text{Cd}_{0.9}\text{Zn}_{0.1}\text{Te}$ (CZT) with a large attenuation coefficient over a wide photon energy range but suffer from unbalanced charge carrier transportation.

Given their optoelectronic properties and the wide range of applications where silver/copper pnictohalides have shown promise, the research community has merely scratched the surface thus far in terms of realizing the photovoltaic and optoelectronic potential of these materials. Given the nascent stage of this research, there is considerable scope for further fundamental investigations and improvement of these materials and devices based thereon. In terms of the fundamental optoelectronic properties, deeper insights are needed into the charge transport, defect properties, and excitonic characteristics, which demand a concerted research effort both in terms of experimental characterization and computational modeling. High-throughput computational strategies and combinatorial synthesis are likely to be particularly useful in this regard and might further expand the library of promising compositions within this family of materials. As discussed above, device engineers are recommended to focus on efficient crystallographic and trap-state defect suppressing strategies to reduce voltage and current losses. Deposition methods that deliver conformal films with larger grain sizes and that passivate defect states at a material processing level might be worth pursuing in an attempt to resolve these constraints. Precise compositional control avoiding the formation of admixtures, which are ubiquitously found within Ag-rich or Bi-rich compositions, is expected to reduce vacancies and thereby improve the performance.

The photovoltaic performance losses reported for such materials to date might also be addressed through the application of effective defect passivation methods, for example, based on the use of cationic/anionic ligands, dopants, additives, or

conductive organic passivation layers. At the same time, thorough research is needed to establish the mechanisms of defect formation in the first place depending on the material compositions and synthesis procedures applied, which would naturally facilitate the development of strategies for surface and grain boundary defect passivation. In the same vein, the field currently lacks a robust understanding of the correlations between structure/composition, morphology, carrier dynamics, optoelectronic structure, and resulting performance for pnictohalide-based devices. At the device level, it is also important to select/develop transport layers that match the energy bands of silver/copper pnictohalides instead of adopting standard yet suboptimal transport layers.

Finally, although pnictohalides have been reported to exhibit excellent stability at elevated temperatures, in the presence of moisture and under illumination, the phenomenon of ion migration within these materials requires further study. The migration of Ag⁺ and Bi³⁺ ions might adversely affect the operational stability on longer timescales than currently assessed and/or under more challenging conditions, and therefore should be investigated and addressed to achieve performance metrics suitable for commercial deployment. Again, the development and application of passivation and doping strategies along with appropriate charge-transport materials can be expected to suppress the undesired ion migration pathways.

In conclusion, the promise already shown by silver/copper pnictohalides as lead-free perovskite-inspired semiconducting materials warrants a broader research effort for these environmentally friendly materials to deliver their full potential for next-generation photovoltaics and optoelectronics.

Acknowledgements

A.C. and N.P. contributed equally to this work. N.P. and A.N.S. acknowledge funding from the Australian Centre for Advanced Photovoltaics (ACAP) and the Australian Research Council through the Centre of Excellence in Exciton Science (CE170100026) and Future Fellowship (FT200100317). Responsibility for the views, information, or advice expressed herein is not accepted by the Australian Government. B.R.T. would like to acknowledge support from the National Science Foundation under grant DMR-2127473. V.P. acknowledges financial support from the National Natural Science Foundation of China (61805166).

Open access publishing facilitated by Monash University, as part of the Wiley - Monash University agreement via the Council of Australian University Librarians.

Conflict of Interest

The authors declare no conflict of interest.

Keywords

group IB, group VA, perovskite-inspired silver/copper pnictohalides, photodetectors, radiation detectors, rudorffites, solar cells

Received: March 23, 2022

Revised: May 29, 2022

Published online:

- [1] E. Płaczek-Popko, *Opto-Electronics Rev.* **2017**, *25*, 55.
- [2] *World Scientific Handbook of Organic Optoelectronic Devices* (Ed: F. So), Vol. 1–2, World Scientific, Singapore **2018**.
- [3] V. Pecunia, *Organic Narrowband Photodetectors: Materials, devices and applications*, IOP Publishing, Bristol, UK **2019**.
- [4] *Perovskite Solar Cells: Materials, Processes, and Devices* (Eds: M. Grätzel, S. Ahmad, S. Kazim), John Wiley & Sons, Ltd, Hoboken, NJ, USA **2021**.
- [5] A. K. Jena, A. Kulkarni, T. Miyasaka, *Chem. Rev.* **2019**, *119*, 3036.
- [6] N.-G. Park, K. Zhu, *Nat. Rev. Mater.* **2020**, *5*, 333.
- [7] J. Y. Kim, J.-W. Lee, H. S. Jung, H. Shin, N.-G. Park, *Chem. Rev.* **2020**, *120*, 7867.
- [8] J.-H. Yun, P. Chen, M. Lyu, L. Wang, M. Hao, *Adv. Energy Mater.* **2017**, *7*, 1602512.
- [9] Y. Yang, J. You, *Nature* **2017**, *544*, 155.
- [10] Z. B. H. A. B. Djurišić, F. Z. Liu, H. W. Tam, M. K. Wong, A. Ng, C. Surya, W. Chen, *Prog. Quantum Electron.* **2017**.
- [11] Q. Zhang, F. Hao, J. Li, Y. Zhou, Y. Wei, H. Lin, *Sci. Technol. Adv. Mater.* **2018**, *19*, 425.
- [12] S. Premkumar, D. Liu, Y. Zhang, D. Nataraj, S. Ramya, Z. Jin, B. B. Mamba, A. T. Kuvarega, J. Gui, *ACS Appl. Nano Mater.* **2020**, *3*, 9141.
- [13] F. Yang, D. Jang, L. Dong, S. Qiu, A. Distler, N. Li, C. J. Brabec, H. J. Egelhaaf, *Adv. Energy Mater.* **2021**, *11*, 2101973.
- [14] M. Batmunkh, Y. L. Zhong, H. Zhao, *Adv. Mater.* **2020**, *32*, 2000631.
- [15] C. Yang, R. Zhi, M. U. Rothmann, F. Huang, Y.-B. Cheng, W. Li, *Sol. RRL* **2022**, *6*, 2100600.
- [16] J. Chen, N.-G. Park, *ACS Energy Lett.* **2020**, *5*, 2742.
- [17] F. Yang, S. Wang, P. Dai, L. Chen, A. Wakamiya, K. Matsuda, *J. Mater. Chem. A* **2021**, *9*, 2612.
- [18] J.-P. Correa-Baena, M. Saliba, T. Buonassisi, M. Grätzel, A. Abate, W. Tress, A. Hagfeldt, *Science (80-.)* **2017**, *358*, 739.
- [19] N. Moody, S. Sesena, D. W. DeQuillettes, B. D. Dou, R. Swartwout, J. T. Buchman, A. Johnson, U. Eze, R. Brenes, M. Johnston, C. L. Haynes, V. Bulović, M. G. Bawendi, *Joule* **2020**, *4*, 970.
- [20] J. Li, H. L. Cao, W. Bin Jiao, Q. Wang, M. Wei, I. Cantone, J. Lü, A. Abate, *Nat. Commun.* **2020**, *11*, 310.
- [21] Y.-T. Huang, S. R. Kavanagh, D. O. Scanlon, A. Walsh, R. L. Z. Hoyer, *Nanotechnology* **2021**, *32*, 132004.
- [22] R. L. Z. Hoyer, P. Schulz, L. T. Schelhas, A. M. Holder, K. H. Stone, J. D. Perkins, D. Vigil-Fowler, S. Iol, D. O. Scanlon, A. Zakutayev, A. Walsh, I. C. Smith, B. C. Melot, R. C. Kurchin, Y. Wang, J. Shi, F. C. Marques, J. J. Berry, W. Tumas, S. Lany, V. Stevanović, M. F. Toney, T. Buonassisi, *Chem. Mater.* **2017**, *29*, 1964.
- [23] V. Pecunia, L. G. Occhipinti, A. Chakraborty, Y. Pan, Y. Peng, *APL Mater.* **2020**, *8*, 100901.
- [24] W. Ke, C. C. Stoumpos, M. G. Kanatzidis, *Adv. Mater.* **2019**, *31*.
- [25] J. Cao, F. Yan, *Energy Environ. Sci.* **2021**, *14*, 1286.
- [26] Z. Xiao, Z. Song, Y. Yan, *Adv. Mater.* **2019**, *31*, 1803792.
- [27] J. Li, J. Duan, X. Yang, Y. Duan, P. Yang, Q. Tang, *Nano Energy* **2021**, *80*, 105526.
- [28] F. Giustino, H. J. Snaith, *ACS Energy Lett.* **2016**, *1*, 1233.
- [29] T. N. Huq, L. C. Lee, L. Eyre, W. Li, R. A. Jagt, C. Kim, S. Fearn, V. Pecunia, F. Deschler, J. L. MacManus-Driscoll, R. L. Z. Hoyer, *Adv. Funct. Mater.* **2020**, *30*, 1909983.
- [30] Z. Jin, Z. Zhang, J. Xiu, H. Song, T. Gatti, Z. He, *J. Mater. Chem. A* **2020**, *8*, 16166.
- [31] Y. Lei, S. Wang, J. Xing, H. Xu, J. Han, W. Liu, *Inorg. Chem.* **2020**, *59*, 4349.
- [32] Y. Tang, M. Liang, B. Chang, H. Sun, K. Zheng, T. Pullerits, Q. Chi, *J. Mater. Chem. C* **2019**, *7*, 3369.
- [33] D. Zhou, T. Zhou, Y. Tian, X. Zhu, Y. Tu, *J. Nanomater.* **2017**, *2018*, 8148072.
- [34] J. P. Correa-Baena, L. Nienhaus, R. C. Kurchin, S. S. Shin, S. Wieghold, N. T. Putri Hartono, M. Layurova, N. D. Klein,

- J. R. Poindexter, A. Polizzotti, S. Sun, M. G. Bawendi, T. Buonassisi, *Chem. Mater.* **2018**, *30*, 3734.
- [35] L. Zhang, K. Wang, B. Zou, *ChemSusChem* **2019**, *12*, 1612.
- [36] V. Pecunia, L. G. Occhipinti, A. Chakraborty, Y. Pan, Y. Peng, *APL Mater.* **2020**, *8*, 100901.
- [37] C. Lan, G. Liang, S. Zhao, H. Lan, H. Peng, D. Zhang, H. Sun, J. Luo, P. Fan, *Sol. Energy* **2019**, *177*, 501.
- [38] M. D. Prasad, M. G. Krishna, S. K. Batabyal, *ACS Appl. Nano Mater* **2021**, *4*, 1252.
- [39] Z. Shao, T. Le Mercier, M. B. Madec, T. Pauporté, *Mater. Lett.* **2018**, *221*, 135.
- [40] X. Jia, L. Ding, *Sci. China Mater* **2019**, *62*, 54.
- [41] Y. Kim, Z. Yang, A. Jain, O. Voznyy, G.-H. Kim, M. Liu, L. N. Quan, F. P. García de Arquer, R. Comin, J. Z. Fan, E. H. Sargent, *Angew. Chemie* **2016**, *128*, 9738.
- [42] N. Pai, J. Lu, T. R. Gengenbach, A. Seeber, A. S. R. Chesman, L. Jiang, D. C. Senevirathna, P. C. Andrews, U. Bach, Y. B. Cheng, A. N. Simonov, *Adv. Energy Mater.* **2019**, *9*, 1803396.
- [43] I. Turkevych, S. Kazaoui, E. Ito, T. Urano, K. Yamada, H. Tomiyasu, H. Yamagishi, M. Kondo, S. Aramaki, *ChemSusChem* **2017**, *10*, 3754.
- [44] H. B. W. Rudorff, *Zeitschrift für Naturforsch* **1954**, *9b*, 614.
- [45] A. Okada, K. Keil, *Am. Mineral.* **1962**, *67*, 132.
- [46] I. Ganesh, *Int. Mater. Rev.* **2013**, *58*, 63.
- [47] Z. Xiao, W. Meng, D. B. Mitzzi, Y. Yan, *J. Phys. Chem. Lett.* **2016**, *7*, 3903.
- [48] T. Oldag, T. Aussieker, H.-L. Keller, C. Preitschaft, A. Pfitzner, *Zeitschrift für Anorg. und Allg. Chemie* **2005**, *631*, 677.
- [49] L. F. Mashadiev, Z. S. Aliev, A. V. Shevelkov, M. B. Babanly, *J. Alloys Compd.* **2013**, *551*, 512.
- [50] H. Zhu, M. Pan, M. B. Johansson, E. M. J. Johansson, *ChemSusChem* **2017**, *10*, 2592.
- [51] Z. Shao, T. Le Mercier, M. B. Madec, T. Pauporté, *Mater. Des.* **2018**, *141*, 81.
- [52] A. Koedtrud, M. Goto, M. Amano Patino, Z. Tan, H. Guo, T. Nakamura, T. Handa, W.-T. Chen, Y.-C. Chuang, H.-S. Sheu, T. Saito, D. Kan, Y. Kanemitsu, A. Wakamiya, Y. Shimakawa, *J. Mater. Chem. A* **2019**, *7*, 5583.
- [53] K. W. Jung, M. R. Sohn, H. M. Lee, I. S. Yang, S. Do Sung, J. Kim, E. Wei-Guang Diao, W. I. Lee, *Sustain. Energy Fuels* **2018**, *2*, 294.
- [54] H. C. Sansom, G. F. S. Whitehead, M. S. Dyer, M. Zanella, T. D. Manning, M. J. Pitcher, T. J. Whittles, V. R. Dhanak, J. Alaria, J. B. Claridge, M. J. Rosseinsky, *Chem. Mater.* **2017**, *29*, 1538.
- [55] P. H. Fourcroy, M. Palazzi, J. Rivet, J. Flahaut, R. Céolin, *Mater. Res. Bull.* **1979**, *14*, 325.
- [56] G. A. Dzeranova, K. B. Kaloev, N. I. Bukhalova, *Zhurnal Neorg Khimii* **1985**, *30*, 2983.
- [57] A. Kulkarni, A. K. Jena, M. Ikegami, T. Miyasaka, *Chem. Commun.* **2019**, *55*, 4031.
- [58] W. Hu, X. He, Z. Fang, W. Lian, Y. Shang, X. Li, W. Zhou, M. Zhang, T. Chen, Y. Lu, L. Zhang, L. Ding, S. Yang, *Nano Energy* **2020**, *68*, 104362.
- [59] J. Tu, C. Kou, M. Liu, H. Lu, Y. Liu, H. Tan, W. Li, Z. Bo, *SN Appl. Sci.* **2019**, *1*, 620.
- [60] *Chemistry of the Elements* (Eds: N. N. Greenwood, A. Earnshaw), Elsevier, Oxford, UK **1997**, pp. 547–599.
- [61] N. Burford, Y. Carpenter, E. Conrad, C. D. L. Saunders, in *Biological Chemistry of Arsenic, Antimony and Bismuth* (Ed: H. Sun), John Wiley & Sons Ltd, Chichester, UK **2011**, pp. 1–17.
- [62] M. B. Gray, E. T. McClure, N. P. Holzappel, F. P. Evaristo, W. Windl, P. M. Woodward, *J. Solid State Chem.* **2021**, *297*, 121997.
- [63] H. Zhu, A. Erbing, H. Wu, G. J. Man, S. Mukherjee, C. Kamal, M. B. Johansson, H. Rensmo, M. Odellius, E. M. J. Johansson, *ACS Appl. Energy Mater.* **2020**, *3*, 7372.
- [64] G. S. Plumlee, M. J. Logsdon, L. F. Filipek, in *The Environmental Geochemistry of Mineral Deposits*, Society of Economic Geologists, Littleton, CO, USA **1997**, pp. 29–70.
- [65] F. F. Jaldurgam, Z. Ahmad, F. Touati, *Nanomaterials* **2021**, *11*, 895.
- [66] Z. Hu, Z. Wang, G. Kapil, T. Ma, S. Iikubo, T. Minemoto, K. Yoshino, T. Toyoda, Q. Shen, S. Hayase, *ChemSusChem* **2018**, *11*, 2930.
- [67] P. H. Fourcroy, D. Carré, F. Thévet, J. Rivet, *Acta Crystallogr. Sect. C Cryst. Struct. Commun.* **1991**, *47*, 2023.
- [68] L. R. V. Buizza, H. C. Sansom, A. D. Wright, A. M. Ulatowski, M. B. Johnston, H. J. Snaith, L. M. Herz, *Adv. Funct. Mater.* **2022**, *32*, 2108392.
- [69] H. C. Sansom, L. R. V. Buizza, M. Zanella, J. T. Gibbon, M. J. Pitcher, M. S. Dyer, T. D. Manning, V. R. Dhanak, L. M. Herz, H. J. Snaith, J. B. Claridge, M. J. Rosseinsky, *Inorg. Chem.* **2021**, *60*, 18154.
- [70] L. Wang, Y. Bao, S. Wang, F. Wang, C. Xie, K. T. Butler, X. Fan, *Cryst. Growth Des.* **2021**, *21*, 2850.
- [71] A. Adappattu Ramachandran, B. Krishnan, D. Avellaneda Avellaneda, M. Isabel Mendivil Palma, J. Amilcar Aguilar Martinez, S. Shaji, *Appl. Surf. Sci.* **2021**, *564*, 150438.
- [72] A. K. Baranwal, H. Masutani, H. Sugita, H. Kanda, S. Kanaya, N. Shibayama, Y. Sanehira, M. Ikegami, Y. Numata, K. Yamada, T. Miyasaka, T. Umeyama, H. Imahori, S. Ito, *Nano Converg* **2017**, *4*, 26.
- [73] H. Lu, A. Krishna, S. M. Zakeeruddin, M. Grätzel, A. Hagfeldt, *iScience* **2020**, *23*, 101359.
- [74] R. Ali, Z.-G. Zhu, Q.-B. Yan, Q.-R. Zheng, G. Su, A. Laref, C. S. Saraj, C. Guo, *ACS Appl. Mater. Interfaces* **2020**, *12*, 49636.
- [75] N. J. Jeon, J. H. Noh, W. S. Yang, Y. C. Kim, S. Ryu, J. Seo, S. Il Seok, *Nature* **2015**, *517*, 476.
- [76] F. Yu, L. Wang, K. Ren, S. Yang, Z. Xu, Q. Han, T. Ma, *ACS Sustainable Chem. Eng.* **2020**, *8*, 9980.
- [77] R. D. Shannon, *Acta Crystallogr., Sect. A: Found. Crystallogr.* **1976**, *32*, 751.
- [78] S. Hosseini, M. Adelifard, *Phys. status solidi* **2021**, *218*, 2000774.
- [79] Q. Zhang, C. Wu, X. Qi, F. Lv, Z. Zhang, Y. Liu, S. Wang, B. Qu, Z. Chen, L. Xiao, *ACS Appl. Energy Mater.* **2019**, *2*, 3651.
- [80] Y. Wang, Y. Liu, X. Shi, L. Huang, J. Tong, G. Wang, D. Pan, *New J. Chem.* **2021**, *45*, 14158.
- [81] J. W. Park, Y. Lim, K. Y. Doh, M. T. Jung, Y. I. Jeon, I. S. Yang, H. S. Choi, J. Kim, D. Lee, W. I. Lee, *Sustain. Energy Fuels* **2021**, *5*, 1439.
- [82] H. C. Sansom, G. Longo, A. D. Wright, L. R. V. Buizza, S. Mahesh, B. Wenger, M. Zanella, M. Abdi-Jalebi, M. J. Pitcher, M. S. Dyer, T. D. Manning, R. H. Friend, L. M. Herz, H. J. Snaith, J. B. Claridge, M. J. Rosseinsky, *J. Am. Chem. Soc.* **2021**, *143*, 3983.
- [83] F. Iyoda, R. Nishikubo, A. Wakamiya, A. Saeki, *ACS Appl. Energy Mater.* **2020**, *3*, 8224.
- [84] H. Wu, H. Zhu, A. Erbing, M. B. Johansson, S. Mukherjee, G. J. Man, H. Rensmo, M. Odellius, E. M. J. Johansson, *ACS Appl. Energy Mater.* **2019**, *2*, 5356.
- [85] M. Bernechea, N. C. Miller, G. Xercavins, D. Therefore, A. Stavrinadis, G. Konstantatos, *Nat. Photonics* **2016**, *10*, 521.
- [86] N. Pai, J. Lu, D. C. Senevirathna, A. S. R. Chesman, T. Gengenbach, M. Chatti, U. Bach, P. C. Andrews, L. Spiccia, Y. B. Cheng, A. N. Simonov, *J. Mater. Chem. C* **2018**, *6*, 2483.
- [87] S. L. Diedenhofen, M. Bernechea, K. M. Felter, F. C. Grozema, L. D. A. Siebbeles, *Sol. RRL* **2019**, *3*, 1900075.
- [88] B. Ghosh, B. Wu, X. Guo, P. C. Harikesh, R. A. John, T. Baikie, Arramel, A. T. S. Wee, C. Guet, T. C. Sum, S. Mhaisalkar, N. Mathews, *Adv. Energy Mater.* **2018**, *8*, 1802051.
- [89] C. Lu, J. Zhang, H. Sun, D. Hou, X. Gan, M. H. Shang, Y. Li, Z. Hu, Y. Zhu, L. Han, *ACS Appl. Energy Mater.* **2018**, *1*, 4485.

- [90] M. Khazaei, K. Sardashti, C.-C. Chung, J.-P. Sun, H. Zhou, E. Bergmann, W. A. Dunlap-Shohl, Q. Han, I. G. Hill, J. L. Jones, D. C. Lupascu, D. B. Mitzi, *J. Mater. Chem. A* **2019**, *7*, 2095.
- [91] H. Ye, B. Sun, Z. Wang, Z. Liu, X. Zhang, X. Tan, T. Shi, Z. Tang, G. Liao, *J. Mater. Chem. C* **2020**, *8*, 14155.
- [92] V. Pecunia, Y. Yuan, J. Zhao, K. Xia, Y. Wang, S. Duhm, L. Portilla, F. Li, *Nano-Micro Lett.* **2020**, *12*, 27.
- [93] Y. Seo, S. R. Ha, S. Yoon, S. M. Jeong, H. Choi, D. W. Kang, *J. Power Sources* **2020**, *453*, 227903.
- [94] S. Tie, W. Zhao, W. Huang, D. Xin, M. Zhang, Z. Yang, J. Long, Q. Chen, X. Zheng, J. Zhu, W. H. Zhang, *J. Phys. Chem. Lett.* **2020**, *11*, 7939.
- [95] Z. Yi, T. Zhang, H. Ban, H. Shao, X. Gong, M. Wu, G. Liang, X. L. Zhang, Y. Shen, M. Wang, *Sol. Energy* **2020**, *206*, 436.
- [96] D. Danilović, D. K. Božanić, R. Dojčilović, N. Vukmirović, P. Sapkota, I. Vukašinović, V. Djoković, J. Božek, C. Nicolas, S. Ptasińska, A. R. Milosavljević, *J. Phys. Chem. C* **2020**, *124*, 23930.
- [97] S.-Y. Lee, S.-M. Yoo, H. J. Lee, *Chem. Lett.* **2021**, *50*, 953.
- [98] F. He, Q. Wang, W. Zhu, D. Chen, J. Zhang, C. Zhang, Y. Hao, *Solid State Electron.* **2021**, *176*, 107950.
- [99] M. S. Shadabroo, H. Abdizadeh, M. Shabani, M. R. Golobostanfard, *Inorg. Chem.* **2021**, *60*, 11110.
- [100] A. Bera, S. Paramanik, A. Maiti, A. J. Pal, *Phys. Rev. Mater.* **2021**, *5*, 095404.
- [101] B. Zhang, Y. Lei, R. Qi, H. Yu, X. Yang, T. Cai, Z. Zheng, *Sci. China Mater.* **2019**, *62*, 519.
- [102] N. Qu, Y. Lei, X. Yang, X. Hu, W. Zhao, C. Zhao, Z. Zheng, *J. Mater. Chem. C* **2020**, *8*, 8451.
- [103] H. Yu, B. Zhang, R. Qi, N. Qu, C. Zhao, Y. Lei, X. Yang, Z. Zheng, *Sustain. Energy Fuels* **2020**, *4*, 2800.
- [104] Z. Bahari, F. Thévet, J. Rivet, J. Dugué, in *JEEP 2009 – 35th Conference on Phase Equilibria*, EDP Sciences, Les Ulis, France **2009**, p. 00020.
- [105] A. Largeteau, S. Darracq, G. Goglio, G. Demazeau, *High Press Res.* **2008**, *28*, 503.
- [106] A. König, A. Schreiner, *Powder Technol.* **2001**, *121*, 88.
- [107] J. R. Couper, W. R. Penney, J. R. Fair, S. M. Walas, in *Chemical Process Equipment*, Butterworth-Heinemann, Waltham, MA, USA **2012**, pp. 561–589.
- [108] L. L. Hench, J. K. West, *Chem. Rev.* **1990**, *90*, 33.
- [109] C. J. Brinker, G. W. Scherer, *Sol-Gel Science: The Physics and Chemistry of Sol-Gel Processing*, Academic Press, San Diego, CA, USA **1990**.
- [110] P. Schmidt, M. Binnewies, R. Glaum, M. Schmidt, in *Advanced Topics on Crystal Growth* (Ed: S. Ferreira), InTech, Rijeka, Croatia **2013**, Ch. 9.
- [111] J. Li, Q. Wu, J. Wu, in *Handbook of Nanoparticles* (Ed: M. Aliofkhaezai), Springer International Publishing, Cham, Switzerland **2016**, Ch. 12.
- [112] B. G. Rao, D. Mukherjee, B. M. Reddy, in *Nanostructures for Novel Therapy: Synthesis, Characterization and Applications* (Eds: D. Fica, A. M. Grumezescu), Elsevier Inc., Amsterdam, Netherlands **2017**, Ch. 1.
- [113] W. G. Burgers, *Physica* **1949**, *15*, 92.
- [114] J. Ulrich, H. C. Bülow, in *Handbook of Industrial Crystallization* (Ed: A. S. Myerson), Butterworth-Heinemann, Woburn, MA, USA **2002**, Ch. 7.
- [115] S. Premkumar, Z. Jin, D. Liu, D. Nataraj, B. B. Mamba, A. T. Kuvarega, J. Gui, *ACS Appl. Nano Mater* **2021**, *4*, 9895.
- [116] S. S. Hosseini, M. Adelifard, *J. Electron. Mater.* **2020**, *49*, 5790.
- [117] M. Xiao, F. Huang, W. Huang, Y. Dkhissi, Y. Zhu, J. Etheridge, A. Gray-Weale, U. Bach, Y. B. Cheng, L. Spiccia, *Angew. Chem., Int. Ed.* **2014**, *53*, 9898.
- [118] F. Huang, Y. Dkhissi, W. Huang, M. Xiao, I. Benesperi, S. Rubanov, Y. Zhu, X. Lin, L. Jiang, Y. Zhou, A. Gray-Weale, J. Etheridge, C. R. McNeill, R. A. Caruso, U. Bach, L. Spiccia, Y. B. Cheng, *Nano Energy* **2014**, *10*, 10.
- [119] N. Sahu, B. Parija, S. Panigrahi, *Indian J. Phys.* **2009**, *83*, 493.
- [120] Y. Vaynzof, *Adv. Energy Mater.* **2020**, *10*, 2003073.
- [121] I. Turkevych, S. Kazaoui, N. Shirakawa, N. Fukuda, *Jpn. J. Appl. Phys.* **2021**, *60*, SCCE06.
- [122] Y. Lei, L. Gu, X. Yang, L. Zhang, Y. Gao, J. Li, Z. Zheng, *J. Alloys Compd.* **2018**, *766*, 933.
- [123] Y. He, Y. Lei, X. Yang, K. Lu, S. Liu, L. Gu, Z. Zheng, *Appl. Surf. Sci.* **2016**, *389*, 540.
- [124] Y. Lei, H. Jia, W. He, Y. Zhang, L. Mi, H. Hou, G. Zhu, Z. Zheng, *J. Am. Chem. Soc.* **2012**, *134*, 17392.
- [125] J. Mei, M. Liu, P. Vivo, V. Pecunia, *Adv. Funct. Mater.* **2021**, *31*, 2106295.
- [126] Y. Peng, F. Li, Y. Wang, Y. Li, R. L. Z. Hoye, L. Feng, K. Xia, V. Pecunia, *Appl. Mater. Today* **2020**, *19*, 100637.
- [127] F. Li, Y. Wang, K. Xia, R. L. Z. Hoye, V. Pecunia, *J. Mater. Chem. A* **2020**, *8*, 4396.
- [128] X. Mettan, R. Pisoni, P. Matus, A. Pisoni, J. Jačimović, B. Náfrádi, M. Spina, D. Pavuna, L. Forró, E. Horváth, *J. Phys. Chem. C* **2015**, *119*, 11506.
- [129] A. Pisoni, J. Jačimović, O. S. Barišić, M. Spina, R. Gaál, L. Forró, E. Horváth, *J. Phys. Chem. Lett.* **2014**, *5*, 2488.
- [130] V. Pecunia, J. Zhao, C. Kim, B. R. Tuttle, J. Mei, F. Li, Y. Peng, T. N. Huq, R. L. Z. Hoye, N. D. Kelly, S. E. Dutton, K. Xia, J. L. MacManus-Driscoll, H. Sirringhaus, *Adv. Energy Mater.* **2021**, *11*, 2003968.
- [131] K. Wang, S. Olthof, W. S. Subhani, X. Jiang, Y. Cao, L. Duan, H. Wang, M. Du, S. (Frank) Liu, *Nano Energy* **2020**, *68*, 104289.
- [132] Y. Yuan, V. Pecunia, in *Proceedings of FLEPS 2019 – IEEE International Conference on Flexible and Printable Sensors and Systems*, IEEE, Piscataway, NJ, USA **2019**.
- [133] A. Crovetto, A. Hajjifarassar, O. Hansen, B. Seger, I. Chorkendorff, P. C. K. Vesborg, *Chem. Mater.* **2020**, *32*, 3385.
- [134] H. Yoo, J. Park, M. P. Suryawanshi, J. Lee, J. H. Kim, K. Eom, H. Seo, H. R. Jung, D. M. Kim, S. W. Shin, J. H. Kim, *J. Mater. Chem. A* **2021**, *9*, 5442.
- [135] M. Rehan, A. Cho, A. M. Amare, K. Kim, J. H. Yun, J. S. Cho, J. H. Park, J. Gwak, D. Shin, *Sol. Energy Mater. Sol. Cells* **2021**, *228*, 111138.
- [136] C. Chen, J. Tang, *ACS Energy Lett.* **2020**, *5*, 2294.
- [137] M. Li, C. Zhao, Z. K. Wang, C. C. Zhang, H. K. H. Lee, A. Pockett, J. Barbé, W. C. Tsoi, Y. G. Yang, M. J. Carnie, X. Y. Gao, W. X. Yang, J. R. Durrant, L. S. Liao, S. M. Jain, *Adv. Energy Mater.* **2018**, *8*, 1801509.
- [138] J. Dagar, S. Castro-Hermosa, G. Lucarelli, F. Cacialli, T. M. Brown, *Nano Energy* **2018**, *49*, 290.
- [139] M. Xie, K. Hisano, M. Zhu, T. Toyoshi, M. Pan, S. Okada, O. Tsutsumi, S. Kawamura, C. Bowen, *Adv. Mater. Technol.* **2019**, *4*, 1800626.
- [140] V. Pecunia, M. Fattori, S. Abdinia, H. Sirringhaus, E. Cantatore, *Organic and Amorphous-Metal-Oxide Flexible Analog Electronics*, Cambridge University Press, Cambridge, UK **2018**.
- [141] V. Pecunia, L. G. Occhipinti, R. L. Z. Z. Hoye, *Adv. Energy Mater.* **2021**, *11*, 2100698.
- [142] M. Freunek Müller, in *Indoor Photovoltaics* (Ed: M. Freunek Müller), John Wiley & Sons Inc., Hoboken, NJ, USA **2020**, Ch. 3.
- [143] F.-C. Chen, *Adv. Opt. Mater.* **2019**, *7*, 1800662.
- [144] L. K. Jagadamma, S. Wang, *Front. Chem.* **2021**, *9*, 71.
- [145] Y. Peng, T. N. Huq, J. Mei, L. Portilla, R. A. Jagt, L. G. Occhipinti, J. L. MacManus-Driscoll, R. L. Z. Hoye, V. Pecunia, *Adv. Energy Mater.* **2021**, *11*, 2002761.
- [146] Z. Jiang, S. Soltanian, B. Gholamkhash, A. Aljaafari, P. Servati, *RSC Adv.* **2018**, *8*, 36542.

- [147] Y. Yan, F. Cai, L. Yang, J. Li, Y. Zhang, F. Qin, C. Xiong, Y. Zhou, D. G. Lidzey, T. Wang, *Adv. Mater.* **2017**, *29*, 1604044.
- [148] K. Xia, Y. Li, Y. Wang, L. Portilla, V. Pecunia, *Adv. Opt. Mater.* **2020**, *8*, 1902056.
- [149] S. Cai, X. Xu, W. Yang, J. Chen, X. Fang, *Adv. Mater.* **2019**, *31*, 1808138.
- [150] P. P. Manousiadis, K. Yoshida, G. A. Turnbull, I. D. W. Samuel, *Phil. Trans. R. Soc. A* **2020**, *378*, 20190186.
- [151] V. Pecunia, D. Natali, M. Caironi, in *Photodetectors: Materials, Devices and Applications*, 2nd ed. (Ed: B. Nabet), Elsevier, Cambridge, UK **2022**.
- [152] C. Li, W. Huang, L. Gao, H. Wang, L. Hu, T. Chen, H. Zhang, *Nanoscale* **2020**, *12*, 2201.
- [153] D. Yang, D. Ma, *Adv. Opt. Mater.* **2019**, *7*, 1800522.
- [154] J. Miao, F. Zhang, *J. Mater. Chem. C* **2019**, *7*, 1741.
- [155] V. Pecunia, *J. Phys. Mater.* **2019**, *2*, 042001.
- [156] C. Perumal Veeramalai, S. Feng, X. Zhang, S. V. N. Pammi, V. Pecunia, C. Li, *Photonics Res* **2021**, *9*, 968.
- [157] S. V. N. Pammi, R. Maddaka, V. D. Tran, J. H. Eom, V. Pecunia, S. Majumder, M. D. Kim, S. G. Yoon, *Nano Energy* **2020**, *74*, 104872.
- [158] S. V. N. Pammi, V. D. Tran, R. Maddaka, J. H. Eom, J. S. Jung, H. M. Jeong, M. D. Kim, V. Pecunia, S. G. Yoon, *Adv. Opt. Mater.* **2020**, *8*, 2000845.
- [159] V. H. Vuong, S. V. N. Pammi, K. S. Pasupuleti, W. Hu, V. D. Tran, J. S. Jung, M. D. Kim, V. Pecunia, S. G. Yoon, *Adv. Opt. Mater.* **2021**, *9*, 2100192.
- [160] Y. Zhang, Y. Ma, Y. Wang, X. Zhang, C. Zuo, L. Shen, L. Ding, *Adv. Mater.* **2021**, *33*, 2006691.
- [161] A. A. Ramachandran, B. Krishnan, D. A. A. Leal, E. G. Martinez, J. A. A. Martinez, D. A. Avellaneda, S. Shaji, *Mater. Today, Commun.* **2020**, *24*, 101092.
- [162] S. Del Sordo, L. Abbene, E. Caroli, A. M. Mancini, A. Zappettini, P. Ubertini, *Sensors* **2009**, *9*, 3491.
- [163] E. T. Hoke, D. J. Slotcavage, E. R. Dohner, A. R. Bowring, H. I. Karunadasa, M. D. McGehee, *Chem. Sci.* **2015**, *6*, 613.



Abhisek Chakraborty finished his M.Tech. (2008) in Nanotechnology from Amity University, India and then joined the Institute of Inorganic Chemistry, Academy of Science, Czech Republic (2011) as a researcher. Thereafter, he obtained his Ph.D. in electronics engineering from the University of Rome Tor Vergata (2017), following which he joined the Institute of Functional Nano & Soft Materials (FUNSOM), Soochow University, China, as a postdoctoral researcher, where he worked on lead-free perovskite solar cells until 2021. His research interests include solution-processed 1D/2D metal oxide and organic/inorganic perovskite thin films for piezotronic and photovoltaic device applications.



Narendra Pai is currently an Australian Centre for Advanced Photovoltaics Research Fellow who is enthusiastic about developing novel lead-free perovskite materials for outdoor and indoor photovoltaic applications. He has concluded his Ph.D. research on developing solution processible lead-free solar cells at Monash University 2019 under the supervision of Dr. Alexandr N. Simonov and Late Prof. Leone Spiccia. Adjunctive to his Ph.D. research, he was awarded a postgraduate publication scholarship by the Monash School of Chemistry.



Alexandr N. Simonov is an Australian Research Council Future Fellow at the School of Chemistry, Monash University. Research in his group is aimed at designing and understanding new methods to generate and use renewable solar electricity for sustainable chemistry technologies, in particular for water electrolysis and transformations of inorganic N-compounds, using in situ spectroelectrochemical methods and advanced electroanalytical techniques.



Vincenzo Pecunia is an associate professor at the School of Sustainable Energy Engineering, Simon Fraser University, Canada, and a Fellow of the Institute of Materials, Minerals and Mining. He earned his Ph.D. in Physics and worked as a postdoctoral researcher at the Cavendish Laboratory, University of Cambridge, UK (2009–2016). At Simon Fraser University, he leads the Sustainable Optoelectronics group, whose research focuses on printable, eco-friendly semiconductors—e.g., organics, lead-free perovskite-inspired materials, and carbon nanotubes—and their applications in photovoltaics and optoelectronics. His research breakthroughs include the pioneering of indoor photovoltaics based on lead-free perovskite-inspired materials and ultralow-power printed-thin-film-transistor electronics.